

196 Beams in a Scanning Electron Microscope

Proefschrift

ter verkrijging van de graad van doctor

aan de Technische Universiteit Delft,

op gezag van de Rector Magnificus prof. ir. K.C.A.M. Luyben, voorzitter van
het College voor Promoties,

in het openbaar te verdedigen op dinsdag 19

November 2013 om 12:30 uur

door

Ali MOHAMMADI-GHEIDARI

M.Sc in solid state Physics

Tarbiat Moallem University of Tehran (Kharazmi University), Tehran, Iran

geboren te Aliabad, Iran

Dit proefschrift is goedgekeurd door de promotor:
Prof. dr. ir. P. Kruit

Samenstelling promotiecommissie:

Rector Magnificus,	voorzitter
Prof. dr. ir. P. Kruit,	Technische Universiteit Delft, promotor
Prof. dr. ir. O.J. Luiten,	Technische Universiteit Eindhoven
Prof. P. Hommelhof,	Friedrich Alexander University
Prof. dr. P.H. Urbach,	Technische Universiteit Delft
Dr. C.W. Hagen,	Technische Universiteit Delft
Dr. A. Henstra,	FEI Company
Prof. Dr. H.W. Zandbergen,	Technische Universiteit Delft, reservelid



ISBN 978-94-6191-985-4

Copyright © 2011 by A. Mohammadi-Gheidari.

All rights reserved. No part of the material protected by this copyright notice may be reproduced or utilized in any form or by any means, electronic or mechanical, including photocopying, recording or by any information storage and retrieval system, without written permission from the copyright owner.

Printed in The Netherlands

Cover illustration: (front) an MBSEM image of a single hole. The diameter of the hole is much larger than the pitch of the beams, (back) an MBSEM image of nano-tin balls. To make these images standard SE detector of the single beam SEM is used.

Cover design: Marieke Dona

“Human beings are members of a whole,
In creation of one essence and soul.
If one member is afflicted with pain,
Other members uneasy will remain.
If you have no sympathy for human pain,
The name of human you cannot retain.”

- *Saadi*

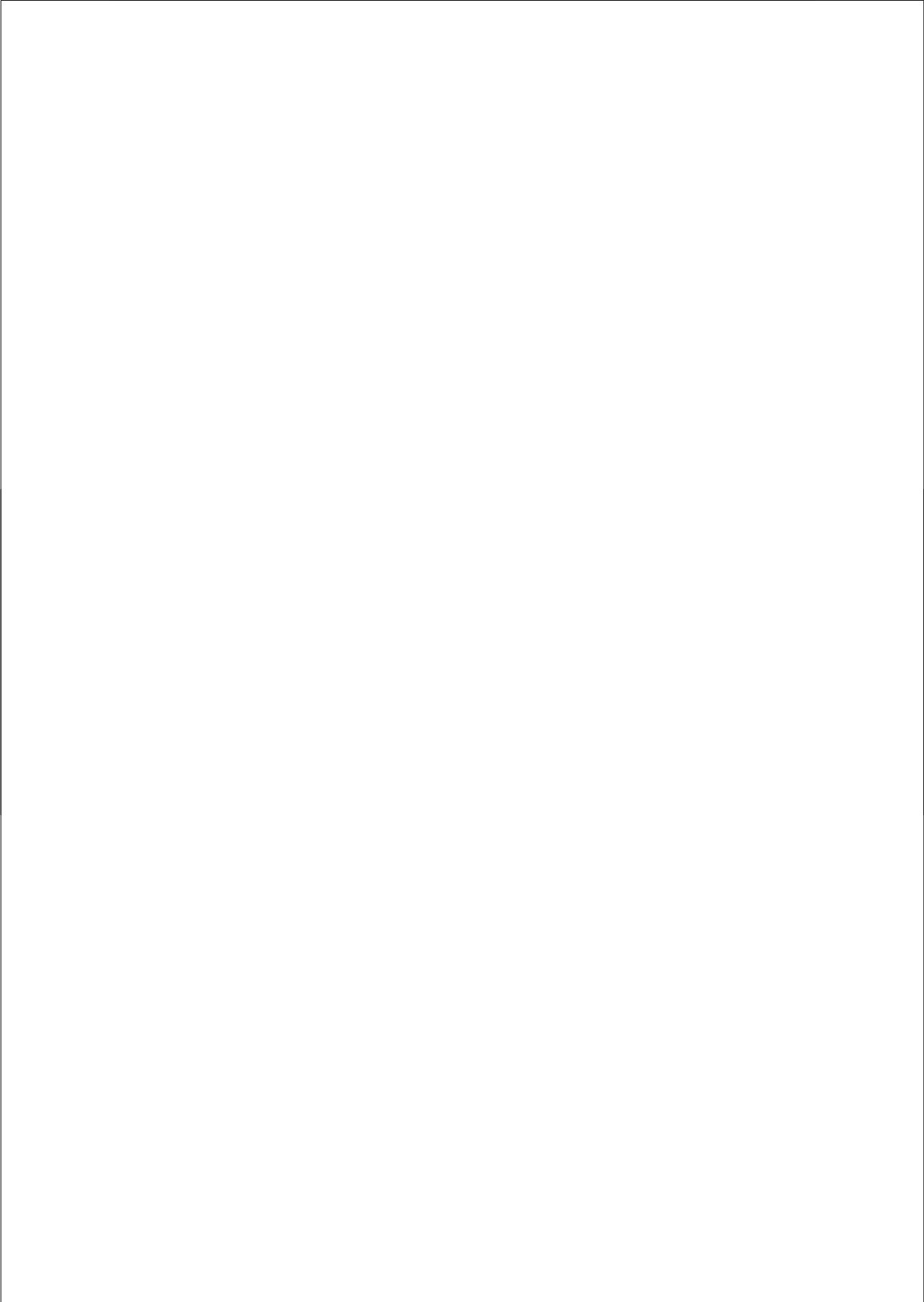
To my Mahboob, Sina and Hesam

Table of Contents

1 Introduction to scanning electron microscopy	1
1.1 From the origins to yesterday	1
1.2 SEMs today and future	3
1.3 The architecture of an SEM: Probe forming system	5
1.4 The electron optics of probe formation	7
1.5 Summary	10
2 Design of a Multi-electron beam source	13
2.1 General consideration for a multi-electron beam source	13
2.2 Multi-electron beam source equipped with a high brightness Schottky electron source	18
2.3 Multi-beam source tolerance	22
2.3.1 Problem description	24
2.3.2 Solution to the problem	25
2.3.3 Roundness of the electrodes	31
2.3.4 Tilt of aperture lenses plane	31
2.3.5 Results and discussions	33
2.4 Coulomb Interactions	34
2.5 Summary	37
3 Electron optics of multi-beam scanning electron microscope	39
3.1 Electron optics of multi-beam scanning electron microscope: Part I	39
3.1.1 Abstract	39
3.1.2 Introduction	40
3.1.3 General design considerations for a Multi-beam SEM	41
3.1.4 First-order optical system design	42
3.1.5 Accelerator lens design	44
3.1.6 Optics simulations of axial performance (method)	47
3.1.7 Optics simulations of axial performance (results)	48
3.1.8 Optics simulations of off-axial performance (method)	51
3.1.9 Optics simulations of off-axial performance (results)	54
3.1.10 Conclusions	57

3.2 Electron optics of multi-beam scanning electron microscope:	
Part II	57
3.2.1 Changing the MBSEM magnification	57
3.2.2 Different acceleration energies	65
3.2.2a High energy performance	65
3.2.2b Low energy performance.	66
3.2.3 C2 lens off mode	71
3.3 Electron optics of multi-beam scanning electron microscope:	
Part III	73
3.3.1 MBSM with larger pitch and higher probe current.	73
3.4 Coulomb interactions	81
3.5 Summary	81
4 Electro-mechanical design of the multi-beam source	85
4.1 Mechanical design	85
4.1.1 Vacuum design	87
4.1.2 Mechanical component design	88
4.1.3 Components assembly and alignment	90
4.1.3a MBS unit	91
4.1.3b Accelerator lens unit	94
4.1.3c complete multi beam source module	95
4.2 Electronics	99
4.3 Summary.	102
5 Experimental results of multi beam SEM	103
5.1 Multi-beam scanning electron microscope: Experimental	
results	105
5.1.1 Abstract	105
5.1.2 Introduction	105
5.1.3 MBSEM system design	106
5.1.4 MBSEM performance	110
5.1.5 Single beam performance of the MBSEM	115
5.2 Beam size measurement using a STEM detector	116
5.3 Summary.	118
6 Parallel EBID with MBSEM	121
Abstract	121
6.1 Introduction	122
6.2 Experimental	123

6.2.1 The Multi-beam SEM	123
6.2.2 Multi-beam EBID	124
6.3 Results and discussions	125
6.4 Summary and conclusions	128
7 Summary and Conclusions	129
8 Samenvatting en Conclusies	134
Acknowledgement	141



Introduction to scanning electron microscopy

“Hardly anyone ever produces a new idea. It is always some combination of old ideas that leads to reward. Revolutions are few and far between. It is steady progress that counts.”

L. Solymar & D. Walsh

The objective of this chapter is to give a brief introduction to the history of electron microscopy, its past and present developments and the main remaining challenge, its throughput will be discussed and possible solutions will be briefly considered and evaluated.

1.1 From the origins to yesterday

The history of electron optics or in general “charged particle optics” began in 1925, when Busch showed that an electro-magnetic field could be used to focus electrons and contemporarily de Broglie postulated the wave nature of the electrons. Later in 1931, Ernst Ruska and Max Knoll verified Busch’s lens formula experimentally and the idea of an electron microscope began to blossom. Finally in 1936 Knoll and Ruska built the first working Transmission Electron Microscope (TEM). It was designed much like an optical microscope, with electrons transmitted through the sample to form an image, instead of light. Very soon however, it was realized that TEMs could not be used to examine all kinds of samples, e.g. the topography of bulky samples cannot be imaged. This was the main driving force towards the introduction of a new class of electron

Chapter 1.

microscope, the scanning electron microscope (SEM). In a SEM a finely focused beam of electrons is scanned across the specimen and the generated signal per pixel is collected to form an image. Various signals generated as a consequence of electron-sample interactions reveal multiple contrast mechanisms providing a variety of information about the sample. Knoll was the first one who suggested the scanning electron beam device, in 1935. In 1938, von Ardenne suggested the use of Secondary Electrons (SEs) as signal to form an image. The first real SEM was built in 1942 by Zworykin with a resolution of 50nm. In 1956 Smith improved the instrument by improving the scanning system and, for the first time, incorporating a stigmator in it. In 1960 Everhart and Thornley developed a collector system using a scintillator-photomultiplier combination which improved the quality of SE collection significantly. Thanks to all of these remarkable achievements, in 1963 Pease and Nixon built a first prototype of a high-resolution SEM capable of reaching 6nm resolution, which was commercialized in 1965 by Cambridge Scientific Instrument, under the name of "Stereoscan" [1].

Since then, an enormous amount of efforts by various groups in different regions of the world was devoted to further evolution of the SEM, a remarkable portion of which was mainly focused on boosting the ultimate achievable resolution. To this end, the main attention was given to minimizing the lens aberrations, one of the major limits to the resolution. The second attention area was improving the acquisition-speed by using ever brighter electron sources. This is not only a matter of convenience for the operator, but also limits the effect of disturbances and drift. Currently commercially available SEMs equipped with a high brightness, low energy-spread Schottky electron source and an immersion objective lens can reach a resolution below 1nm. Even higher resolution has been obtained recently with the incorporation of monochromators and aberration correctors [2, 3]. Nowadays, the recognition that a SEM is an indispensable tool for various applications is not only because it can produce high resolution images, but also because it can be used for material modification at the nano-scale. Among other things, it is used for high resolution patterning through

Electron Beam Induced Deposition (EBID). EBID is a direct-write 2D and 3D-lithographic technique that uses a focused electron beam to make small material deposits. Precursor molecules (fig.1.1), adsorbed on a surface are dissociated by impinging electrons, resulting in a deposit of which the composition depends on the choice of precursor gas [4].

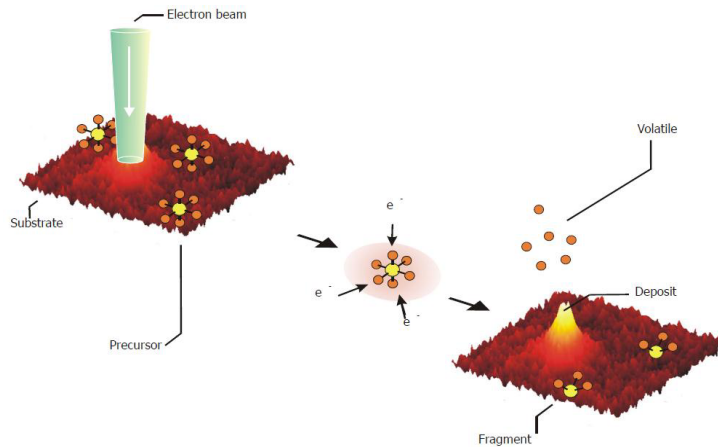


Figure 1.1 a schematic representation of electron beam induced deposition.

With this technique, structures of 1nm have been fabricated, using the Scanning Transmission Electron Microscope (STEM) [5]. The use of SEM, however, offers many advantages such as ease of use and broad availability. In fact, having EBID accessories in commercially available SEMs is nowadays a common option. Very recently, it has been demonstrated that 3 nm lines on bulk samples are feasible with SEM EBID [6].

1.2 SEMs today and future

State-of-the-art high resolution SEMs reach a resolution below 1nm with a typical beam current of 10-100 pico-Amps. Even though the task of resolution improvement is still being tackled, at the moment the resolution of SEMs is satisfactory enough for many high resolution applications. In these systems the required time for noise-free high resolution images of 10^6 pixels is typically in the order of a second (a current of 100 pA deposits 1000 electrons per pixel).

Chapter 1.

When used for patterning, the writing time for 10^6 pixels is only a few orders of magnitude larger. In the past when the application of the SEM was limited to laboratories or industries where occasionally a small sample had to be examined or a small feature had to be written this was not a major problem. Currently, there can be found thousands of SEMs around the world being used in multidisciplinary fields of nanotechnology, life sciences, energy resources and etc., and in different places from small lab's to industries.

In ever more applications, the acquisition speed is a problem. One example is the semiconductor industry, where samples as large as a 300mm Silicon-wafer can be accommodated in the chamber of current SEMs. It is completely impossible to write or image a surface of a full wafer. Stated differently, current SEMs are not yet capable of rapidly processing a large volume of samples both in imaging and patterning.

We can already make a very strong statement here and that is: what really is missing in the development of the SEM technology so far is the improvement in its throughput. The next two simple examples demonstrate this.

In order to understand the brain's functions, neuroscientists would like to have a complete picture of the neural circuitry of the brain. A typical neuronal circuit however, can be spread out in a bulky volume of tens of cubic millimetres of the brain tissue in a very complex shape. To produce the full picture of this circuit accurately, ultrathin (<50nm) serial sections of the brain tissue have to be imaged by a SEM and finally thousands of high resolution images have to be mapped out to produce a complete picture of the brain. Using current high resolution SEMs, a typical time necessary to image a very small volume of only 1mm^3 of the brain tissue sliced into thin sections of 50nm thickness, is approximately 600 years of continuous imaging. However, one can think of making use of all SEMs in the world (say 10000) to reduce the total imaging time to only 22 days! Notice that in this example (neither in the next one) the time needed to load the sample, piece by piece, in the system, the navigation time needed to find the region of interest on the sample and the time needed to save the images step by step is not included in the calculations! Let's see how things are with writing.

Imagine you want to make a $1 \times 1 \text{ mm}^2$ array of 1 nm^3 dots at a 10 nm pitch using a dose of 4 pC/nm^3 . With a typical probe current of 25 pA , it would take a bit more than 500 years. With all 10,000 SEMs it could be done in “only” 18 days!

The obvious solution to overcome the problem associated with the throughput of the SEM is to increase its probe current. But let us ask ourselves, why we can't increase the probe current of current high resolution SEMs? Indeed, why is there no SEM with 100 nA of probe current at 1 nm resolution? In order to answer these questions, we first need to understand how a SEM works. Therefore, for the moment we leave this till the next section, where the electron optics of the SEM is discussed, and here we offer some possible solutions to the problem.

One possible solution would be using many SEMs in parallel. With the conventional SEMs, it is very simple to realize that this is not a wise solution. However, recent works on the miniaturized SEMs can be a potential solution to the problem [7-17]. Another attractive alternative is to produce multiple focused beams in a single electron optical column [17-26].

We have developed a multi beam scanning electron microscope (MBSEM) that can produce 196 focused beams. This system is based on a standard SEM column equipped with a multi-beam source, the theoretical design and practical realization of which is the subject of this thesis.

1.3 The architecture of an SEM: Probe forming system

The architecture of the SEMs that we design today is, essentially, still the same as the first commercial system. Figure 1.2 shows a schematic representation of the fundamental architecture of the SEM. This configuration is sometimes referred to as a “probe forming unit”, and can be divided into two main units: the electron source and the electron optical column. The electron source provides a stream of electrons and accelerates them to a working energy. It consists of an electron emitter usually followed by an electrostatic (or electromagnetic) condenser lens, the “ C_1 lens”. An essential part of any electron source is the emitter from which the electrons are emitted. The electron optical column consists of one or two electrostatic and/or electromagnetic condenser lenses and an objective lens,

which is mostly a magnetic lens or a combination of electrostatic and magnetic lenses, to form a finely focused probe of electrons at the sample.

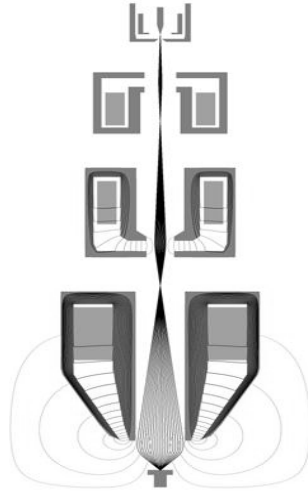


Figure 1.2 Schematic overview of the probe forming system.

The shape, size and enclosed current of this focused probe substantially determine the ultimate achievable resolution and throughput of the SEM. For microscopic applications of an electron source, its reduced brightness and energy spread are the most important parameters. The significance of a source with higher reduced brightness is simply more current in a given probe, and therefore a higher signal-to noise ratio in the image. Moreover, a lower energy spread means a lower contribution from chromatic aberration which is more favourable for low voltage applications. It is not, however, only the electron source that determines the performance of a microscope but also the electron optical column plays a very important role. In fact, for a desirable performance of the complete machine, there should be a perfect match between these two units.

These are pretty much the essential architectural components of any probe forming system. Depending on the application, extra accessories and arrangements are coupled to the probe forming unit. For instance for the application in microscopy, material analysis and inspection, the probe has to be scanned across the sample in a raster fashion and the generated signals due to the

electron specimen interaction need to be collected by detectors synchronous with the scanning system. These signals are then converted to an image.

In patterning applications, the probe is used to irradiate the defined position on the surface of the sample for a certain time called the “exposure time”. The exposure time is controlled by a set of blanking deflectors in association with a beam stop aperture and the pattern to be written is controlled by a computer which controls both the scanning and the blanking deflection systems. To better understand the importance of each unit of the probe forming system, and their individual influence on the overall performance of the system let’s briefly describe how a very simplified probe forming system, such as a SEM, works.

1.4 The electron optics of probe formation

In a SEM, or in general any probe forming system, the virtual source is strongly de-magnified to form a very small probe. In the absence of electron-electron interactions and energy filters, the reduced brightness is a conserved quantity throughout the electron optical column, hence the probe current, I , can be defined as [27]:

$$I = B_r U \pi^2 \alpha^2 \frac{d_{geo}^2}{4} \quad (1.1)$$

Where B_r is the reduced brightness of the electron source, U is the beam acceleration energy, α is the half opening angle at the probe and $d_{geo} = M \cdot d_v$ is the geometrical source image at the specimen where M is the total magnification of the electron lenses and d_v is the virtual source size.

In reality however, the area over which this current is distributed, is larger than the geometrical source image alone due to the lens aberrations and diffraction. That is, the real probe size is not just a perfect image of the electron source but a blurred image of it. To calculate the total probe size, d_p the contributions from lens aberrations and diffraction should be added to the geometrical source image. Among the many approximations used to add up the different contributions, the root power sum or “RPS” algorithm proposed by Barth and Kruit [28] is probably the most acceptable and accurate one.

We will use it throughout this thesis. It is based on using the FW50 size of the probe, i.e. the width that contains 50% of the total current and is expressed as:

$$d_p = \{[d_I^{1.3} + (d_\lambda^4 + d_s^4)^{1.3/4}]^{2/1.3} + d_c^2\}^{1/2} \quad (1.2)$$

Where d_I , d_λ , d_s and d_c are the FW50 diameters of the individual contributions from the source image, the diffraction, the spherical aberration, and the chromatic aberration, respectively. These FW50 values can be calculated using the following formulae:

$$d_I = d_{geo.} = M d_v = \frac{2}{\pi} \sqrt{\frac{I}{B_r V}} \frac{1}{\alpha} \quad (1.3)$$

$$d_\lambda = 0.54 \frac{\lambda}{\alpha} \quad (1.4)$$

$$d_s = 0.18 C_s \alpha^3 \quad (1.5)$$

$$d_c = 0.6 C_c \frac{\Delta U_{50}}{U} \alpha \quad (1.6)$$

Here λ is the wavelength of the electrons, U is the final acceleration energy of electrons, C_s and C_c are the spherical and chromatic aberration coefficients respectively, and ΔU_{50} is the FW50 value of the energy spread of the electron source (Note: for a ΔU_{FWHM} , the pre-factor of 0.6 in eq. (1.6) should be replaced with 0.34). It should be noted that C_s and C_c contain contributions from all the lenses, correctly scaled with their magnification. Almost in all high resolution probe forming systems, the objective lens has the strongest de-magnification of all lenses in the column making the aberration contributions of the other lenses negligible. Inserting equations (1.3), (1.4), (1.5) and (1.6) in equation (1.2), the only variable now left in the equation for total probe size is the half-angle at the probe. The opposite dependence of d_I & d_λ versus d_c & d_s on the half angle of the probe suggests that, for any given probe current, there will be an opening angle for which the probe size is minimum. Given a source with its parameters and electron lenses with their aberration coefficients, the electron optical columns are often optimized for the smallest probe size or the largest current in a given probe by finding the right opening angle of the probe and the total magnification of the system. Optimizing this angle in effect means balancing the contributions to the

probe that increase with α (objective lens aberrations) and the contributions that decrease with α (diffraction, source image, and C_1 lens aberrations).

Figure 1.3 shows one example of such an optimization for three different probe currents of 20, 50 and 100pA at beam acceleration energy of 10keV. To produce such graphs the aberration coefficients of the objective lens, C_s and C_c , are assumed to be 5mm and 3mm respectively which are reasonable numbers for an immersion objective lens with a working distance of about 5mm.

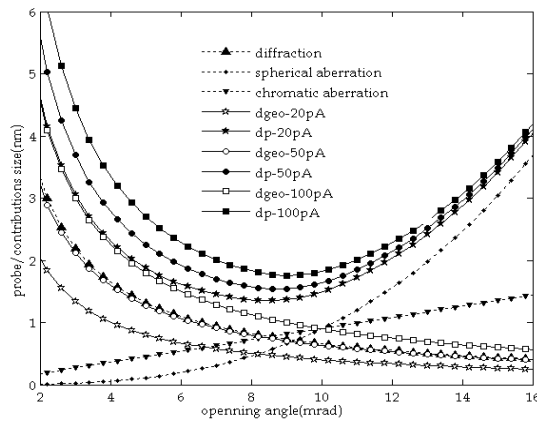


Figure 1.3 Variation of the probe size as a function of beam opening angle for 3 different probe currents of 20, 50 and 100pAs. The electron source is assumed to be a Schottky source with a typical reduced brightness of $5 \times 10^7 \text{ Am}^{-2}\text{sr}^{-1}\text{V}^{-1}$ [27].

From figure 1.3 the following conclusions can be drawn: for a specific probe current, an optimum opening angle can be found for which the probe size is minimum. For larger opening angles than the optimum, the probe size is mainly determined by lens aberrations. The lens aberrations enlarge the probe size for higher probe current. For smaller opening angles than the optimum, the contributions from lens aberrations are negligible but the probe size is mainly determined by contributions from the source image (reduced brightness of the electron source) and diffraction. For high probe current the contribution from source brightness is larger than that of diffraction whereas for lower probe current it is the other way around. A situation can be found in which the

contribution from diffraction and source image are almost equal. This is known as the diffraction limited regime. The diffraction limited probe and its current is the best one can get for a source with certain brightness irrespective of the quality of the optical column. From equations (1.1) and (1.4) it follows directly that the current in a diffraction limited probe is, $I = K \cdot B_r$ ($K = 10^{-18} m^2 SrV$). For a Schottky electron source with a typical reduced brightness of 5×10^7 ($Am^{-2}sr^{-1}V^{-1}$), this is 50 pA. This can also be clearly seen in the figure.

When we also minimize the probe size by choosing the optimum opening angle, we typically get a probe size of about 1.5nm at 10keV beam acceleration energy: the maximum current one can have close to the highest resolution of the SEM using a high brightness Schottky source is only 50pA!. Therefore, in order to have higher probe current while preserving the same probe size, even brighter electron sources have to be realized. The current in a probe can be increased by enlarging the opening angle at the cost of an increase in the probe size due to the increased lens aberrations. One may think of using expensive aberration correctors to suppress or lower the aberration contribution, especially the contribution from spherical aberration which is the main limiting factor for higher current at high acceleration voltages. But even if we correct the spherical aberration, the current can only be increased to a limited amount and beyond that the Coulomb interactions will deteriorate the probe size at higher currents.

1.5 Summary

In this chapter it is discussed that the resolution of the current SEMs is good enough for any kind of high resolution application but the throughput is the main problem. The current of the conventional SEMs cannot be increased while maintaining high resolution, because of the limited brightness of the electron sources, lens aberrations and Coulomb interactions. The throughput can be increased by using multiple miniaturized SEMs or alternatively by incorporating a multi-beam source in an SEM. In the next Chapter we will explain the challenges in the design of a multi-beam source and present more detail on our multi-beam source concept.

1.6 Bibliography

- [1] C.W. Oatley, *J. Appl. Phys.* 53 (2002) (2).
- [2] R. Young, et al., *Proc. of SPIE Vol. 7378* (2009) 737803-15.
- [3] J. Zach, et al., *Nucl. Instr. and Meth. in phys. Res. A* 363 (1995) 316.
- [4] N. Silvis-Cividjian and C. W. Hagen, *Advances in Imaging and Electron Physics* (Elsevier, Amsterdam, 2006), Vol. 43.
- [5] W.F. van Dorp and C. W. Hagen, *J. Appl. Phys.* 104 (2008) 081301.
- [6] J.C. van Oven, et al., *J. Vac. Sci. Technol. B* 129 (2011) F305.
- [7] T.H.P. Chang, et al., *J. Vac. Sci. Technol. B* 14 (1996) 3774.
- [8] T.H.P. Chang, et al., *Microelectron. Eng.* 32 (1996) 113.
- [9] C.D. Bubeck, et al., *Nucl. Instr. and Meth. in phys. Res. A* 427 (1999) 108.
- [10] E. Kratschmer, et al., *J. Vac. Sci. Technol. B* 13 (1995) 2498.
- [11] H.S. Gross, et al., *Microelectron. Eng.* 35 (1997) 469.
- [12] D.A. Crewe, et al., *J. Vac. Sci. Technol. B* 14 (1996) 3808.
- [13] R.Y. Lutsch and E. Plies, *Ultramicroscopy* 93 (2002) 339.
- [14] I. Honjo, et al., *J. Vac. Sci. Technol. B* 15 (1997) 2742.
- [15] M. Mankos, et al., *J. Vac. Sci. Technol. B* 18 (2000) 3057.
- [16] Y. Endo, I. Honjo, and S. Goto, *J. Vac. Sci. Technol. B* 16 (1998) 3082.
- [17] D. Winkler, et al., *J. Vac. Sci. Technol. B* 16 (1998) 3181.
- [18] E. Yin, et al., *J. Vac. Sci. Technol. B* 18 (2000) 3126.
- [19] S. Tanimoto, et al., *Jpn. J. Appl. Phys., Part 1* 42 (2003) 6672.
- [20] S.T. Coyle et al., *J. Vac. Sci. Technol. B* 22 (2004) 501.
- [21] H. Yasuda, et al., *J. Vac. Sci. Technol. B* 14 (1996) 3813.
- [22] G. Winogard, et al., *J. Vac. Sci. Technol. B* 18 (2000) 3052.
- [23] M. Muraki and S. Gotoh, *J. Vac. Sci. Technol. B* 18 (2000) 3061.
- [24] N. Nakasuji, et al., *Jpn. J. Appl. Phys.* 44 (part 1) (2005) 5570.
- [25] O. Kamimura, et al., *J. Vac. Sci. Technol. B* 25 (1) (2007) 140.
- [26] A.J. van den Brom, et al., *J. Vac. Sci. Technol. B* 25 (6) (2007) 2245.
- [27] M. Bronsgeest, PhD Thesis, Delft University of Technology, 2009.
- [28] J. Barth, P. Kruit, *Optik* 101 (3) (1996) 101.

Chapter 1.

2 CHAPTER

Design of a multi-electron beam source

"We cannot solve the problems by using the same kind of thinking we used when we created them."

Albert Einstein

The objective is to develop a multi beam source module to be mounted in a Scanning Electron Microscope for high throughput and high resolution patterning and microscopy applications. From the preceding chapter, it is clear that we need a bright electron source to be able to achieve high resolution. In this chapter, various options for the multi beam source that were found in the literature are briefly reviewed. The problems associated with our older concept of multi beam SEM are discussed and a new concept is proposed. Finally, the electron optics, mechanical tolerances and the effect of electron-electron interactions of the new multi beam source is presented.

2.1 General consideration for a multi electron beam source

A multi electron beam source provides multiple beams for the system. So far multiple beams are either created by using multiple sources [1-3] or by using a single source that is split into multiple sub-beams using a micro-fabricated lens array [4-9]. Present multiple sources which are either photo-cathodes or cold field emitter arrays, are not yet suitable to be used in a high resolution multi beam SEM. Photo-cathodes have problems with poor current stability, short lifetime, and low brightness [10-14]. Cold field emitters, on the other hand, are promising candidates due to their high brightness, small virtual source size and low energy spread. They can be produced easily and cost

effectively in a micro-fabricated array. However, years of research and investment have not yet produced emitters that are sufficiently stable and reproducible to be useful in multi-beam systems [15-18].

Multiple beams from a single source are created by splitting and focusing the wide angle beam of a single source into many sub-beams with a micro-fabricated lens array. Two kinds of electron sources have been used so far: thermionic sources such as LaB₆ and dispenser type cathodes [19]. Both emitters provide a very high current but for high resolution applications the brightness is too low. We want to use the Schottky source which is the most widely used electron source in high resolution SEMs. Traditionally, a collimator lens is placed between the electron source and the micro-lens array so that the broad beam enters the micro-lenses parallel to the axis of the lenses [e.g. 6, 20]. For sources with a small virtual source size, this cannot be done because it introduces a chromatic deflection aberration larger than the source size itself for the off-axis beams [21]. An effort to correct for these aberrations has not yet succeeded [20]. To avoid the off-axial aberrations, Kruit has suggested placing the micro-lens array between the source and the collimator lens [21]. However, this introduces large aberrations in the traditional three-electrode micro-Einzel lenses due to the skewed incidence of the beams to the lens plane. Van Bruggen has suggested curing this by also skewing the three-electrode Einzel lenses [22], but this gives only a limited skew angle and leads to a complicated fabrication process for the lenses. Zhang, using a single electrode lens array which produces such thin lenses that a skew angle is much less of a problem, has designed a multi electron beam source operating at a low extraction voltage of 1kV [23]. Single electrode lenses need an electric field on the apertures supplied by "macro electrodes". These macro electrodes can either be between the source and the micro-lens array (decelerating at the micro-lenses) or after the micro-lens array (accelerating at the micro-lenses) [23]. We will make use of Zhang's first concept (decelerating at micro-lenses). However, to adopt this concept with a standard SEM infrastructure, an extraction voltage of about 5kV has to be used. This calls for a re-optimization

of the multi electron beam source. Van Bruggen proposed the first version of such a design and built it [24]. However, the complexities associated with his design, convinced us to start with a new design for a multi electron beam source module. Figure 2.1 shows a picture of a standard single beam Nova nano SEM (left), multi electron beam SEM equipped with a multi electron beam source module designed and built by Van Bruggen (middle) and the MBSEM, which is the present working multi beam SEM (right). As shown in the middle picture, a massive and huge extension unit was added to the standard SEM column that served as a multi electron beam source module. In this extension part, all electron optical components and also high voltage electrical feed-throughs were accommodated. These electrical feed-throughs were necessary both for supplying voltages to the extra lens electrodes of the multi electron beam source and also for supplying voltages to the beam blanking electrodes meant for individual control of the beams.

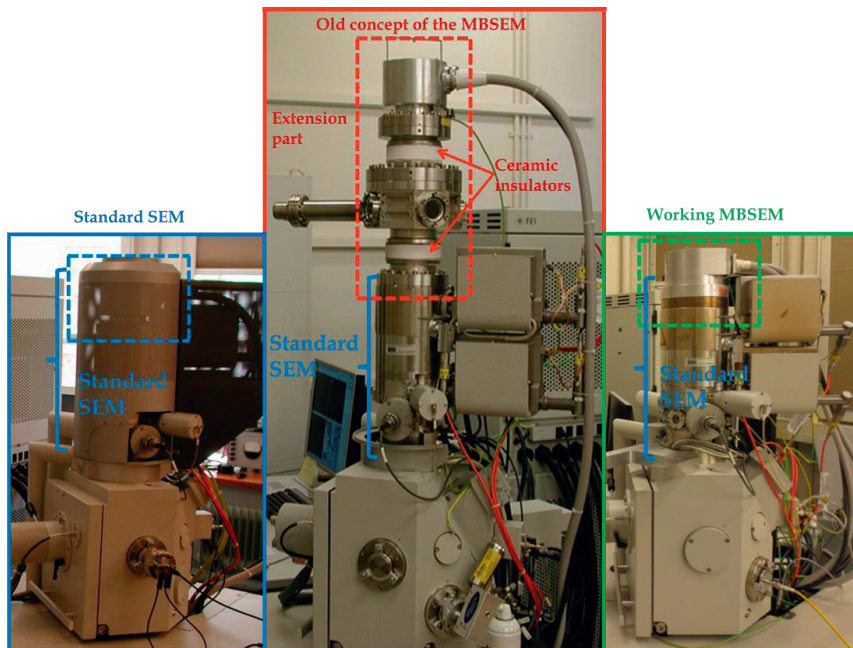


Figure 2.1 Photo of a standard single beam Nova-nano 200 SEM (left), a multi beam SEM as designed by Van Bruggen et al. (middle) and the present working MBSEM (right).

Chapter 2.

The system shown in the middle of figure 2.1 was the latest status of the multi beam SEM project when I took over the project with the aim of getting it to work and to characterize its performance. After a few months of struggle however, we found that it was impossible to get the Schottky source in stable and reliable operation; there were continuously vacuum problems, high tension breakdowns and system shut downs. There were several problems associated with that particular design. Here we only mention two of them to show that it was indeed a wise choice to start with a new design instead of struggle further with the old design. The first problem was the fact that the complete extension part had to be evacuated using only a standard ion getter pump (IGP) with a limited pumping speed of only 25 l/s as designed for a standard column. After vacuum calculations and experimental measurements, it was found that the out-gassing rate of the extension part together with the multi beam source components was about four orders of magnitude ($\approx 8 \times 10^{-7}$ mbar.l.sec⁻¹.cm⁻²) larger than that of a standard source.

The huge out-gassing area can be simply seen from figure 2.2 where the schematic drawing of the standard source with its components and its housing in a Nova-nano SEM (fig. 2.2a) is compared with the two different versions of the multi beam source modules and their components (fig. 2.2 b,c).

As can be seen from the fig.2.2b, the huge out-gassing area of the multi beam source designed by Van Bruggen on one hand and the lack of enough pumping capacity on the other hand, made it impossible to obtain an adequate vacuum condition required for stable and reliable operation of the Schottky source. Even a careful cleaning of the components and a longer bake out didn't help to reach a minimum required vacuum level. The only solution was to have extra pumping capacity at the extension part. There was however, a second problem to this design, a more serious problem: the complete extension unit had to be floated at a high voltage of -28.5kV with respect to real ground, making the system a very dangerous and unfriendly toy, a real monster, to play with.

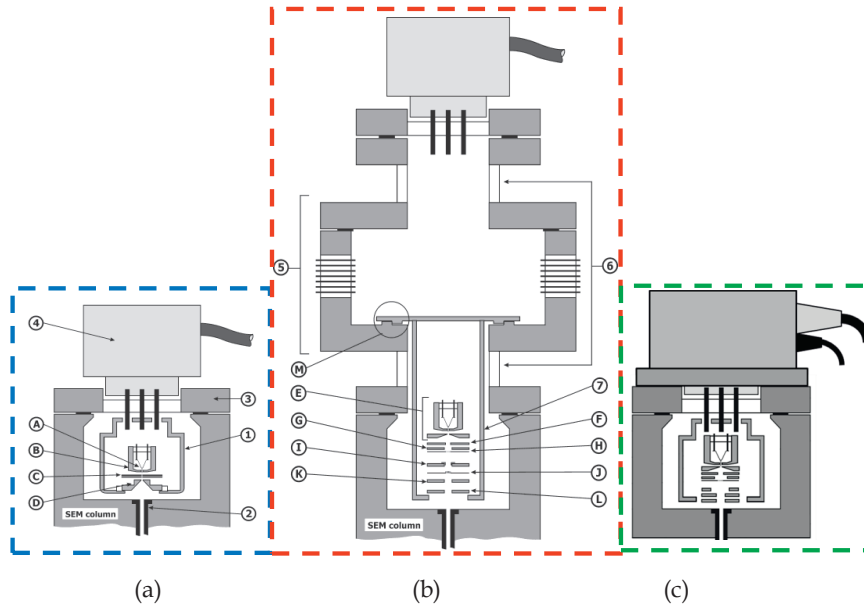


Figure 2.2 Schematic cross section of: a) the standard Nova nano 200 SEM source section with the electron source module (1), containing a Schottky emitter (A), suppressor (B), extractor (C) and C₁ electrode (D), the coulomb tube (2), the CF100 flange with standard high voltage feed-throughs (3) and the electrical connector for the source module (4); b) the modified source by Van Bruggen with the extension part including the feed-throughs (5), the ceramic insulators to insulate the extension unit floating at -28.5KV with respect to ground from the rest of the column (6), the MBS mounting stage (7) containing a Schottky electron source with pre-integrated Schottky emitter, suppressor and extractor (E), MBS electrode 1 (E₁) (F), MBS electrode 2 (E₂) (G), aperture lens array (H), octupole for alignment (I), blanker array (J), accelerator electrode 1 (Acc-1) (K) and accelerator electrode 2 (Acc-2) (L). The fitting edge (M) is used to mechanically align the mounting stage with respect to the chamber (From [24] with permission); c) the new compact design of the multi beam source module as is used at the present MBSEM. This multi beam source module fits in the standard column of the Nova nano SEM with no need for further modifications.

We therefore decided to get rid of the extension part and design a new multi beam source module, a more compact and user friendly one, free from all those problems (figure 2.2 c). Removing the extension part was not for free and had of course consequences on both electron optical and electro-mechanical design of the previous multi beam source module. We tried to keep as much as possible of the electron optical beam splitting concept as proposed by Zhang and Van Bruggen in our new multi beam source. In the forthcoming sections, we will briefly present the electron optical design of the

new multi beam source unit. In particular the accelerator lens had to be redesigned and consequently the electron optics of the complete column had to be re-optimized and calculated.

The electron optics of a new accelerator lens and the aberration optimization of the complete SEM column is the subject of chapter 3.

2.2 Multi-electron beam source equipped with a high brightness Schottky electron source

Our multi beam source module is composed of two crucial components; the multi beam source unit (sometimes referred to as: MBS) whose electron optical design will be briefly discussed here, and the accelerating lens unit (sometimes referred to as: ACC) whose electron optical design will be discussed in chapter 3. As mentioned in the previous section, the essence of our multi beam source is based on a multi beam source design proposed by Zhang and Kruit [23]. We, however, re-optimized its electron optics and its electro-mechanics in order to adopt it to our compact mechanical design of the source module but also to make it compatible with the standard SEM infrastructure. We therefore intend to only present a brief summary of its electron optical design and characteristics here, but a more elaborate and detailed electron optical design, in terms of aberration minimization can be found elsewhere [23]. Figure 2.3a shows our multi beam source module configuration including MBS and ACC with equi-potential lines and real rays modelled using EOD [25]. This source module is used in our multi beam SEM (sometimes referred to as: MBSEM) to produce an array of focused beams. Figure 2.3b shows the first part of the multi beam source module, the multi-beam source configuration, its equi-potential lines as modelled by the EOD program. The inset picture of figure 2.3b represents the way that a micro-lens effect is created. In the MBS the emission cone of a high brightness Schottky source is split into an array of focused beams by an aperture lens array (sometimes referred to as: ALA). The aperture lens array consists of a thin Si membrane with micro-apertures fabricated using micro-fabrication

technology. Two macro electrodes in combination with the extractor electrode of the electron source and the aperture plate create a so called “zero-strength macro lens”. “Zero strength” means that the off-axis beams are not deflected, thus avoiding the problem associated with chromatic deflection errors. The field from the macro electrodes ends on the aperture plate, forming low aberration single aperture lenses for the micro-beams. By manipulating the shape of the field at the aperture plate, field curvature can be corrected, so the array of micro-beams focuses in a flat plane (fig. 2.3c).

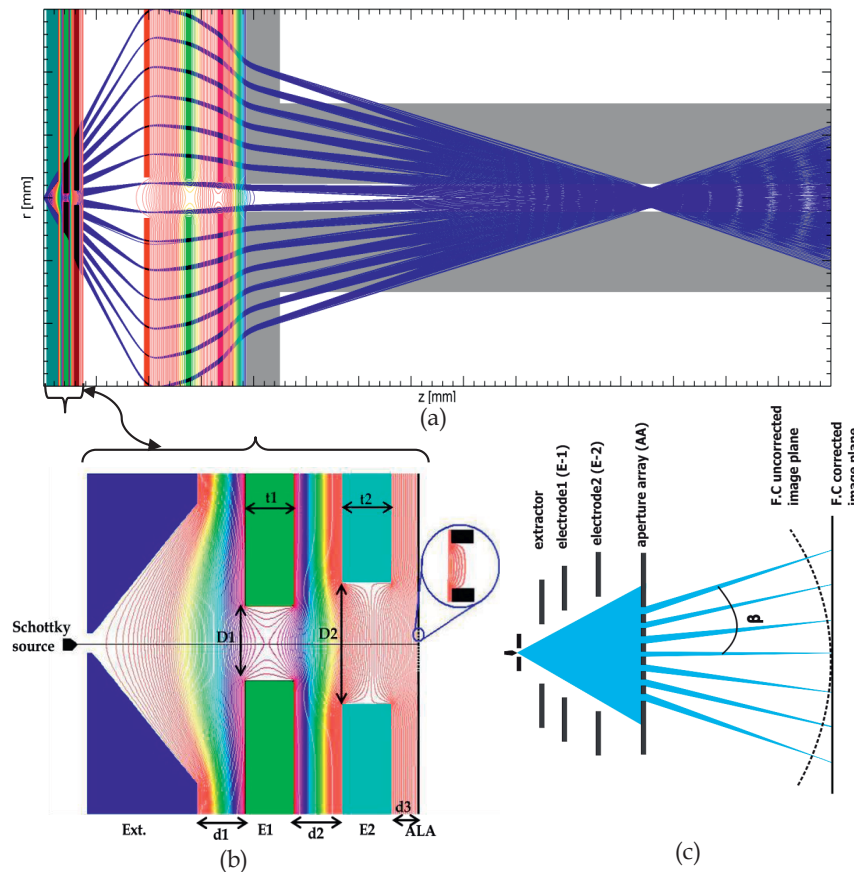


Figure 2.3a) The multi beam source module configuration including MBS and ACC configuration, the equi-potential lines and real rays modeled using EOD. Note that the rays are magnified by 70x in the radial direction for better visibility. Figure 2.3b) MBS configuration modeled using EOD. Figure 2.3c) a schematic of the concept of field curvature correction in the MBS image plane.

Chapter 2.

The correction of the field curvature is one of the essential and unique characteristics of this design. By careful manipulation of the shape of the field at the aperture plate, which is actually done by adjusting the voltages of the electrode-1 (E-1) and electrode-2 (E-2), it is even possible to introduce intentionally some amount of field curvature in the MBS image plane to compensate for any possible field curvature of the other lenses in the rest of the SEM column. In the latter case of course it should be in combination with a slight defocus of the aperture lens array to keep the macro lens strength “zero”.

Table 2.1 and 2.2 summarize the optimized electro-mechanical and electron optical parameters of the MBS.

Table 2.1 Optimum values of Electro-mechanical parameters of the MBS.

parameter	Value
V_{ext} (V)	5000
V_{E-1} (V)	11200
V_{E-2} (V)	2500
V_{AA} (V)	1500
D_1 (mm)	1.4
D_2 (mm)	2.3
D_{AA} (μ m)	18
$t_1=t_2=d_1=d_2$ (mm)	1.0
d_3 (mm)	0.7
pitch(μ m)	25

Table 2.2 Axial performance of the MBS.

Parameter	Value
Z_{source} (mm)	0
Z_{izsl}^* (mm)	0.57
Z_{ALA} (mm)	7.5
Z_{imbs} (mm)	19.8
M_{mbs}	3.16
M_{gmbs}	0.58
C_{smbs}^{***} (mm)	7.1
C_{cmbs}^{***} (mm)	36

*virtual image position of the ZSL.

**image side spherical and chromatic aberration coefficients of the MBS.

This MBS creates an array of focused beams with a geometrical probe size of 95 nm. Thus for a Schottky source, the typical probe current of each beamlet is 0.8nA. Now, the main question is: how many sub-beams can be produced by this MBS? The most important criterion for sub-beams is that they all should have the same size and current. To have sub-beams of the same size is, to a large extent, guaranteed by a design of the MBS where the aberrations are well controlled. However, obtaining multiple sub-beams with identical probe current also demands identical axial and off-axial performance

of the Schottky source. The angular current density and virtual source size of the electron source determines the probe size and its current. Therefore, for the off-axis beams to have the same properties as the axial beams, the Schottky electron source must fulfil these two important requirements: 1) the variation in angular intensity, within the range of emission angles, used to obtain multiple beams, must stay reasonably constant and 2) the virtual source size as seen from the extractor for off-axis beams must be equal to the axial virtual source size. It has been shown that for a constant temperature and extraction voltage, the virtual source size of the Schottky emitters is constant up to 120mrad emission cone angle [26, 27]. Previous and recent measurements on the angular intensity of Schottky electron sources also reveals that indeed the angular current density varies with different emission cone angle and the amount of the variation strongly depends on the extraction voltage [26,27]. Figure 2.4 shows the result of one of these typical measurements. It can be seen that the shape of the curve varies with the extraction voltage; however for an extraction voltage of about 5 kV, which is the extraction voltage used for our Schottky source, the variation in angular intensity is negligible for an emission cone half-angle of less than 4 degrees. It is therefore clear that the main limiting factor for the off-axial performance of the Schottky electron source is the angular intensity which is not constant for emission cone angles of larger than ~ 70 mrad. This restriction poses a boundary limit on the total number of sub-beams extractable from the MBS. With a "safe" half cone angle of 30 mrad and a distance of about 7.5mm between the Schottky emitter and aperture lens array, the total area on the aperture lens array plane for which the angular current density is reasonably constant is about $450 \times 450 \mu\text{m}^2$. With an $18 \mu\text{m}$ diameter of each aperture lens we decided to have a pitch of $25 \mu\text{m}$ between the aperture lenses.

The compromise involves three different parameters: To have as many beams as possible in the column, to have a reasonably large pitch at the wafer and also to have enough separation between the focused beams at the MBS

image plane. The latter was of prime importance for a later incorporation of an array of individual beam blanking deflectors at this plane.

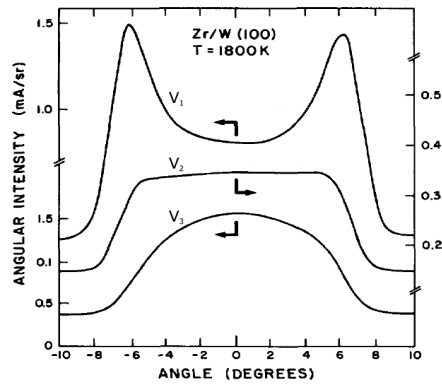


Figure 2.4 Measured angular intensity of a Schottky electron source with a tip radius of $0.8\mu\text{m}$ for different extractor voltages where $V_1 > V_2 > V_3$ and $V_1 = 4600\text{V}$. (from [26]).

With a pitch of $25\mu\text{m}$ this separation is only $70\mu\text{m}$ which was considered to be just enough to accommodate the MEMS electrodes and required wiring of the deflectors. Considering the total permitted area at the aperture lens array and a pitch of $25\mu\text{m}$ and the angular magnification of the zero strength lens (which is slightly larger than one) a total number of 196 beams, or an array of 14×14 , can be extracted from this MBS.

2.3 Multi beam source tolerance

In the previous sections the electron optics of the multi beam source was briefly discussed. It was mentioned that the combination of the zero strength lens and MEMS apertures creates an array of aperture lenses. The zero strength lens is designed such that its axial aberrations are smaller than the virtual source size of the Schottky source and by changing its strength it is possible to tune the shape of the field at the apertures plane. By changing the shape of the field in the apertures plane it is then possible to manipulate the curvature of field in the MBS image plane. This means that, it is possible to

correct the curvature of field of the multi beam source at its image plane or even correct the curvature of field of the whole MBSEM system by introducing extra opposite curvature of field at the MBS image plane.

The design presented there is valid only for an ideal situation and as is usually the case, electron lenses are not ideal. All electron lenses suffer from mechanical misalignments. These mechanical misalignments spoil the axial symmetry of the lens and thus the optical performance. The mechanical misalignments can be either due to mechanical imperfections as introduced during the fabrication of the electrodes, e.g. un-roundness, or inaccuracies introduced while assembling and fixing the components together, such as shift and tilt between electrodes. Although it is impossible to avoid misalignments completely, it is possible to minimize their destructive effects by introducing strict tolerances during fabrication and assembly of the elements. This, however, is very time consuming and costly and it may well be that for some specific elements such strict tolerances are not required. It is therefore very useful to determine the effect of misalignments on the electron optical performance of the lens quantitatively.

In general it isn't straightforward to calculate very accurately the effect of misalignments on the performance of the lenses. This is because the problem requires a full 3D simulation packages or 2D packages based on perturbation principle and mostly there isn't an appropriate software package to calculate the field. For this reason, making a simplified model and finding the maximum allowed misalignments quantitatively is an attractive alternative.

The objective of this section is to find the maximum allowed misalignment of the MBS. Here we consider three sources of misalignment: i) the un-roundness of the electrodes as introduced during the fabrication, and ii) the lateral shift and iii) the tilt of the individual electrodes during assembling and fixing the individual components.

2.3.1 Problem description

The apparent consequence of any misalignment in the MBS components is twofold: a change in the electric field at the plane of the aperture lenses, which changes the strength of the aperture lenses, and the change in the position and quality of the image of the zero strength lens. These two however have different consequences on the array of images produced by the aperture lenses. For instance, as a result of E_2 electrode tilt, the following consequences are expected: aperture lenses that are closer to the tilted electrode will be stronger than those that are further away; the position of the zero strength lens image (Z_{iZSL}) is tilted and moves off-axis. The latter by itself leads to an enlarged (blurred) object with different distances to the aperture lenses (different incident angle to the aperture lenses).

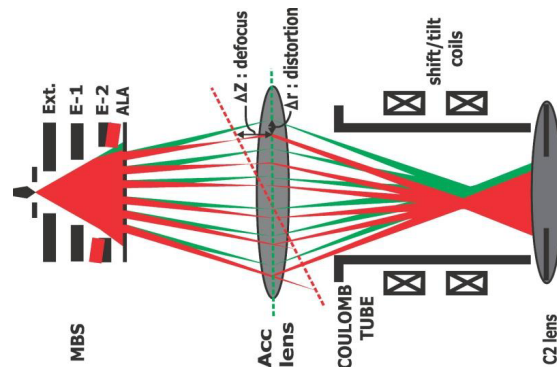


Figure 2.5 Schematic drawing of the MBS and the accelerator lens. The green beam-lets are for an ideal MBS and the red beam-lets are for a tilted E_2 electrode as shown in the figure.

The change in the strength of the aperture lenses will change the position of the image of every aperture lens compared to its ideal situation. Moreover, the change in the object position will also change the incidence angle of the beams in the aperture lenses leading to an extra off-axial aberrations and a distorted array of focused beams with different sizes produced by different aperture lenses. Finally, the shift of the image of the zero strength lens will add off-axial aberrations to it, especially coma which will be imaged and magnified by aperture lenses to their image plane.

Having different image planes for different aperture lenses effectively means that some of the beams experience under-focus while some others will have over-focus in the MBS Gaussian image plane. This leads to an axial shift between the focus planes of different aperture lenses represented by ΔZ_o which will be imaged onto the sample by the rest of the SEM column leading to an axial shift of ΔZ_i in the sample plane as:

$$\Delta Z_i = -M^2 \left(\frac{U_{MBS}}{U_{Sample}} \right)^{1/2} \Delta Z_o \quad (2.1)$$

Where M is the transverse magnification from the MBS image plane to the sample plane, U_{MBS} is the acceleration energy at the MBS image plane and U_{Sample} is the acceleration energy of the sample plane. The result of such an Over / under-focus is to enlarge the probe size at the sample. From the previous section we know that at an acceleration energy of 20 kV, for a 1 nm probe size the typical geometric probe size is about 0.5nm and the typical opening angle at the wafer is about 8mrad. If we allow an addition of only 10% of the geometric size contribution to the probe size due to this axial shift, the total allowed ΔZ_i will be only 7nm. This means that the maximum allowed ΔZ_o is about 70 μ m.

The un-roundness of the electrodes of the zero strength lens adds astigmatism to its image thus enlarging the geometric size of the object as seen by the aperture lenses. The un-roundness of the electrodes introduced during their manufacturing is not completely avoidable. However, there can be a maximum allowed range for this imperfection and that is defined as: The maximum allowed astigmatic blur added to the object of an aperture lens should about be 10% of the geometric size of the object.

2.3.2 Solution to the problem

As mentioned earlier, in general accurate misalignment calculations are not straightforward. In the case of the MBS, the large span of dimensions in the components, ranging from millimetres in the macro electrodes to only tens of microns in the aperture lenses makes it even more complicated to use 3D

programs directly. This is because to get reasonably accurate field calculations, extremely small meshes of only a few microns have to be defined in a relatively large volume. This makes it impossible to calculate the field using these programs. To handle the problem, however, we have divided the MBS into two different lenses; a thick zero strength lens and an array of thin aperture lenses. The effect of misalignment of the zero strength lens can then be studied using 3D simulation programs where only small misalignments are considered, whereas for aperture lenses, thin lens approximations have to be used. We have used the CPO 3D program [28] to calculate the field and to trace particles. In the zero strength lens, the effect of the electrode (s) lateral shift and tilt with respect to the common optical axis of the lens are studied separately and independently and in the end the net effect of each step is added together in quadrature.

For any electrode tilt or shift, using a CPO 3D program, the following steps have been taken:

- The two rays of $r_\alpha(z)$ and $r_\beta(z)$ with the initial condition in the object plane (z_o) of $r_\alpha(z_o) = 0$, $r'_\alpha(z_o) = 1$ and $r_\beta(z_o) = r'_\beta(z_o) = 0$ (thus $r_\beta(z)$ is just the optics axis) is calculated.
- The electric field ($E_r(x, y, z_{ALA})$) at a plane just in front of the aperture lenses is calculated.

Using these two rays, the position of the virtual image of the zero strength lens, the position of the object as seen by the aperture lenses, is found. Having found the position of this image, the object distance of each aperture lens, the incidence angle at every aperture lens and the off-axial distance in the principle plane of the zero strength lens is calculated accordingly.

Figure 2.6 and 2.7 show two examples of these rays and corresponding parameters. Figure 2.6 shows the effect of E_2 shift along +r direction (Note: in fact the shift has occurred in the x-y plane along a line having 45degree angle with both axes, however for simplicity we explain it in 2D and r-z coordinate system). Two rays as described above are produced using CPO 3D. The green rays are for an ideal zero strength lens whereas two red rays are for a zero

strength lens with shifted E_2 . The asymptotes to these rays show the position of the image in both cases. As can be seen, an E_2 shift leads to a radial shift (dr) of the image. The position of the image is calculated by the parameters shown in the figure (namely r_t , z_t and α_t). The radial shift in the image position changes the inclination angle to the aperture lenses as can be seen from the figure which leads to different off-axial aberration contributions from aperture lenses and distortion in the image of the array compared to the ideal case. Moreover, the off-axis distance at the object principle plane of the lens (r_{Ho}) is shown in the figure which leads to an off-axial aberration contribution, especially coma to the zero strength lens image.

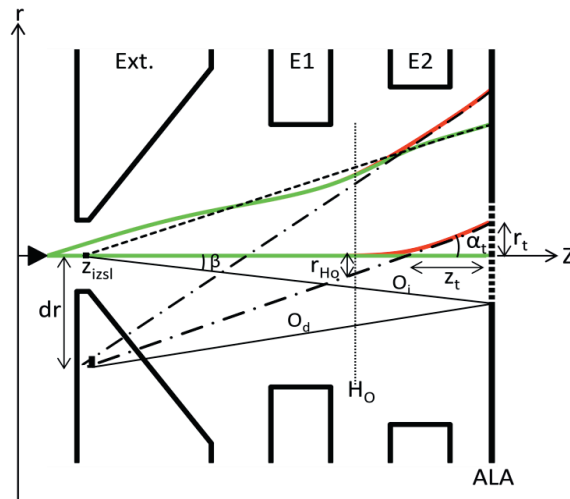


Figure 2.6 the effect of E_2 shift along $+r$ direction. The green rays are two rays for an ideal zero strength lens whereas two red rays are for zero strength lens with shifted E_2 . An E_2 shift shifts the position of the zero strength lens image (Z_{izsl}) off-axis by dr , making the incidence angle to the aperture lenses different than its ideal value.

The coma contribution to the zero strength lens image is a consequence of the spherical aberration of the zero strength lens and the off-axial appearance of its image to the aperture lenses. The maximum allowed contribution of the coma as seen by the aperture lenses should be 10% of their object size. However, to be able to use 3D program accurately, the aperture lenses have to be excluded. This means that we should translate the requirement on the

coma contribution to zero strength lens optical parameters. The maximum opening angle of the beam cone of the Schottky source needed to illuminate the aperture lenses is 34mrad. The maximum allowed blur introduced by coma should then only be 10% of the geometric size of the zero strength lens image. With some simple mathematics, it can be shown that the tilt/shift induced coma contribution is:

$$d_{CO}(50) = \frac{C_{si}(\infty)}{f^4} v^3 \beta^2 r_{Ho} \quad (2.2)$$

Where $d_{50}(50)$ is the FW50 disc size of the coma, $C_{si}(\infty)$ and f are the image side spherical aberration coefficient and the image side focal length of the zero strength lens respectively, v is the distance from the tip to the object principle plane of the zero strength lens and β is the maximum opening angle of the beam cone illuminating the whole aperture lenses. It should be mentioned that for in fact for the calculation of coma as induced by different electrodes misalignment, the accumulative spherical aberration coefficient up to the position of that electrode has to be taken into account not the total spherical aberration coefficient of the ZSL. This formula therefore over estimates the size of misalignment induced coma.

The same calculations are done for E_1 and extractor shift. It should be mentioned that the effect of the extractor shift on the virtual source of the electron source has not been taken into account here. Figure 2.7 shows another example where the effect of the E_1 tilt is considered. The E_1 is tilted around the x-axis at the point Z_1 as shown in figure 2.7. Similar to the previous case, again two rays are produced using CPO 3D. The green rays are for an ideal zero strength lens whereas two red rays are for zero strength lens with tilted E_1 . The asymptotes to these rays show the position of the zero strength lens image in both cases.

The same calculations are done for E_2 and extractor tilt. It should be mentioned that the effect of the extractor tilt on the virtual source of the electron source has not been taken into account here.

With the previous simulations, the position and the size of the object for the aperture lenses are calculated. If we calculate the aperture lens strength, the

have to be then compared with this reference instead of the paraxial calculations of the electron optical parameters.

Figure 2.8 shows a result of such typical calculations. In this figure the image distance of the aperture lenses for an ideal MBS is compared with two distinct misaligned situations: the E_2 electrode is shifted by $15\mu\text{m}$ along the radial direction, and the E_2 is tilted by 0.3 degree. In this figure the numbers on the “ r ” axis correspond to the position of the aperture lenses in r - z plane. Therefore every labelled point in the graph corresponds to an aperture lens position and its image distance. As can be seen, the image plane of the ideal MBS has already a small intentionally induced curvature of field. Electrodes shift or tilt introduces an axial shift of ΔZ_{max} , as defined in the figure.

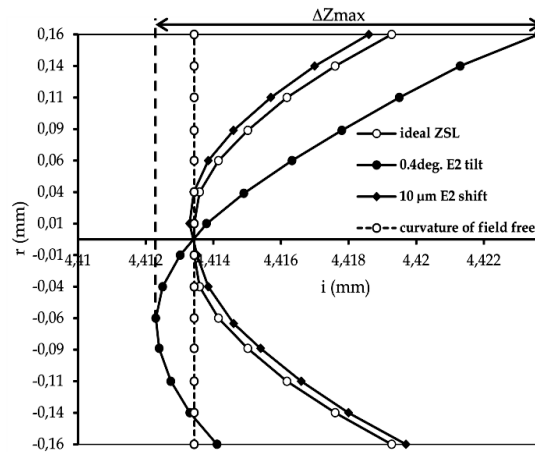


Figure 2.8 the image distance of the aperture lenses for an ideal MBS is compared with two distinct misaligned situations: the E_2 electrode is shifted by $15\mu\text{m}$ along the radial direction, and the E_2 is tilted by 0.3 degree. The r -axis shows the position of the aperture lenses and the i -axis shows the image position of the aperture lenses. That is, every labeled point in the graph corresponds to an aperture lens position and its image distance. The ideal MBS has already a small intentionally induced curvature of field. Electrodes shift or tilt introduces an axial shift of ΔZ_{max} , as defined in the figure.

Electrodes shift or tilt introduces an axial shift of ΔZ_{max} , as defined in the figure. This ΔZ_{max} is calculated independently for any electrode tilt and shift.

As already mentioned, any misalignment changes the incidence angle of the beams in the aperture lenses leading to an array of focused beams with different sizes due to different contributions of off axial aberrations. This will

also introduce a boundary limit on the tolerances of the MBS components. The routines on how to calculate the off-axial aberrations of the MBSEM will be explained in chapter 3. Here we only present the results of off-axial aberration calculations as induced by misalignments.

2.3.3 Roundness of the electrodes

With exactly the same line of reasoning and explanations for the calculation of the coma contribution to the object of the aperture lenses, the maximum allowed contribution from astigmatism introduced by un-roundness of the electrodes as seen by the aperture lenses can be expressed in terms of zero strength lens image size and can therefore be calculated excluding aperture lenses in the simulation. We therefore calculate the size of the astigmatic blur (appeared as an ellipse) for different degree of electrodes ellipticity and compare the produced blur with the axial image size of the lens.

The size of the blur, the larger radius of the ellipse, is calculated as follows: A principle ray, $r_\alpha(z)$, is produced for an ideal case and for a case where one of the electrodes has a slightly larger or smaller radius by an amount dr . Using $r_\alpha(z)$ the position of the images are found. For instance for E_2 with a larger radius the image shifts by ΔZ towards the ALA. By this shift the radius of the ellipse, $\Delta r = \beta \cdot \Delta Z$, is calculated (see figure 2.9).

This is repeated for E_1 and Extractor and the resulting ΔZ is added in quadrature ($\Delta z = \left((\Delta z_{Ext}^2)^2 + (\Delta z_{E1}^2)^2 + (\Delta z_{E2}^2)^2 \right)^{\frac{1}{2}}$).

With a Schottky virtual source size of 30nm, the geometrical source size of the zero strength lens image is about 52nm. This means that if Δr is smaller than about 27nm, out of roundness of the electrodes are acceptable. That is the maximum allowed shift, ΔZ_{max} , should be less than 0.8 μ m.

2.3.4 Tilt of aperture lenses plane

As mentioned earlier, the aperture lenses are assumed to be simple thin lenses. The tilt in the aperture lens array plane can have two distinct effects:

axial shift and tilt of the aperture lenses from their ideal position. The axial shift results in the strength change of the aperture lenses.

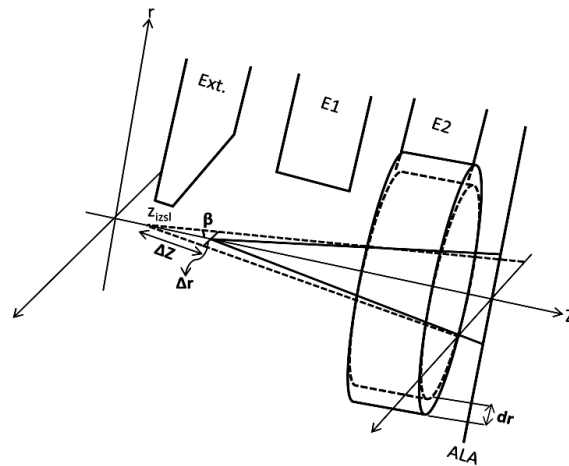


Figure 2.9 the effect of electrode out of roundness on the size of the image of the ZSL (Z_{iZSL}) as seen by the aperture lenses.

For instance if tilt is around x-axis and clockwise, the aperture lenses in the first and second quadrant of the ALA plane get weaker and the aperture lenses in the third and fourth quadrant get stronger (with respect to the ideal case). This problem can be simply treated using ZSL lens model and CPO 3D, the same way as described for tilt and shift of other electrodes. But the effect of aperture lens tilt is to introduce additional ΔZ to the MBS image plane and cannot be modelled using CPO 3D. It can be simply shown that for a thin aperture lens the amount of ΔZ induced by a tilt of the aperture lens is:

$$\Delta Z = \frac{1}{2}(M^2 + M)v_{ALA}\theta^2 \quad (2.4)$$

Where $M = (M_{MBS}/M_{ZSL})$ is the magnification of the aperture lens, v_{ALA} is the object distance of the aperture lens and θ is the tilt angle. It can be seen that this effect is extremely small compared to that of shift of the ALA plane.

For example, for a ALA plane tilt of 5mrad, the shift induced ΔZ in the MBS image plane is about 10 μ m while the ΔZ induced by the tilt of the aperture lens is less 1 μ m.

2.3.5 Results and discussions

Figure 2.10a shows the effect of the electrodes radial shift on the ΔZ_{\max} . In general, the effect of the shift of the electrodes is not as critical as the effect of their tilt. The shift of the E_1 and the extractor can be acceptable up to $20\mu\text{m}$ whereas for the E_2 the shift has to be kept below $15\mu\text{m}$. It should be mentioned that the shift of the ALA plane w.r.t to the optical axis is irrelevant here. The reason is that with ALA shift only the number of beams will be less (some beams are missing) and has no effect on the electron optical performance of the MBS. Figure 2.10b shows the variation of the ΔZ_{\max} as a function of electrodes tilt. It is strongly dependent on the E_2 and aperture lens array plane (ALA) tilt. A tilt of even 0.4 degree is acceptable for E_1 and Extractor whereas the maximum allowed tilt for E_2 and ALA is about 0.2 degrees or even smaller.

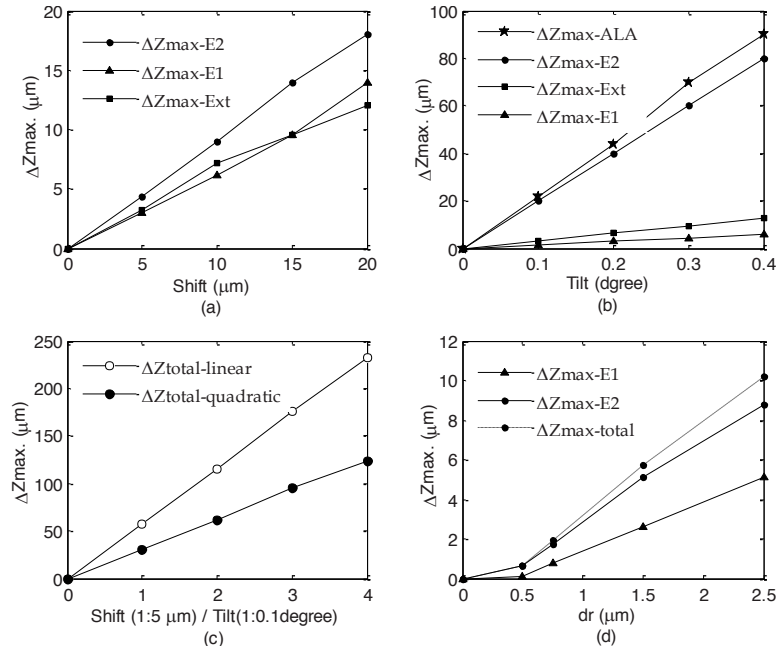


Figure 2.10-a) Variation of ΔZ_{\max} . as a function radial shift of different electrodes. b) Variation of ΔZ_{\max} . as a function of tilt angle of different electrodes. c) Variation of total ΔZ_{\max} as a function of electrode tilt and shift. The ΔZ_{total} is the addition of all ΔZ_{\max} produced by electrode tilt and shift added up in two forms of linear and in quadratic. d) Variation of ΔZ_{\max} as a function of out of roundness of the electrodes of the ZSL.

Figure 2.10c shows the total ΔZ_{\max} as a function of electrode tilt and shift. In this figure, total ΔZ_{total} is the addition of all ΔZ_{\max} produced by electrode tilt and shift. The addition is done in two ways: linear addition and quadratic addition. The reason is that, for the same amount of shift or tilt the sign of the ΔZ_{\max} is not the same. For instance in the case of the shift, the effect of E_1 is opposite to that of Extractor and E_2 and in the case of tilt the effect of Extractor is opposite to that of E_1 and E_2 .

For the maximum allowed ranges of tilt and shift as discussed above, the contribution of coma is found to be smaller than the geometric size of the ZSL image and also in this range of misalignment the variation in the sizes of the focused beam at the MBS image plane due to different off-axial aberration contributions (different inclination angle) is found to be below 10%.

Figure 2.10d shows the result of the out of roundness calculations for different electrodes of the zero strength lens. It shows the individual and total ΔZ corresponding to different dr of different electrodes in the ZSL. As can be seen from the figure, controlling the out of roundness of the E_2 electrode below $1.5\mu\text{m}$ ($dr \leq 0.75\mu\text{m}$) is crucially important, whereas for E_1 this is slightly relaxed to $dr \leq 1\mu\text{m}$. The out of roundness of the extractor is even more relaxed with respect to that of E_1 and E_2 . It should be noted that the effect of the out of roundness of the extractor on the virtual image quality of the source has not been taken into account. With such tolerances, the field change at the ALA plane is remarkably small compared with the change induced by electrode shift and tilt and therefore its effect on the performance of the aperture lenses is neglected.

Note: we expect the out of roundness of the aperture lenses fabricated by MEMS technique is negligibly small.

2.4 Coulomb interactions

In general, the Coulomb forces that an electron experiences in the electron beam are twofold: The space charge and individual statistical interactions. The space charge effect only results in a defocus which ultimately can be

corrected by refocusing the beam [29]. The statistical interactions on the other hand will degrade the brightness and the energy spread of the beam. The brightness loss is the result of transversal e-e interactions in the beam known as “trajectory displacement” effect, whereas the increase in the energy spread is related to the longitudinal interaction of the electrons in beam known as “Boersch effect”. The most accurate calculations of the trajectory displacement and Boersch effect in electron optical systems can only be done using a simulation based on Mont Carlo programs. To get quantitative estimates of the interactions, however, there have been developed a couple of analytical calculation methods. Most of these only have a limited purpose or specific beam geometries [29]. Only the model described by Jansen, is more complete and applicable for wider range of beam geometries [30]. Jansen’s analytical equations are based on the so called extended two-particle approximation. In this model the beam segments are assumed to be at a constant potential and depending upon the beam volume density at every section of the beam envelope, a variety of regimes can be distinguished [30]. Tiemeijer has developed a program based on Jansen’s model to calculate the trajectory displacement and Boersch effect in his Wien-filter monochromator [29]. The program in fact divides the beam in infinitesimally short slices whose potential and diameter are assumed to be constant. It then calculates the FW50 size of the deviations in the trajectory and energy of the beam of every slice using Jansen’s expressions for pencil and Holtzmark regimes and finally the FW50 values corresponding to either of the regimes is added up [30]. This is repeated throughout the complete beam and the total trajectory and energy deviation is then found by integrating over all beam slices. The trajectory displacement is translated back into the virtual source by including the magnification of the lenses, deceleration and / or acceleration of the electrons. The more detailed explanation of the theory behind this program as well as the results of simulation against experimental measurements is presented elsewhere [29].

With slight simplifications and approximations, we can make use of Tiemeijer's program to calculate the interactions in our MBS. The reason for necessary simplification and approximation is as follows: if one would have only considered the central aperture lens, the beam envelope was axially symmetric and therefore Jansen's equations could have been used in a straightforward way. However, it is not only the interaction between the electrons in their individual beam-let but also the interaction between the neighbouring beam-lets. In fact it is easy to understand that the latter is of prime importance; the current of each beam-let is about 0.8nA, which is usually small enough to have no considerable Coulomb interactions. However, the current in all beam-lets together is 157nA ($=196 \times 0.8\text{nA}$). Therefore the interaction between the neighbours is much larger compared to that in the individual beam-let. To calculate the interaction between the neighbouring beam-lets is not in the scope of Jansen's model. We therefore divide the MBS into two sections; the first section being from the tip to the aperture array plane for which the program can be used directly. For the second section, being from aperture lens array plane to the MBS image plane, Jansen's equations can't be used directly. For this section we have to assume a circular beam of diameter equal to the size of the diagonal of the whole aperture lenses area with a uniformly distributed total current of 157nA (as total current transmitted through the aperture lens array) and calculate the interactions using Tiemeijer's program. We believe that this might slightly underestimate the situation but gives a reasonable understanding about the interactions. The result of the calculations is as follow: the increase in the virtual source size due to the trajectory displacement in the first section of the MBS is 4.9nm whereas the increase in the virtual source size due to the trajectory displacement in the second section of the MBS is only 2.1nm. Therefore, the total increase in the virtual source size due to the trajectory displacement in the MBS is only 7nm (if the different contributions from different sections are added up linearly) which is small compared to a virtual

source size of approximately 30 nm. The calculated interactions in the rest of the column will be presented in chapter 3.

2.5 Summary

In this chapter the various options for the multi beam source that were found in the literature were very briefly discussed. The traditional combination of collimator lens and micro-aperture Einzel lens cannot be used as a multi beam source for high resolution and high throughput MBSEM. The old design of the multi beam source module was put aside and a new design free from all previous problems was proposed. A very brief summary of the electron optical design of the MBS was presented and the maximum number of achievable sub-beams was calculated. The required tolerances of every component in the MBS is calculated and discussed and at the end the effect of Coulomb interactions on the performance of the MBS is studied.

2.6 Bibliography

- [1] E. Yin, et al., *J. Vac. Sci. Technol. B* 18 (2000) 3126.
- [2] S.Tanimoto, et al., *Jpn. J. Appl. Phys.*, part 1 42 (2003) 6672.
- [3] S.T.Coyle et al, *J. Vac. Sci. Technol. B* 22 (2004) 501.
- [4] H. Yasuda, et al., *J. Vac. Sci. Technol. B* 14 (1996) 3813.
- [5] G. Winogard, et al., *J. Vac. Sci. Technol. B* 18 (2000) 3052.
- [6] M. Muraki and S.Gotoh, *J. Vac. Sci. Technol. B* 18 (2000) 3061.
- [7] N. Nakasuji, et al., *Jpn. J. Appl. Phys.* 44 (part 1) (2005) 5570.
- [8] O. Kamimura, et al., *J. Vac. Sci. Technol. B* 25 (1) (2007) 140.
- [9] A. J. van den Brom, et al., *J. Vac. Sci. Technol. B* 25 (6) (2007) 2245.
- [10] M. Manko et al., *J. Vac. Sci. Technol. B* 18(6) (2000) 3010.
- [11] X, Jiang et al., *J. Vac. Sci. Technol. B* 16(6) (1998) 3374.
- [12] M. Wieland et al., *Microelectron. Eng.* 57-58 (2001) 155.
- [13] D. Schroder et al., *IEEE Trans. Electron Devices* 21 (12) (1974) 785.
- [14] T. Teepen et al., *J. Vac. Sci. Technol. B* 23(2) (2005) 359.

Chapter 2.

- [15] W. Hofmann, et al., *J. Vac. Sci. Technol. B* 13(6) (1995) 2701.
- [16] Y. Yamaoka, et al., *Jpn. J. Appl. Phys.* 35 (1996) 6626.
- [17] J.-Y. Park et al., *J. Vac. Sci. Technol. B* 15(6) (1997) 2749.
- [18] G. Guo et al., *J. Vac. Sci. Technol. B* 19(3) (2001) 862.
- [19] A. J. van den Brom et al, *J. Vac. Sci. Technol. B* 25(6) (2007) 2245.
- [20] M. J. Van Bruggen et al, *J. Vac. Sci. Technol. B* 23(6) (2005) 2833.
- [21] P. Kruit, Publication No. US2007029509.
- [22] M. J. Van Bruggen et al, *J. Vac. Sci. Technol. B* 27(1) (2009) 139.
- [23] Y. Zhang, PhD Thesis, Delft University of Technology, (2008).
- [24] M. J. van Bruggen, PhD Thesis, Delft University of Technology (2008).
- [25] B. Lencova, J. Zlamal, Electron Optical Design program package EOD 3.069.
- [26] D. Toggle, L. Swanson, *J. Vac. Sci. Technol. B* 3(1) (1985) 220.
- [27] M.S Bronsgeest, PhD Thesis, Delft University of Technology (2009).
- [28] CPO Programs, <http://www.electronoptics.com>
- [29] P. C. Tiemeijer, *Microelectron. Eng.* 78 (1999) 53.
- [30] P. Kruit, G. H. Janssen, *Handbook of Charged Particle Optics*, CRC press, New York, 1997.

3 CHAPTER

Electron optics of multi beam scanning electron microscope

“Mathematics is the tool specially suited for dealing with abstract concepts of any kind and there is no limit to its power in this field. “

Paul Dirac

This chapter addresses the electron optics of the multi beam scanning electron microscope in three distinct parts. Throughout part I a detailed description of the axial and off-axial electron optics calculations of the MBSEM, plus the results of electron optics calculations for a specific setting of the system is presented. In part II the possibilities and limitations of very high resolution MBSEM with different magnifications for different acceleration energies is presented. Part III presents the possibilities and limitations of larger pitch and higher probe current MBSEM with moderate resolution.

3.1 Electron optics of multi beam scanning electron microscope: Part I¹

3.1.1 Abstract

We have developed a Multi Beam Scanning Electron Microscope (MBSEM), which delivers a square array of 196 focused beams onto a sample with a resolution and current per beam comparable to a state-of-the-art single beam SEM. It consists of a commercially available FEI Nova-nano 200 SEM column

¹From “A. M.-Gheidari and Pieter Kruit, NIMA 645 (2011) 60” with slight modifications in the orders of the sub-sections in order to make the storyline of thesis more consistent.

equipped with a novel multi-electron beam source module. The key challenge in the electron optical design of the MBSEM is to minimize the off-axial aberrations of the lenses. This article addresses the electron optical design of the system and presents the result of optics simulations for a specific setting of the system. It is shown that it is possible to design a system with a theoretical axial spot size of 1.2 nm at 15 kV with a probe current of 26 pA. The off-axial aberrations for the outermost beam add up 0.8 nm, increasing the probe size to 1.5 nm.

3.1.2 Introduction

Charged Particle lithography and microscopy instruments are key tools in science and industry. Scanning electron microscopes can reach resolutions below 1nm. The acquisition time for noise-free high resolution images of 10^6 pixels is typically in the order of seconds. When used for patterning, the writing time for 10^6 pixels is almost in the same order of magnitude. For some applications, both in patterning and in imaging, this is too slow. However, the current in a single beam cannot easily be increased without degrading the resolution due to the limited reduced brightness of the electron source. Multi-beam systems can enhance the throughput by several orders of magnitude.

Many approaches have been tried to make multi-electron beam systems over the last decades [1-11]. There are basically two major challenges for multi-beam systems: to find an appropriate electron source, and to focus multiple beams onto the sample. In the single column/single source approach [7-12], which we will adopt, multiple beams are created by splitting the wide angle beam of a single source into many sub-beams, forming an intermediate focus using a micro-fabricated lens array. A single column with common cross-overs of all beams is then used to focus the beams onto the sample.

For splitting up a single source, two kinds of sources have been used so far: LaB₆ sources and dispenser type cathodes [12]. Both emitters provide a very high current but for high resolution applications the brightness is too low.

We have developed a multi-beam scanning electron microscope (MBSEM) as a tool for fast and high resolution patterning through Electron Beam Induced Deposition (EBID), with a resolution down to 1 nm, similar to a state-of-the-art single beam SEM. This system is currently able to deliver 196 focused beams onto the sample [13]. The instrument may also be used for high throughput ordinary resist-based electron beam lithography, and for fast imaging (the latter, of course, only after a suitable detector has been developed). To develop a high resolution MBSEM, we have used a commercially available column of a Nova-nano 200 SEM (FEI Company) and designed a novel multi-beam source module that splits the beam of a high brightness Schottky source. A consequence of using a single column system to image the multiple beams is that electron beams have to travel off-axis through the SEM lenses. The key challenge in the electron optical design of the MBSEM is to minimize the off-axial aberrations of the lenses.

The objective of this article is to describe the electron optical design of the MBSEM and show the simulation results of the off-axial aberrations.

3.1.3 General design considerations for a multi beam-SEM

The electron optical design of the multi electron beam source to be used in the MBSEM was discussed in the previous chapter. It is possible to design and build a system with individual micro-columns for each beam. However, it is not easy to align all optical elements with respect to each other and direct the beams through each column. For high resolution applications, where the total beam current is relatively low, we can afford to have common cross-overs of the beams without deterioration of the beam quality as a result of electron-electron interactions. Thus, we choose to use a single column for transporting the output of the multi beam source to the target. When all 196 beams are focused by single lenses, it is obvious that most beams travel off-axially through the column. The off-axis aberrations of the lenses may then degrade the resolution of the system. Therefore the key challenge is now to minimize the off-axis contributions of the lenses. The simplest solution is to only place

lenses where all beams have a common cross-over, because at those points none of the beams is off-axis. However, then we need lenses to image one common cross-over to the next cross-over. If these “field lenses” are placed in the planes where the sub-beams are focused, that are in conjugate planes of the source and the sample, the off-axis aberrations cannot (in the thin-lens approximation) influence the resolution. The disadvantages of this solution are the large number of lenses that are needed and the rigidity of the system: once built, the magnification or probe-size cannot be changed anymore.

We have chosen a design in which only the last lens, the objective lens, is situated at a common cross-over, and only the first lens after the multi-beam source is a field lens. The reason for the first decision is that, just as in a conventional single beam SEM, the last lens of the MBSEM de-magnifies all aberration contributions of other lenses, so its own aberrations are dominant.

The reason for the second decision is that we expect that we can keep the off-axial distance of the beams smaller in the rest of the column than in this output plane of the source. In addition, this is the lens that needs to collimate the diverging beams from the source. From fairly simple first order estimates, one can find that chromatic deflection errors alone would be larger than the geometrical size of the source image if this lens is not in a conjugate plane of the source.

3.1.4 First-order optical system design

With the design principles set out in the previous paragraph, we can attempt to use a standard SEM. We had an FEI Nova-nano 200 SEM available, so to get a better understanding of the electron optical challenges involved in the design of a MBSEM let us look briefly at the electron optics column of the standard single beam SEM. Figure 3.1.1a shows a schematic drawing of electron optical configuration. In this system the single beam produced by a Schottky source is imaged by subsequent lenses to form a probe. The “gun lens” (C_1) and the C_2 lens make an intermediate image of the Schottky virtual source in front of the variable aperture (VA). The Coulomb tube (CT) is

surrounded by a set of coils to tilt and shift the beam to align it onto the optical axis of the system. The variable aperture is used to determine the beam opening angle. Further de-magnification is done by the intermediate lens (INT) and either the high resolution (HR) or magnetic immersion ultra high resolution (UHR) objectives lenses. Scan- and stigmation-coils are positioned between the intermediate lens and the objective lens.

For multi-beam operation the standard source module (dashed rectangle in fig. 3.1.1a) is replaced by multi beam source module.

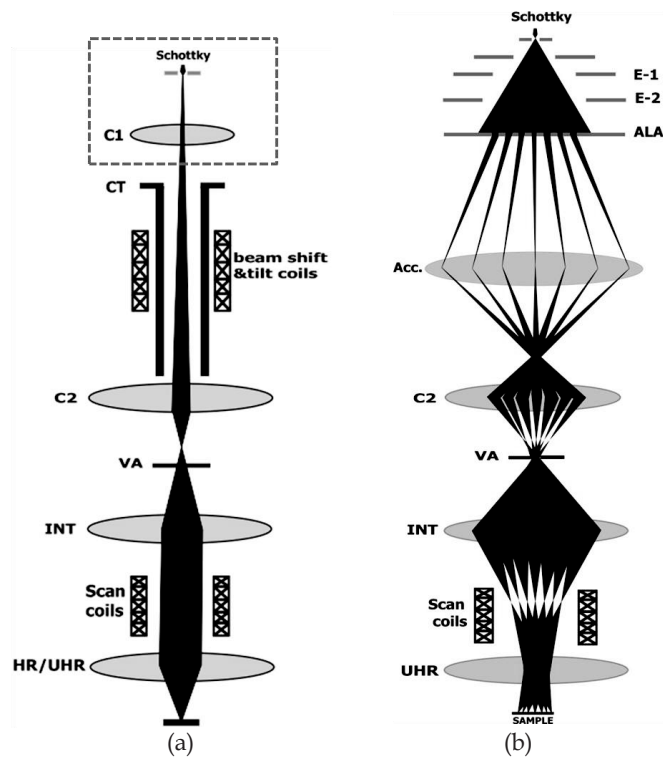


Figure 3.1.1 a) Schematic overview of electron optical configuration of the standard Nova-nano 200 SEM: b) Schematic overview of electron optical configuration of the MBSEM.

The multi-beam source needs to be coupled to the column with a coupling lens that also accelerates the beam to the required final energy. This is the field lens that was discussed in the previous paragraph. The design of this accelerating lens will be discussed in the next section. Figure 3.1.1b shows a schematic overview of the first order imaging sequence of the multi beam

SEM. The accelerating lens creates a common cross-over in front of the C_2 lens. The C_2 lens images this cross-over onto the variable aperture. The variable aperture thus determines the aperture angle for all beams, which avoids the problem of aligning a second aperture array to the beam array. By changing the strengths of the accelerating lens and the C_2 lens, the magnification of the system can be changed. The intermediate lens images the common cross-over into the coma-free plane of the objective lens. At the same time, the C_2 lens images the plane with focused beams in front of the variable aperture. The intermediate lens images this plane in front of the objective lens, and the objective lens creates an array of focused beams on the sample.

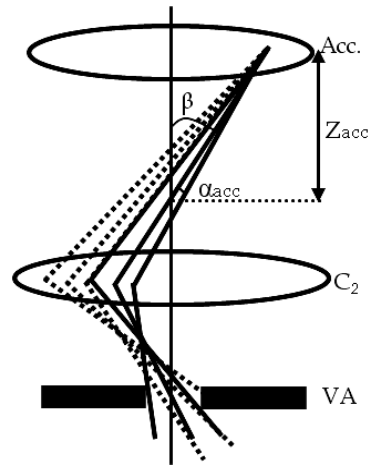
3.1.5 Accelerator lens design

The design of the accelerator lens needs some special attention. We mentioned that, because it is used as a field lens, its aberrations would not influence the resolution if it may be considered as a thin lens. However it should possess an acceptable spherical aberration coefficient for the imaging of the first common crossover. This is because the spherical aberration causes a spread in the position of the different beams in the common cross-over, making the cross-over not so “common” anymore. This spread will be imaged and magnified by the C_2 lens onto the variable aperture. The consequence is that part of the electron beams may not pass the variable aperture. For un-apertured operation, the spread will later be imaged and magnified by the INT lens leading to an off-axis position of the beams in the coma-free plane of the objective lens. It is possible to estimate the acceptable limit of the spherical aberration coefficient.

Figure 3.1.2 shows schematically the problem of crossover spread where the dashed beam suffers from spherical aberration of the accelerator lens. The maximum radial displacement of the position in the common crossover plane can be calculated as follows:

$$\Delta r = C_{si,Acc}\beta^3 \quad (3.1)$$

Figure 3.1.2 Schematic drawing of the problem of crossover spread due to spherical aberration of the accelerating lens where the outer dashed beam suffers from spherical aberration.



Where $C_{si,Acc}$ is the image side spherical aberration coefficient of the lens and β is the landing angle of the outer beam with respect to the optical axis.

If we assume that a shift of only 30% of the beam diameter is acceptable:

$$\Delta r = C_{si,Acc} \beta^3 < (\alpha_{Acc} Z_{Acc}) \cdot 30\% \quad (3.2)$$

Where α_{Acc} is the opening angle of the individual beams as shown in figure 3.1.2 and Z_{Acc} the z-position of the first crossover, measured from the plane of the accelerator lens. The 30% criterion implies that the largest variable aperture that can be used with a full filling for every beam selects a diameter of 70% of the total diameter, thus about 50% of the total current.

Figure 3.1.3 shows the multi-beam source module configuration as modelled by the EOD program [14]. It is composed of the actual multi-beam source and the accelerator lens. The accelerator lens consists of three electrodes with voltages of V_1 , V_2 and V_3 . The entrance of the Coulomb tube of the SEM is also a part of the lens. It accelerates the electrons from 1.5 keV energy at the MBS image plane to the desired working energy at the target. This is done by keeping the Coulomb Tube (CT) always at real ground potential; at positive potential with reference to the potential of the electron source. V_1 is fixed to 1.5 kV, which is the voltage of the aperture array. V_2 and V_3 can be changed to vary the system magnification. In our system we have chosen, for practical reasons, to make V_2 equal to the voltage of the extractor electrode of the source, thus fixing it at 5kV. So it is only possible to vary V_3 .

There are limitations to the range of crossover movements, for instance if it moves far away from the C_2 lens toward the accelerator lens, the pump aperture located at the C_2 lens starts cutting off the outer beams (see figure 3.1.4). More comprehensive results on system flexibilities and performances at different magnifications shall be discussed in the forthcoming parts of this chapter. This electrode configuration gives a $C_s=21\text{m}$ for acceleration to 15kV. With $\beta=7.1\text{mrad}$, $\alpha_{\text{acc}}=0.2\text{mrad}$ and $Z_{\text{acc}}=104\text{mm}$, we find $\Delta r=7.6\mu\text{m}$ and the size of the beam ($2\alpha_{\text{acc}}Z_{\text{acc}}$) = $42\mu\text{m}$, so that the displacement is within our requirement of 30% of the beam size.

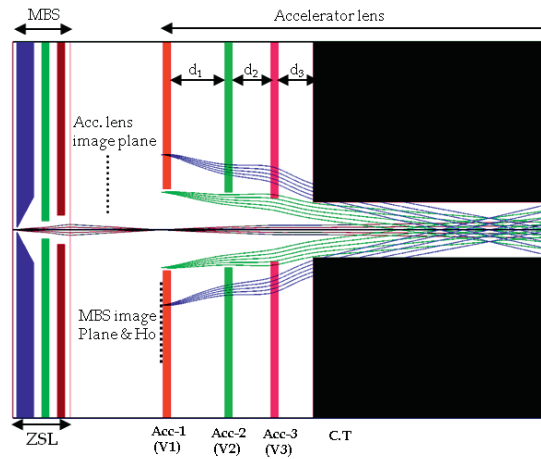


Figure 3.1.3 Multi beam source configuration modeled using EOD, consisting of the MBS and the accelerator lens. The axial ray presents the imaging sequence of the MBS and accelerator lens for the central beam, whereas the off-axis rays present the imaging of the array by accelerator lens from MBS image plane. The accelerator lens images the array of focused beams produced by the MBS to a virtual image as is shown by the red dashed lines.

In the fabrication, assembly and aligning of the accelerator lens components, tough not necessary, but for convenience, we applied the same tolerances used for the MBS elements. These tolerances for the MBS were discussed in the previous chapter.

Table 3.1.1 summarize the optimized electron optical and mechanical parameters of the accelerator lens.

Table 3.1.1 Optimum values of electron optical and mechanical parameters of the lens.

parameter	Value
V ₁ (V)	1500
V ₂ (V)	5000
V ₃ (V)	Variable*
V _{C.T} (V)	Ground
D _{V1} (mm) **	6.5
D _{V2} (mm)	6.0
D _{V3} (mm)	5.0
d ₁ (mm)	7.0
d ₂ (mm)	5.0
d ₃ (mm)	4.5

* For different magnification and different energies.

**Diameter of the electrodes.

Note: The thickness of the electrodes is 1mm.

3.1.6 Optics simulations of axial performance (method)

The axial probe size, d_{axial} , containing 50% of the total current is calculated using the RPS algorithm proposed by Barth and Kruit [15]. It should be noted that the FW50 measure for the probe size calculation will be used throughout this paper unless otherwise mentioned:

$$d_{axial} = \left\{ [d_l^{1.3} + (d_\lambda^4 + d_s^4)^{1.3/4}]^{2/1.3} + d_c^2 \right\}^{1/2} \quad (3.3)$$

Where d_l , d_λ , d_s and d_c are the FW50 contributions to the probe size of source image, diffraction, spherical aberration and chromatic aberration respectively with the following relations:

$$d_l = d_{geo.} = M d_v = \frac{2}{\pi} \sqrt{\frac{I}{B_r V}} \frac{1}{\alpha} \quad (3.4)$$

$$d_\lambda = 0.54 \frac{\lambda}{\alpha} \quad (3.5)$$

$$d_s = 0.18 C_s \alpha^3 \quad (3.6)$$

$$d_c = 0.6 C_c \frac{\Delta U_{50}}{U} \alpha \quad (3.7)$$

Where M is the total magnification of the system, d_v the virtual source size of the Schottky source, B_r the reduced brightness of the electron source, λ is the wavelength of the electrons, U is the final acceleration energy of electrons, α the half opening angle of the probe, C_s and C_c are the total spherical and chromatic aberration coefficients respectively, and ΔU_{50} is the FW50 value of the energy spread of the electron source (Note: for a ΔU_{FWHM} , the pre-factor of 0.6 in eq. (1.6) should be replaced with 0.34). As soon as the total magnification of the system is fixed, an optimum half opening angle is found for maximizing the current in the probe. Practically this half opening angle can be set by the variable aperture size.

The probe current is calculated using the following formula:

$$I = B_r U \pi^2 \alpha^2 \frac{d_{geo}^2}{4} \quad (3.8)$$

3.1.7 Optics simulations of axial performance (results)

Figure 3.1.4 shows a more detailed schematic overview of the MBSEM imaging sequence. Sections A to F show the procedure of imaging of the array of Schottky virtual sources and sections G to I show the imaging of the common crossovers.

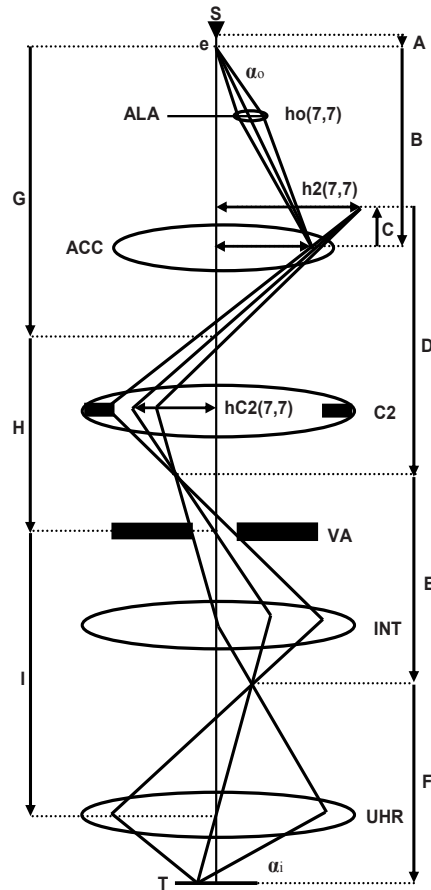


Figure 3.1.4 Schematic overview of the imaging sequence in the MBSEM for an outermost off-axial beam. (A-F) indicates the imaging sequence of the array of Schottky virtual source and (G-I) indicates the imaging sequence of the common crossover. Note: $h_o(7,7)$ is the distance of the outer aperture lens to the optical axis.

For example section "A" comprises the zero strength lens where "S" is the position of the Schottky virtual source and "e" is the image position of the zero strength lens (which should be the same for a perfect zero strength).

The 14×14 array of source images produced by the micro lens array at its image plane (B) will be imaged by the accelerating lens to plane (C) with a magnification close to unity. In the approximation that the accelerating lens was a thin lens, (B) and (C) would coincide, but for a thick lens, these planes can be apart. The ideal position of the plane with source images is in the object principal plane of the accelerator lens. From plane (C) it will be further imaged and de-magnified by the magnetic lenses of the SEM onto the sample (D-F). It can immediately be seen that the object and image position of the accelerating lens, C_2 and the INT lenses for imaging the common crossovers (G-I) are known. This means that the strength and excitations and consequently the axial properties such as magnification, image position, the spherical aberration coefficients and the chromatic aberration coefficients of these lenses can be calculated. Once the image position of the INT lens is determined, the excitation and consequently the axial properties of the UHR lens (F) can also be calculated for a defined working distance. A typical result of the performance of MBSEM lenses is presented in table 3.1.2. For these calculations V_3 is at 4700V and the acceleration energy is 15 keV, the working distance is 5mm. The reason to assign such a value to V_3 is that, for this specific acceleration energy it presents the worst performance of the system in terms of off-axial aberration control. This is because for this value of V_3 the C_2 lens will see the largest off-axial distance of the beams before the pump aperture starts cutting the outer beams off (see figure 3.1.4). The aim is to find the off-axis aberrations for the worst case.

Table 3.1.2 summarizes the axial properties of different imaging steps obtained by the EOD program. Note that the aberration values are given for the image plane. The smallest achievable axial probe size is 1.2 nm corresponding to an opening angle of 7.8 mrad. From now on all calculations are considered for this opening angle.

Table 3.1.2 Axial properties of different imaging steps obtained by the EOD program (for HV= 15KV, V₃=4.7KV). Note: The aberration coefficients (C_s and C_c) are the image side axial aberration coefficients of each lens and for final probe calculation they have to be scaled down with the magnification of lenses.

Imaging Step	Parameter			
	Magnification	Angular magnification	C _s (mm)	C _c (mm)
Source array				
A	1.76	1.04	27	0.52
(A+B) ^a	3.16	0.58	6.9 × 10 ⁴	36
C	1.19	0.26	2.3 × 10 ³	1.2 × 10 ²
D	0.21	4.9	2.2 × 10 ²	2.9 × 10 ¹
E	0.67	1.5	8.6 × 10 ³	1.4 × 10 ²
F	0.03	32.5	5.45	3
Crossover				
G	1.43	-	2.1 × 10 ⁴	-
H	2.81	-	2.5 × 10 ⁴	-
I	2.96	-	2.6 × 10 ⁵	-

^a Imaging parameters of the MBS

Figure 3.1.5 shows the axial performance of the system where the variation of the axial probe size and axial contributions to the probe as a function of opening angle of the probe is presented.

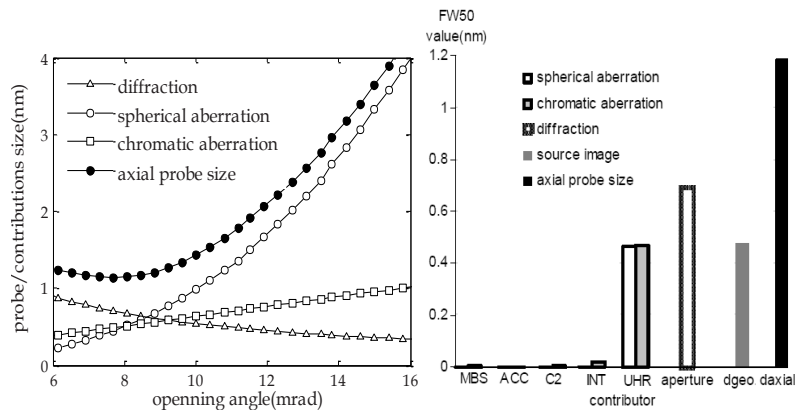


Figure 3.1.5 Variation of total axial probe size and axial contributions to the probe as a function of beam opening angle.

Figure 3.1.6 axial contributions of different lenses to the axial probe for an opening angle of 7.8mrad.

Figure 3.1.6 shows the axial contribution of different lenses to the probe. The contributions are calculated for an opening angle of 7.8 mrad corresponding to the opening angle of the smallest probe of the system.

The axial contribution of the UHR lens is dominant over others, which is not surprising, because its large demagnification also de-magnifies the contributions from other lenses. The axial performance of the MBSEM is very much similar to the performance of a standard single beam SEM. The major contribution to the axial probe size is the diffraction.

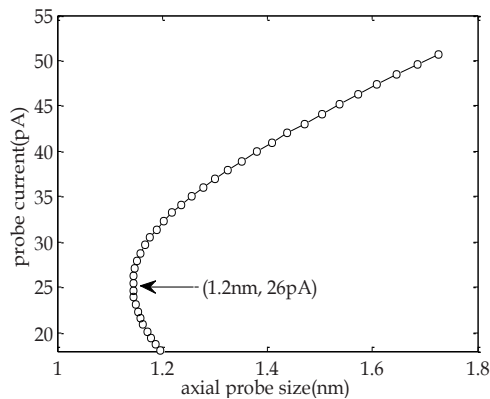


Figure 3.1.7 Relation between probe current and probe size calculated by changing the opening angle.

Figure 3.1.7 shows the relation between probe current and probe size, for a reduced source brightness of $5 \times 10^7 \text{ A/m}^2\text{srV}$. Since the total magnification of the system is fixed, the probe current and probe size can be changed by changing the opening angle of the probe (by changing the size of the variable aperture). As shown in the figure, the current corresponding to the smallest probe is 26 pA. This probe current is also comparable to that of a state of the art high resolution single beam SEM with a Schottky source.

3.1.8 Optics simulations of off-axial performance (method)

In the MBSEM beams are travelling off-axially to the lenses. Therefore, for the probe size quantification of each beam, it is required to include the off-axial aberration contributions to the axial probe size. This is done by calculating the off-axis aberration contributions of each lens (sections A, B, C, D, E, and F) at the sample and adding them to the axial spot size. The off-axis aberrations that are considered here are the third-order geometrical aberration such as

isotropic and anisotropic coma, astigmatism, field curvature and the first order chromatic aberration such as isotropic and anisotropic chromatic magnification error. To calculate these aberrations for a situation as depicted in figure 3.1.8 which is the case in the MBSEM, it is required to have the off-axis aberration coefficients of the lens for a specific aperture position (Z_a). These aberration coefficients can be obtained either in the object or in the image plane of the lens using the EOD program. Moreover, the off-axis distance of the beam in the object (or image) plane as well as the opening angle of the beam is required. The FW50 disks are calculated using the following formulas:

$$\frac{d_{AS}(i,j)}{M} = \sqrt{2}h^2(i,j)\alpha\sqrt{C_a^2 + c_a^2} \quad (3.9)$$

$$\frac{d_{FC}(i,j)}{M} = \sqrt{2}h^2(i,j)\alpha|D_a + C_a| \quad (3.10)$$

$$\frac{d_{CO}(i,j)}{M} = h(i,j)\alpha^2\sqrt{F_a^2 + f_a^2} \quad (3.11)$$

$$\frac{d_{CM}(i,j)}{M} = h(i,j)\frac{\Delta U_{50}}{U}\sqrt{C_{Da}^2 + C_{\theta a}^2} \quad (3.12)$$

Where $d_{AS}(i,j)$, $d_{FC}(i,j)$, $d_{CO}(i,j)$ and $d_{CM}(i,j)$ are FW50 disk diameter of the astigmatism, field curvature, coma, and chromatic magnification error of each lens in its image plane for the beam (i,j) in the array.

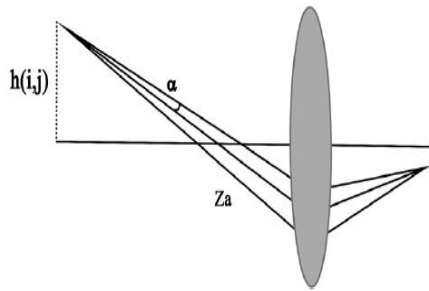


Figure 3.1.8 Schematic drawing of an off-axis beam and parameters needed to calculate the off-axis aberrations.

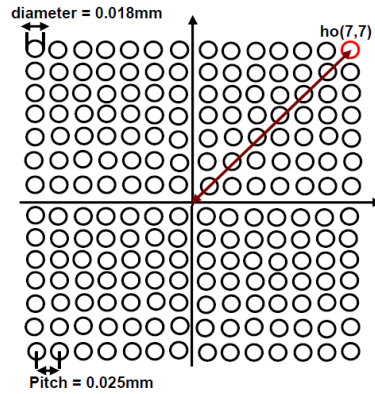


Figure 3.1.9 Schematic drawing of the aperture array with the aperture diameter and pitch definition. The off-axis distance of the beam for subsequent lenses is calculated from this plane.

In these formulas $h(i,j)$ is the off-axis distance and α is the opening angle of that beam in the object plane of each lens (figure 3.1.8). The off-axis distance $h(i,j)$ can be calculated from the known pitch in the plane of the aperture array. Figure 3.1.9 shows a schematic drawing of that plane where for instance the outermost beam ($i,j = 7$) has an off-axis distance to the common optical axis of $h_0(7,7)$. The aberration coefficients C_a, c_a, D_a, F_a, f_a and $C_{Da}, C_{\Theta a}$ are the isotropic-anisotropic third-order geometrical aberration coefficients for astigmatism, field curvature, coma and isotropic-anisotropic first-order chromatic aberration coefficients, respectively, of the lens in its object plane.

These are the aperture-dependent aberration coefficients as indicated by index "a" [16, 17]. Note that the aberration disks for astigmatism, field curvature, coma and chromatic magnification error of the individual lenses, scaled of course by the appropriate magnification.

The numerical pre-factors $\sqrt{2}$ for the astigmatism and field curvature are introduced to convert the full-width 100% value of a uniformly filled disk to a value for the full-width 50% diameter. The shape of the coma disk is not circular, uniformly shaped, so we take as a rough estimate for the FW50 size $1/3$ of the total length of the comet shape. For the chromatic error we have already used the FW50 size of the energy spread, so the total size of the aberration disk will be larger than the value given by the formula above and thus, a different pre-factor than one is not justified. For the MBS and accelerator lens being electrostatic lenses, the anisotropic parts of the aberration coefficients are zero. The FW50 disk sizes of the aberration figures will then be as follows:

$$\frac{d_{AS}(i,j)}{M} = \sqrt{2}C_a h^2(i,j)\alpha \quad (3.13)$$

$$\frac{d_{FC}(i,j)}{M} = \sqrt{2}(C_a + D_a)h^2(i,j)\alpha \quad (3.14)$$

$$\frac{d_{CO}(i,j)}{M} = F_a h(i,j)\alpha^2 \quad (3.15)$$

$$\frac{d_{CM}(i,j)}{M} = C_{Da} h(i,j) \frac{\Delta U_{50}}{U} \quad (3.16)$$

Representing the FW50 disk of Astigmatism, Field curvature, Coma, and Transverse chromatic aberrations respectively.

Since there is no alternative to add individual off-axis aberrations together nor to the axial probe size methodology (like the RPS method that we used for the axial aberrations), we use the algorithm below which is basically a standard quadrature addition of contributions:

$$d_p(i, j) = \sqrt{d_{axial}^2 + d_{off-axial}^2(i, j)} \quad (3.17)$$

$$d_{off-axial}(i, j) = \sqrt{D_{AS}^2(i, j) + D_{FC}^2(i, j) + D_{CO}^2(i, j) + D_{CM}^2(i, j)} \quad (3.18)$$

Where $d_p(i, j)$ is the total probe size of the beam (i,j) in the array with Where $d_{axial}(i, j)$ and $d_{off-axial}(i, j)$ being the axial contribution (axial probe size) and the off- axial contribution to that probe respectively. The off-axial contribution of the beam (i,j) consists of: Where $D_{AS}(i, j)$, $D_{FC}(i, j)$, $D_{CO}(i, j)$ and $D_{CM}(i, j)$ which are the total aberration disk size of astigmatism, field curvature, coma and chromatic magnification error of all lenses at the target respectively.

3.1.9 Optics simulations of off-axial performance (results)

Table 3.1.3 summarizes the calculated electron optical parameters of the system at the wafer. The opening angle is chosen to give the smallest probe possible for this setting.

Figure 3.1.10 shows the off-axial contributions to the outer probe of all subsequent lenses. The off-axial contribution of the last lens of the system is the smallest contribution. This is due to the fact that the common crossover of the beams is in the coma free plane of the lens. Thus, the off-axial contributions of the INT lens are dominant, because the off-axis distance of the beams in the INT plane is determined by the position of the variable aperture and the objective lens, as can be seen in figure 3.1.1b. Nevertheless, we find that the axial contribution of the lenses is greater than the off-axial contribution.

Electron optics of multi beam scanning electron microscope

Table 3.1.3 calculated electron optical properties for $V_3=4.7\text{kV}$ for smallest probe.

Parameter	Value
Total magnification from source to sample	0.016
half opening angle(mrad)	7.8
Size of the variable aperture (μm)	19
Probe current *(pA)	26
Pitch(nm)	360
axial probe size (nm)	1.2
Outer probe size (nm)	1.5
Maximum off-axis height in C_2 lens**(μm)	231
Working distance(mm)	5
Acceleration energy(keV)	15
$V_3(\text{kV})$	4.7

* $B_r = 5 \cdot 10^7 \text{ Am}^{-2}\text{sr}^{-1}\text{V}^{-1}$

**The radius of pumping aperture is $250\mu\text{m}$.

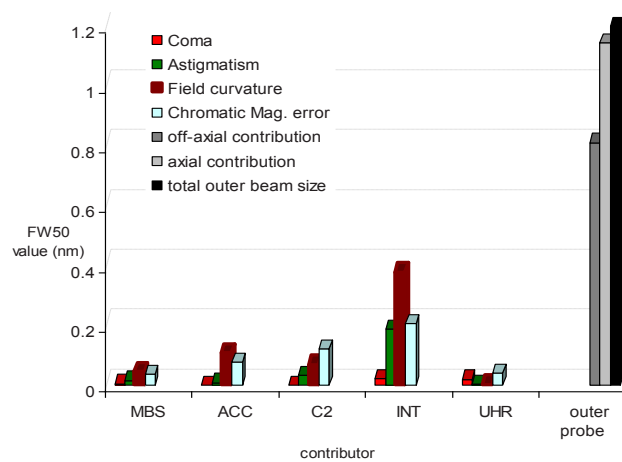


Figure 3.1.10 Off-axial contributions of different lenses to the outer probe. The total probe size, total axial probe size and total off-axial contribution are also shown.

Note that we expect a numerical precision of the values of not better than $\pm 30\%$ due to our rough estimate of the pre-factors in the equations and due to our procedure of addition in quadrature of the different contributions.

In order to check how important it is to get the common cross-over exactly in the coma-free plane of the objective lens we calculated the total off-axis contribution of the UHR lens to the outermost probe as a function of crossover position. Figure 3.1.11 shows the results. The total off-axis contribution consists of contributions of combined isotropic and anisotropic coma, astigmatism, field curvature and chromatic magnification error calculated for an opening angle of 7.8 mrad.

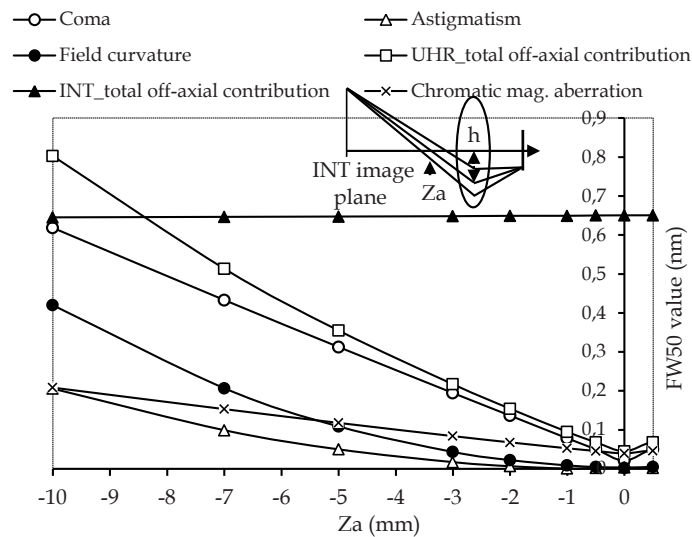


Figure 3.1.11 FW50 aberration discs of Coma, Astigmatism and Field curvature of UHR lens in the outer probe as a function of the position of the crossover along the optical axis. The total off-axis contribution of the UHR and the INT lens to the probe are also plotted in this figure.

The total off-axis contribution of the INT lens to the outermost probe is also shown for comparison. Note that the contributions from the C_2 lens, the accelerator lens and the MBS are smaller than those of the INT lens. For a crossover position further than 8.5mm from the coma-free plane, that is for an off-axis distance in the lens plane (see inset) of $6.5\mu\text{m}$ and more, the off-axis contribution of the UHR dominates over others. Note that the radius of a beam in the objective lens is $28\mu\text{m}$. This stresses the importance of positioning of the crossover fairly exactly at the coma free plane of the UHR lens.

3.1.10 Conclusions

We have demonstrated, by detailed computer simulation of the full optical system, that it is possible to mount a multi-beam source on a standard scanning electron microscope and form multiple focused beams in the sample plane with the same beam size and beam current that was obtainable in the original SEM. The design of a low aberration coupling lens between the multi-beam source and the SEM is critical. For the suppression of off-axial aberrations, the first image plane of the source, with multiple images of the source, should coincide with the plane of the coupling lens. For the calculation of the on- and off-axis aberrations, we have made a model of the full multi beam SEM, so that the contributions from the different lenses can be compared. The result shows that the off-axis aberrations can be kept under control if a common crossover of all the beams is positioned in the coma-free plane of the objective lens. In that situation, the on axis minimum probe size for a 15 kV beam is 1.2nm, the maximum off-axis aberrations in a 14x14 array of beams is 0.8nm, adding up in quadrature to 1.5nm. The main contribution to the off-axis aberrations is field curvature, which, in theory, could be reduced by over-compensating the field curvature in the multi beam source.

3.2 Electron optics of multi beam scanning electron microscope: Part II²

3.2.1 Changing the MBSEM magnification

In a standard SEM, the probe current can be tuned by “spot number”; by changing the spot number in fact the position of the first crossover of the beam is changed leading to a change in total magnification of the system. This results in a different geometrical source size contribution to the total probe which will consequently change the probe current and its size. However, for a specific magnification, fixed spot number, but at the cost of higher contributions from lens aberrations, the probe current can be further

² Paper in preparation.

increased by choosing a larger objective lens beam limiting aperture, also known as the variable aperture (VA). Similarly, in the MBSEM a change in total magnification will change the probe current and its size but also the pitch of the beams. Further change in the probe current but not the pitch is still possible using the VA. In fact, once the magnification of the system is set, using VA one can either set the desired probe current regardless of whatever will be the probe size and/or the smallest possible probe size with a given probe current. Now the question is: How can we change the MBSEM magnification and what are the flexibilities and limitations? It is the subject of this part to answer these questions in more detail. There are basically two ways to change the magnification of the MBSEM. These two ways will be discussed and evaluated separately below in sections "1 and 2".

1). *The total magnification of the system can be changed by changing the accelerator lens strength.* This is very similar to the concept of "spot number" that was discussed in the previous paragraph. From now on we shall call this also a "spot number". In this case the system magnification is changed as a result of a change in the position of the first common crossover of the beam-lets; by changing the strength of the accelerator lens, varying the voltages of the Acc-2 and Acc-3 electrodes (V_2 and V_3), the position of the common crossover (Z_{acc}) will move up and down in the Coulomb tube (see fig 3.1.2). When the crossover goes up (towards the accelerator lens), the C_2 lens has to be weakened to keep the second crossover fixed in the VA plane. This weak C_2 lens will therefore image the array of the beams closer to the INT lens with smaller lens de-magnification. Since for a fixed acceleration energy, the strength of the INT lens is always fixed, this array will be further imaged by the INT lens with a smaller de-magnification. The same applies to the UHR lens because its working distance (WD) is fixed. So, by making the accelerator lens stronger, smaller de-magnification of the total column for imaging the array of beams is obtained. The result is a larger contribution from the geometrical source size, a higher probe current and a larger pitch. The opposite behavior can be obtained by making the accelerator lens weaker.

Note that this is a little counter-intuitive, because in the single beam SEM the spot size decreases when the cross-over is moved upward in the Coulomb tube, while here, the spot size increases.

Table 3.2.1 summarizes the change of the main electron optical parameters of the system as a function of V_3 . In these calculations, the acceleration energy is 20keV and the WD is 5mm. The data presented in this table are for the smallest possible probe, as indicated by the term “min”, for each value of V_3 .

As can be seen, there is an upper and lower limit to the geometrical source size and pitch in this table. The question is: why isn't it possible to vary these parameters over a larger range?

Table 3.2.1: Electron optical parameters of the system as a function of V_3 calculated for $U=20\text{keV}$ and $WD=5\text{mm}$. Note: the data are calculated for an opening angle that corresponds to the smallest probe size.

V_2 (KV)*	V_3 (KV)	$d_{\text{geo.}}$ (nm)	Pitch(nm)	$d_{\text{p-min}}$ (nm)	$I_{\text{p-min}}$ (pA)	$\alpha_{\text{p-min}}$ (mrad)	VA_{min} (μm)
6	7.6	0.536	426	1.05	40	7.5	19.4
6	7.8	0.481	382	1.03	33	7.5	19.3
6	8.0	0.425	340	0.96	26.5	7.7	19.7
6	8.2	0.368	293	0.94	20	7.7	19.7
6	8.4	0.331	263	0.91	16.5	7.7	19.6
6	8.5	0.321	255	0.90	14	7.5	19.2
6	9.0	0.223	175	0.85	7	7.5	19.1

* At an acceleration voltage of 20KV, $V_2=5\text{KV}$ gives the same electron optical performance, but then V_3 has to be adjusted consequently.

The answer is that there are limitations in changing the system magnification by this method. These limitations are listed as follow:

- i) When the crossover moves upwards in the Coulomb tube, the Off-axial aberrations of the lenses especially those of the INT lens limit the probe size; especially of the outer beam-lets ($d_p(7, 7)$). This can be clearly seen from figure 3.2.1 where the off-axial contribution of different lenses, the axial contribution and total probe size is plotted versus V_3 . The conclusion is that the maximum allowed pitch is about 400nm. The minimum pitch is set by the fact that the

geometrical size can be made small to the point that there is still a usable current ($\geq 5\text{pA}$) in the probe.

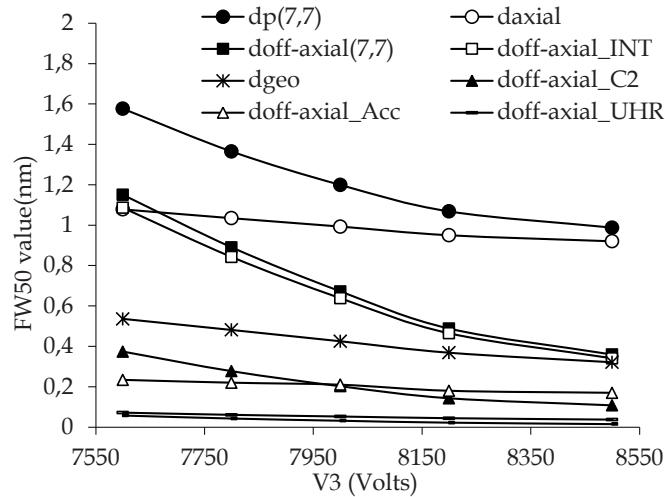


Figure 3.2.1 variation of different aberration contributions to the outer probe as a function of V_3 . The opening angle corresponds to the smallest probe for each V_3 .

- ii) The second reason is that, by moving the crossover upwards, the outer probes get cut off by the pump aperture ($\varnothing = 500\mu\text{m}$) located in the C_2 lens. This limits the number of beams entering the column. Figure 3.2.2 shows the variation of the incidence height of the outer beam at this aperture plane (r_{ap}) as a function of V_3 . It can be seen that the beam blocking occurs for V_3 smaller than 7600V.
- iii) The last limitation which actually comes only when the accelerator lens is very strong is the fact that its object principle plane starts deviating from the image plane of the MBS. This is however negligible for the range of V_3 values shown in figure 3.2.1 and 3.2.2.

The first reason is the most important and limiting reason. Therefore, we assume that the complete range of pitches and geometrical source size change can only be in the range as shown in table 3.2.1. However, as mentioned previously, it is possible to vary the beam current by changing the VA which effectively changes the opening angle of the beams.

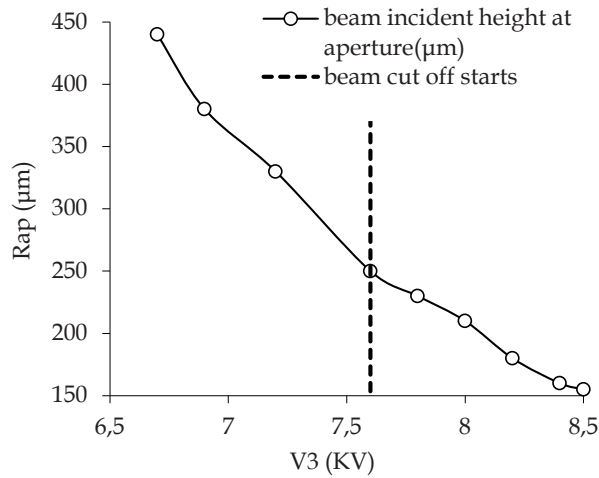


Figure 3.2.2 Incidence height of the outer beam as a function of V_3 . For $r_{ap} > 250\mu\text{m}$, beam blocking occurs.

Figure 3.2.3 shows the variation of the probe current as a function of the axial probe size for different system magnification (different values of V_3). To produce such a graph, the VA is changed which will result in a change in both probe size and its current.

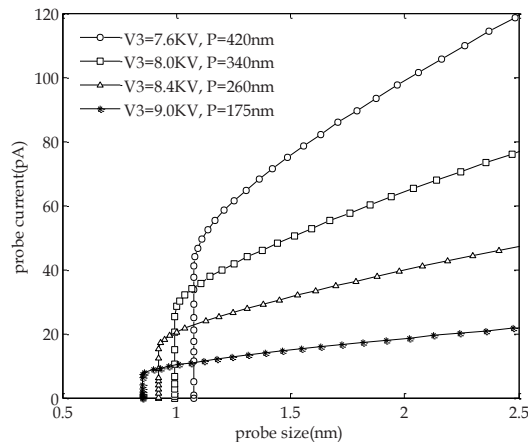


Figure 3.2.3 Probe size vs. probe current for different magnification. "P" stands for pitch and the numbers in the parenthesis correspond to (d_{pmin} (nm), I_{pmin} (pA)) representing the obtainable smallest probe with its current.

2). The magnification of the system can also be changed by changing the working distance (WD) of the objective lens. The working distance of the UHR lens can be changed in a relatively wide range. For larger WDs the UHR lens is weaker,

de-magnifies less, leading to a larger pitch and larger geometrical source size (more current). On the other hand, for smaller WDs, the UHR lens is stronger leading to a smaller pitch and smaller geometrical probe size (less current).

The variation of the magnification of the system through working distance can be combined with “spot number” to have a wide range of variation for pitch and probe current. Table 3.2.2 summarizes the variation of some of the important electron optical parameters of the system for different WD and different V_3 . It is possible to change the system magnification in a sufficiently wide range by a right combination of WD and V_3 . Larger values of V_3 with smaller working distance of the system leads to larger total demagnification whereby very small probe size with a relatively low current and smaller pitch are obtained. Smaller values of V_3 with larger working distances on the other hand give rise to less demagnification of the system whereby a very high probe current with a larger pitch is obtained. In this case however a relatively larger probe size due to a very large contribution of the geometrical probe size but also lens aberrations is expected.

Table 3.2.2: Probe current, probe size and pitch for different WDs and different V_3 . NOTE: the acceleration energy is 20keV and V_2 is fixed to 6KV.

WD (mm)	V3 = 7600V			V3=7800V			V3=8000V		
	dp_{min} (nm)	Ip_{min} (pA)	Pitch (nm)	dp_{min} (nm)	Ip_{min} (pA)	Pitch (nm)	dp_{min} (nm)	Ip_{min} (pA)	Pitch (nm)
1	0.49	13.5	134	0.48	10.6	125	0.47	8.5	107
3	0.76	26	258	0.73	21.5	232	0.71	16	205
5	1.08	42	426	1.035	32.2	382	0.99	26.2	340
7	1.41	53	610	1.42	57.5	547	1.29	35	485
10	1.93	72	900	2.71	125.3	808	1.73	47.5	718

The electron optical parameters listed in table 3.2.2 are only those representing the axial performance of the system. It is important to see the effect of using different working distance and different V_3 values on the off-axial contribution to the probe size. To better understand the effect of different V_3 and different WDs on the off-axial contribution, we define a parameter, dr which shows the relative relation between off-axial to axial contributions in the probe ($dr = (d_p(7,7)/d_{axial}) \times 100\%$). Figure 3.2.4 shows

the variation of dr for the outer probe, $d_p(7,7)$, as a function of WD for different values of V_3 .

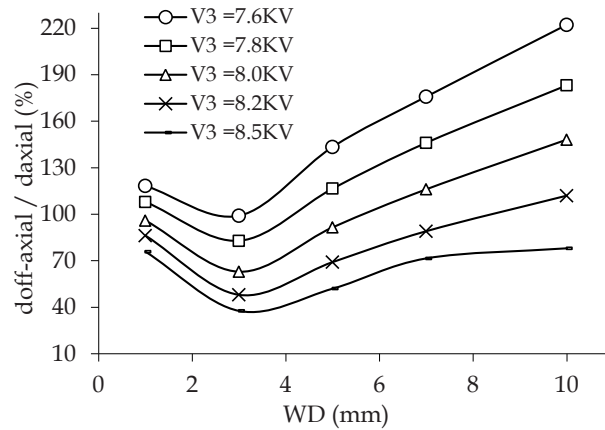


Figure 3.2.4 variation of dr vs. of working distance for different V_3 .

As can be seen, dr increases for WDs ≥ 3 mm and this is most pronounced for smaller V_3 . From the previous section it was found that the increase of the off-axial contributions for smaller V_3 is related to the off-axial aberration of the INT. In figure 3.2.1 it is shown that, for $V_3=7600$ V, the contribution of off-axial aberrations is almost equal to that of axial aberrations. This is also depicted in figure 3.2.4 where at a WD=3mm, dr is close to 100%. We have chosen to keep $dr \leq 100\%$. From figure 3.2.4 it can be seen that, $V_3=7600$ is no longer an acceptable value for larger and smaller WDs than 3mm. It seems that for larger WDs the effect of off-axial aberrations is enlarged. One might misinterpret that, by larger WDs, just like axial contributions, the off-axial aberration contribution of the UHR lens is increased. It is in fact true that the aberration coefficients scale with WD, but because the INT lens aims the beam crossover correctly at the coma free plane of the UHR lens, which is close to its geometrical mid plane, the off-axial aberrations of the UHR lens are still negligible compared to those of the other lenses.

The large values of dr , are for the same reason as explained in the previous section, still a consequence of INT lens off-axial aberrations especially those from field curvature. However, the fact that it is now more remarkable at

larger WDs is because for larger WDs, the UHR lens de-magnifies less and this enlarges the contribution of the INT lens to the probe. On the contrary, the sudden increase of dr for WDs $\leq 3\text{mm}$ is not due to the INT lens off axial aberrations but due to the UHR lens off-axial aberrations. In fact at such a small WDs, the UHR lens de-magnifies so much that the contribution of all preceding lenses, even that of the INT lens is very small. At such a high de-magnification, the UHR lens is so strong that the large contribution from anisotropic coma causes such a jump in dr . Depending on the requirement on pitch, different values of dr can be allowed. This will then define the WD and V_3 values for the best obtainable probe current and/or probe size. To have a relatively uniform probe size distribution, smaller values of dr are preferred and for this a larger values of V_3 has to be chosen in advance and then WD can be varied. Once V_3 and WD are fixed, the probe current can be further changed by varying the VA. Figure 3.2.5, shows some of these typical curves for a fixed V_3 of 8.2 KV and different WDs.

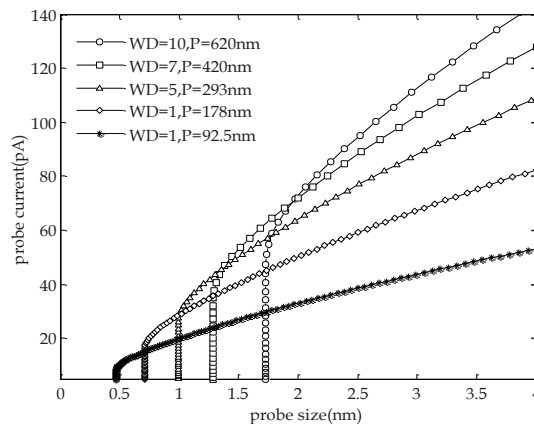


Figure 3.2.5 Relation between probe current and probe size for different system magnification as obtained by changing the WD for a fixed $V_3=8200\text{V}$. (P =pitch)

It should be mentioned that by combining the magnification change as obtained by “spot number” and adjusting the WD and VA, it is also possible (to a very limited extent) to change the pitch while keeping the probe size or its current unchanged.

3.2.2 Different acceleration energies

In a standard single beam SEM, the acceleration energy is defined by the high tension supply unit (HTSU) of the system which effectively biases the complete electron source module negatively with reference to ground. To change the acceleration energy of the MBSEM, the same principle can be used. The important point is that, depending on the acceleration energy, V_2 and V_3 have to be adjusted in such a way that the accelerator lens acts as a field lens directing all the beam-lets towards the column and meanwhile having its object principle plane (H_0) in coincidence with the image plane of the MBS.

Moreover, to change the magnification of the system, V_3 has to be further adjusted. For higher acceleration energies of larger than 10keV, this can be done straightforward; by finding a right value for V_2 and V_3 it is possible to position its H_0 in the MBS image plane and make a crossover in the Coulomb tube and by slight variation of V_3 it is possible to change the system magnification.

At lower acceleration energies of below 10keV on the other hand the accelerator lens cannot comply all these conditions. To overcome this problem, one can use a beam deceleration concept for low acceleration energies, meaning to start with high acceleration energy of e.g. 10-20keV and bias the sample negatively to get the desired low landing energy (LE).

Therefore, we define two acceleration energy regimes of: High and low acceleration energies. In forthcoming sections, the optical performance of the system will be treated in both acceleration energy ranges separately.

3.2.2a High energy performance

As mentioned earlier, at high acceleration energy switching between different energies is very straightforward. It should be noted that all that has been said in the previous section about the system magnification change for specific acceleration energy of 20keV, is also applicable for other high acceleration energies. Figure 3.2.6 shows the variation of the probe current as a function of

probe size for different acceleration energies for a fixed working distance of 5mm and a maximum allowed V_3 defined by INT lens off-axial aberrations.

To produce such a graph, the VA is changed continuously which will result in a change in both probe size and its current.

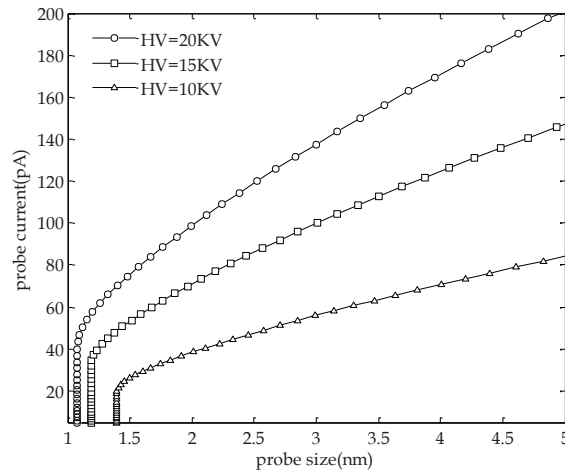


Figure 3.2.6 Probe current vs. probe size for different acceleration energies. It should be mentioned that the smallest allowed value by INT lens off-axial aberrations is used for each acceleration energy and $WD=5$.

3.2.2b Low energy performance

Biasing the sample will introduce an extra electrostatic lens effect, known as “cathode lens”. In combination with UHR magnetic immersion lens, the cathode lens will determine the optical performance of the system at low landing energies (LEs). Table 3.2.3 summarizes some of the main electron optical properties of the system for different LEs of 1, 2.5 and 5 keV. To get these landing energies, the sample has to be biased negatively with respect to the primary acceleration energy of 10keV. These calculations are done for V_3 of 4100V, the smallest allowed value for a V_3 at 10keV, giving the largest possible pitch and geometrical probe size at a fixed WD of 5mm.

Table 3.2.3: Variation of the main electron optical parameters of the MBSEM for different LEs.

Parameter	LE = 5 (keV)	LE = 2.5 (keV)	LE = 1 (keV)
<u>Main optical parameters:</u>			
dp(7,7) (nm)	2.5	2.8	3.4
d _{axial-min} (nm)	1.75	2.2	2.8
I _{axial-min} (pA)	18	14	10
α_{min} (mrad)	9.1	10.4	12.6
VA _{min} (μ m)	19.2	17	15
Pitch (nm)	490	540	600
WD (mm)	5	5	5
<u>Contributions to the probe (nm):</u>			
Geometrical	0.60	0.66	0.74
spherical aberration	0.41	0.36	0.27
chromatic aberration	1.03	1.36	1.86
diffraction	1.03	1.27	1.68
d _{off-axial} *	1.80	1.80	1.91

* Dominant contributions are curvature of field and isotropic chromatic magnification error of the INT lens.

As can be seen from the table, for lower landing energies the probe size becomes larger with a less current. The larger axial probe size is due to the larger contribution of diffraction and chromatic aberration. Although the geometrical contribution is also larger at lower energies, the probe current is smaller due to the fact that at smaller landing energies the opening angle is limited. The relatively larger opening angle of the probe at smaller LEs compared with those of high acceleration energies is due to the low axial aberration coefficients of the combination of a magnetic immersion lens and a very strong cathode lens. In fact, the advantage of having a strong cathode lens is that larger opening angles can be used, which relaxes the problem of a larger diffraction contribution at smaller LEs. The current in the probe can be further adjusted by adjusting the size of the VA.

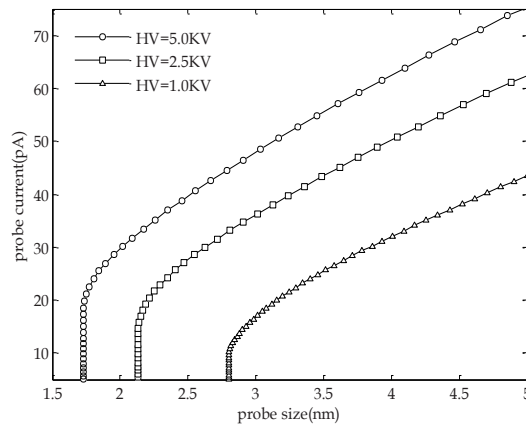


Figure 3.2.7 Probe current vs. probe size for different low landing

Figure 3.2.7 shows the variation of probe current as a function of axial probe size for three different low landing energies. These calculations are done for V_3 of 4100V and a fixed WD of 5mm for primary acceleration energy of 10keV. Now the question is: what are the flexibilities and limitations in changing the MBSEM magnification at lower LEs? The smaller probe current of lower LEs as tabulated in table 3.2.3 indicates that any further demagnification of the geometrical contribution will result in a probe with hardly any current in. This becomes a severe problem for extremely low landing energies of below 2.5 keV. In fact, the reason that in all previous calculations we chose the smallest allowed value of V_3 at 10keV accelerating energy, 4100V, is to have the largest possible contribution from the geometrical source in the probe in order to have enough current in the probe.

The conclusion is that at lower LEs, the presented data in the table 3.2.3 is the lower limit for pitch and geometrical probe size. That means that the variation of magnification by "spot number" in combination with WDs smaller than 3mm leads to an unacceptably low current in the probe. The WDs ≥ 3 mm can still be combined with "spot number" to change the magnification of the system. By doing this of course one has to consider the effect of off-axial aberrations. Figure 3.2.8 shows the variation of dr , as calculated for the outer beam, as a function of WD for different low landing energies (LEs). These calculations are also done for V_3 of 4100V and for an

opening angle that corresponds to the smallest probe size obtained at different WD.

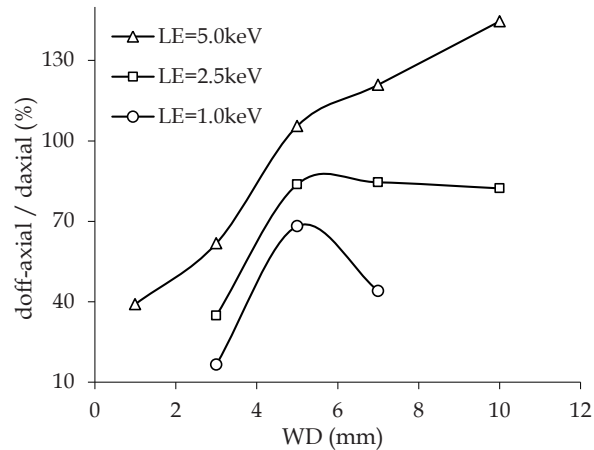


Figure 3.2.8 Variation of the dr as a function of WD for different low

As can be seen from the figure, at LEs of below 2.5keV, the $d_{off-axial}$ is smaller than d_{axial} . On the other hand, for higher LEs of above 2.5keV the probe is dominated by off-axial aberrations at larger WDs. This is because of the larger off-axial aberration contribution from the INT lens but also due to the smaller demagnification of the UHR lens. For example at LE=5keV, it is not allowed to have a WD of larger than 5mm. However, as can be seen from table 3.2.3, the probe current at such a relatively high LE, is still high enough to choose a larger V_3 with lower off-axial contributions from INT lens. What is important to notice in this figure is that, for smaller LEs of below 5keV, there is a WDs for which beyond that value the contribution from off-axial aberration become smaller and smaller. This is in contrast to what we see for relatively high LE of 5keV or even to what we have seen for higher acceleration energies of the order of 10keV as presented in figure 3.2.4.

The origin of this behaviour has to be related to the presence of the cathode lens. In fact, for LEs of below 5keV, the axial aberration coefficients of combined UHR and cathode lens have a minimum for a WD of about 5mm. The lower aberration coefficient of WD=5mm leads to a larger allowed opening angle. With a larger opening angle the axial contribution to the probe

grows faster than the off-axial contribution. The larger opening angle also means that the contribution from diffraction is smaller but the probe current is larger. This is demonstrated in figure 3.2.9 where the probe current is plotted versus probe size for different WDs for LE=2.5keV. It is clear from this figure that the WD=5mm gives the best optical performance compared to that of the others.

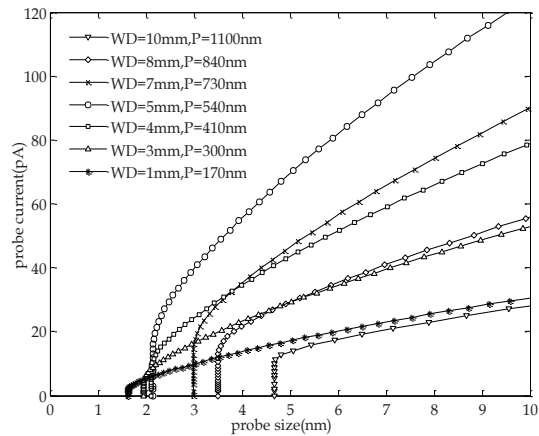


Figure 3.2.9 Relation between probe current and probe size for different system magnification as obtained by changing the working distance of the system.

As mentioned earlier, lower landing energies ($\leq 10\text{keV}$) is only possible by beam deceleration close to the sample by biasing the sample stage. This is very advantageous for the MBSEM at least in three aspects: first, it introduces a cathode lens that in combination with immersion magnetic lens provides a very low aberration objective lens effect making it possible to allow larger beam opening angles. Therefore, first the effect of diffraction can be compensated (to some extent) at lower energies; second, biasing the sample is critical for through the lens detection of the SEs and BSE signals and third the effect of the Coulomb interaction is reduced (section 3.4).

3.2.3 C₂ lens off mode

As it was discussed earlier, the main limitations in changing the MBSEM magnification by changing its working distance and the acceleration lens strength were the off-axial aberrations of the INT lens. It was shown that, in order to minimize the effect of the INT lens off-axial aberrations, larger values of V_3 (weaker accelerator lens) and smaller WDs had to be used. This posed a limitation in having larger pitches of more than 650 nm at higher acceleration energies. By switching the C₂ lens off this can be facilitated to, some extent: In the C₂ lens off mode which is schematically sketched in figure 3.2.10, the C₂ lens is optically switched off. The accelerator lens makes a common crossover of the beams far away in the VA plane. Here we present the results of the C₂ lens off mode. These calculations are done for an acceleration energy of 15keV and different working distances.

The experimental results of this mode for the same acceleration energy and a fixed WD=5mm is the subject of chapter 5 of this thesis but it is also already presented elsewhere [13]. Figure 3.2.11 shows the variation of probe current as a function of probe size for different WDs. The pitch corresponding to each working distance is also presented showing that, using the C₂ lens off mode one can have larger pitches at higher acceleration energies, which was impossible previously. It should be mentioned that in setting the C₂ lens off mode, one has to find a right combination of V_2 and V_3 satisfying the

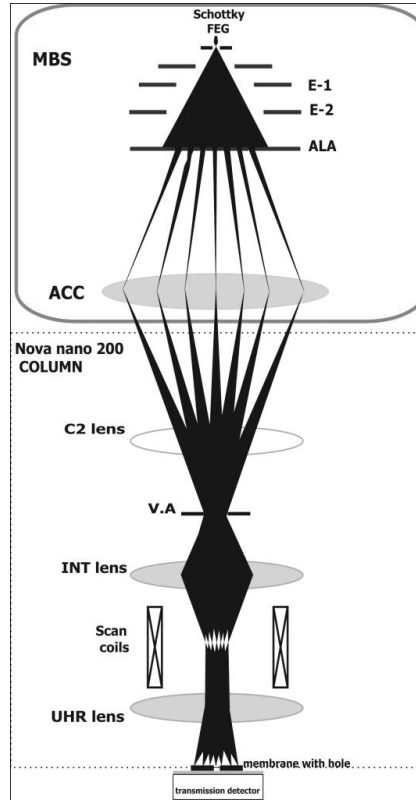


Figure 3.2.10 Schematic overview of the electron optical configuration of the MBSEM in C₂ lens off mode.

following requirements: to keep the object principal plane of the accelerator lens in coincidence with the MBS image plane and to focus the common crossover of the beams in the VA plane such that the incidence height of the outer beams in the pump aperture located just above the C_2 lens doesn't exceed $250\mu\text{m}$.

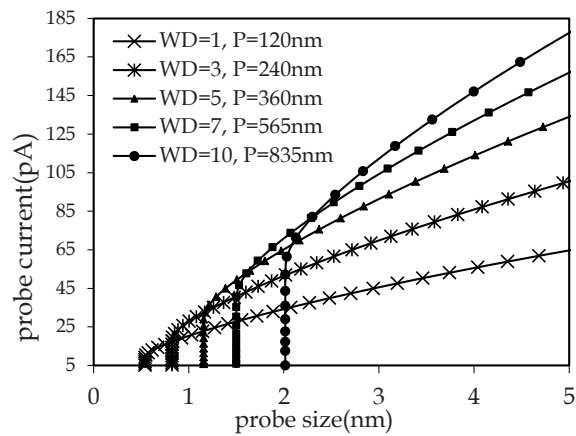


Figure 3.2.11 Relation between probe current and probe size for different magnification in C_2 lens off mode.

Figure 3.2.12 shows the variation of dr as a function of WD at C_2 lens off mode for acceleration energy of 15keV .

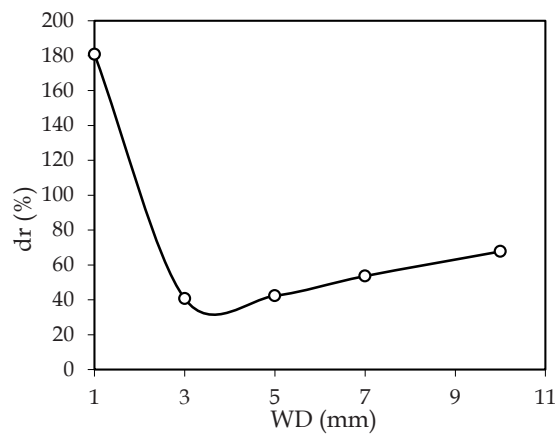


Figure 3.2.12 Variation of the dr as a function of WD for C_2 lens off mode.

Although at larger WD s we have larger pitches compared to what we have seen before, however, for these WD s, dr is smaller than 100% meaning that

the contribution of off-axial aberrations to the probe is smaller than the axial contribution. This is because in the C_2 lens off mode, the INT lens becomes a somewhat stronger lens with a better optical performance. So, larger pitch accompanied with a slightly better resolution is possible in this mode.

3.3 Electron optics of multi beam scanning electron microscope: Part III

3.3.1 MBSEM with larger pitch and higher probe current

All the calculations presented in Part II, about different magnification, different probe current and different pitch, were done for a very high resolution (small probe sizes) MBSEM. This means that special attention was given to probe sizes smaller than 5nm and this will of course limit the magnification range of the system. For some applications in both microscopy and patterning, however, very high resolution is of less importance. Instead a larger current per beam and a larger pitch is of prime importance. In this part the possibilities and limitations of having larger pitch and larger probe current in the MBSEM with moderate probe sizes of 5-20nm or even larger will be discussed. For a larger pitch and a larger probe current, the total demagnification starting from the MBS image plane to the sample plane has to be decreased substantially. From the previous part we know that the magnification of the system can be changed either by changing the strength of the accelerator lens or by changing the working distance of the system. We also know that for very small probes, the former method doesn't offer a sufficiently large range due to the limitation imposed by the off-axial aberrations of the INT lens.

For a larger pitch and a larger probe current the resolution is of less importance: this means that the off-axial aberrations of the INT lens will not be limiting for the magnification ranges it was for the very small probes. However in this case it is the beam cut off by the pump aperture and the deviation of the object principle plane of the accelerator lens from the MBS

image plane (limitations number 2 and 3 in part II) that limit the maximum obtainable magnification. Therefore the only way of increasing the magnification of the MBSEM over a larger range is to increase the working distance which effectively decreases the de-magnification of the objective lens.

Moreover, in the previous part it was also concluded that in general the C_2 lens off mode offers a larger magnification compare to the ordinary C_2 on mode. In conclusion, to have a larger pitch and larger probe current, one has to work with C_2 lens off mode and a larger working distance.

Now the central question is: what are the possibilities and limitations in the larger magnification of the system? To answer this question, let us first define what we mean with a larger pitch and find out what the total magnification is that is needed to achieve it? With a larger pitch we simply mean a pitch of several micro-meters, say 1-5 μm or maybe a little more! To get a pitch of 5 μm the total de-magnification of the MBSEM from the MBS image plane to the sample has to be about 0.07 (= pitch at MBS image plane / pitch at sample). In the case of C_2 lens off, the typical de-magnification of the INT lens is about 0.2. Therefore the de-magnification of the objective lens has to be around 0.35 which is almost one order of magnitude larger than needed in the previous part for a very small probe, very high resolution, MBSEM. If we use the ultra high resolution (UHR) lens as an objective lens, with a typical object distance of 140 mm, this means that the image distance (\approx working distance) has to be about 50mm whereas if we use high resolution (HR) lens as an objective lens whose object distance is about 40mm shorter than that of UHR lens, its image distance has to be about 37mm. But the HR lens body is much larger than 37mm; a MBSEM with a HR lens can only provide very large de-magnifications of much larger than 0.35. But now let us answer the aforementioned question about possibilities and limitations on changing the magnification. There are two main sources of limitations: the immediate danger of a very large magnification of the objective lens is that the off-axial aberrations of the INT lens, which is the largest contribution among the lenses of the MBSEM (and that used to be suppressed substantially by a very large

de-magnification of the UHR lens in the case of high resolution) becomes more and more apparent. This causes a huge difference between the sizes of axial and off-axial probes. Regardless of the type of the objective lens to be used, in general, this imposes an upper limit to the maximum obtainable de-magnification of the MBSEM. As we know, this wasn't the case for a high resolution MBSEM due to a larger de-magnification of the UHR lens which almost nullifies the contribution of preceding lenses in the column. The main off-axial contributions of the INT lens are curvature of field and astigmatism. To a certain extent, the curvature of field can be corrected by the MBS which relaxes the limitation on the magnification range. But then the contribution from astigmatism and other off-axial aberrations of the INT lens come into play. To better understand the effect of the INT lens off-axial aberration contributions on the enlargement of the outer probes, we use the parameter dr that was defined in the previous part as the size of the outer probe to the axial probe ($dr = d_p(7,7)/d_{axial}$). If dr is smaller than 1.4 that is, the outer probe is only 40% larger than the axial probe, the de-magnification of the objective lens is allowed (safe de-magnification) otherwise the de-magnification is not allowed. Figure 3.3.1 shows the variation of dr as a function of the HR and UHR de-magnifications. It can be seen that the UHR lens can provide an acceptable dr for a relatively large range of de-magnifications (below 0.3) only after that the curvature of field is corrected by the MBS. The HR lens can only provide de-magnifications larger than 0.38, a range far beyond the safe de-magnification range where, even if the curvature of field is corrected, dr is still unacceptable. As illustrated in the figure, in the case of both UHR and HR lenses if we use only 5×5 number of beams per quarter (100 beams in total), with extra curvature of field correction by the MBS, the de-magnification ranges up to 0.4 provide an acceptable dr . This can be generalized as: Regardless of the type of the objective lens, the maximum allowed de-magnification of the Objective lens can only be up to 0.3× and beyond that dr is not acceptable.

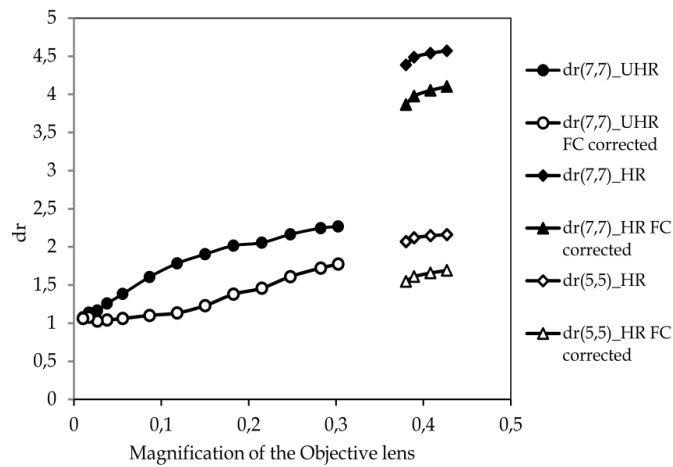


Figure 3.3.1 Variation of the dr as a function of magnification for two Objective lenses of UHR and HR.

The second source of limitation is the large spherical aberration coefficient of the objective lens for larger magnifications. This is because the larger magnifications are achieved for larger working distances and spherical aberration coefficient scales with working distance. The large spherical aberration coefficient limits the opening angle of the probe giving rise to a very small amount of current in the probe. Figure 3.3.2 shows the variation of probe current as a function of probe size for different magnifications of the UHR lens. To produce such a graph, the opening angle of the probe is changed (in real life this is done by changing the diameter of the variable aperture) which results in a change in both probe size and its current. From this figure three different magnification regimes can be distinguished; magnifications up to 0.1: in this regime the probe is mainly limited by the reduced brightness of the electron source, the probe current is rapidly increasing with magnification; magnification range of 0.1-0.2: for this regime the increase in the probe current is considerably slow with magnification and that is because the contribution of axial aberrations gradually start limiting the opening angle of the probe; magnifications larger than 0.2: in this regime the probe current drops down rapidly with magnification and that is because the probe is mainly limited by axial aberrations, especially that of spherical

aberration of the UHR lens. At this range of magnifications, the working distance is so large (typically larger than 30mm) that the spherical aberration coefficient of the lens is in the order of meters. Such a large spherical aberration coefficient limits the opening angle of the beam considerably leading to a very limited probe current for high acceleration energy beams ($\geq 10\text{keV}$). But for lower acceleration energy beams ($\leq 5\text{keV}$) the combination of the UHR (or HR) lens with a strong cathode lens provides a reasonably small spherical aberration coefficient.

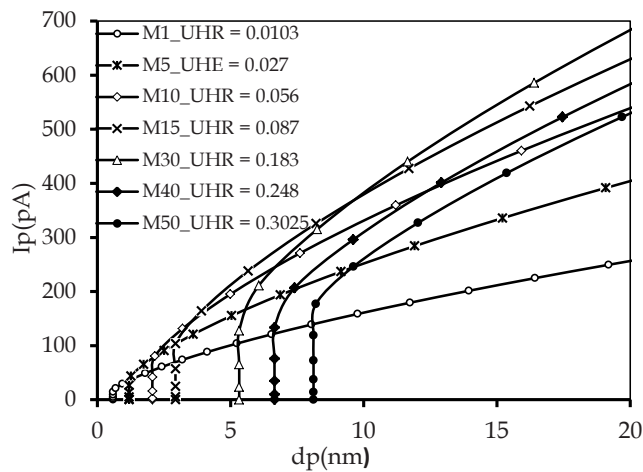


Figure 3.3.2 Relation between probe size and probe current as calculated by changing the opening angle of the probe for different magnifications of the UHR lens. Note: the integer number beside M stands for working distance and the number in the right side is the magnifications of the UHR lens correspond to that WD

The alternative solution is to use the combination of HR and UHR lens as an objective lens instead of using either UHR or HR lens alone. For the same working distances, the combined HR/UHR lens provides larger magnifications with a reasonably smaller spherical aberration coefficients compared to those of HR and UHR lenses. In fact, unlike the case of using UHR or HR lenses separately as an objective lens whose spherical aberration coefficient and magnification scales with working distance, in the case of the combined HR/UHR lens the spherical aberration coefficient and

magnification scales inversely with the working distance. Why this is exactly will be explained later.

Figure 3.3.3 shows the variation of the spherical aberration coefficient and the magnification of the three different objective lenses (HR, UHR and HR/UHR) as a function of working distance.

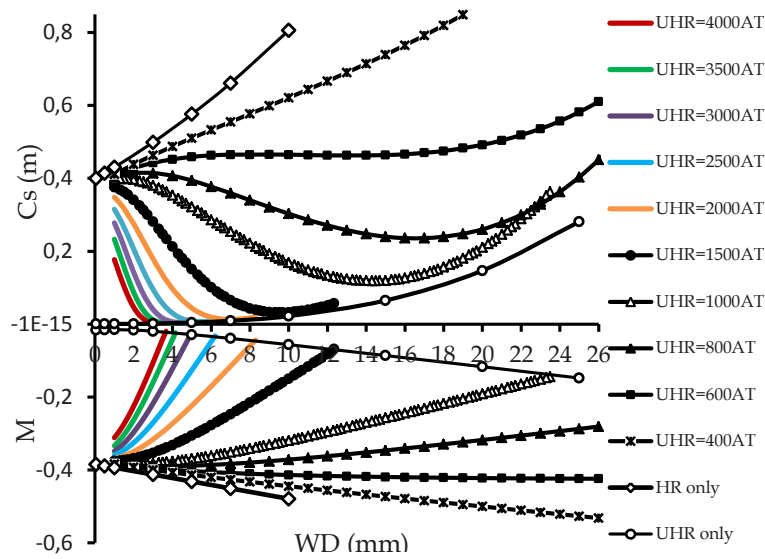


Figure 3.3.3 Variation of Cs & M as a function of WD for three different Objective lenses.

Now the question is: what has to be the excitation of the UHR and HR lenses? This question arises because even a single magnification can be produced with a couple of different combinations of lens excitations and different working distances. As can be seen from the figure 3.3.3, the stronger the UHR lens is, the smaller is the spherical aberration coefficient of the lens but the magnification range is then limited. On the other hand, the weaker the UHR lens is the larger the magnification can be but with a larger spherical aberration coefficient. Moreover, it is also important to notice that, for combined HR/UHR objective lens, the coma free plane lies between the two lenses. The consequence is that the last common crossover of the beams will not be at the UHR lens centre. For a stronger UHR lens (=weaker HR lens) it is

closer to the UHR lens and for a stronger HR lens (=weaker UHR lens) it is closer to the HR lens. The deviation of the last common crossover of the beams away from the object principle plane of the UHR lens simply means that different beams will have different incident height at the lens, leading to a distorted pattern at the sample plane. By tuning the excitation of the HR lens, the distortion can be corrected by its spherical aberration. The compromise in choosing the combination excitation of the HR and UHR lenses for a specific magnification therefore has to be made by taking into account both the total spherical aberration coefficient of the combined lenses and also the spherical aberration coefficient of the HR lens that corrects reasonably the distortion at the sample.

Figure 3.3.4 shows the variation of probe current as a function of probe size for two objective lenses of UHR and HR/UHR for the same magnifications. As before, to produce such a graph, the opening angle of the probe is changed continuously which results in a change in both probe size and its current.

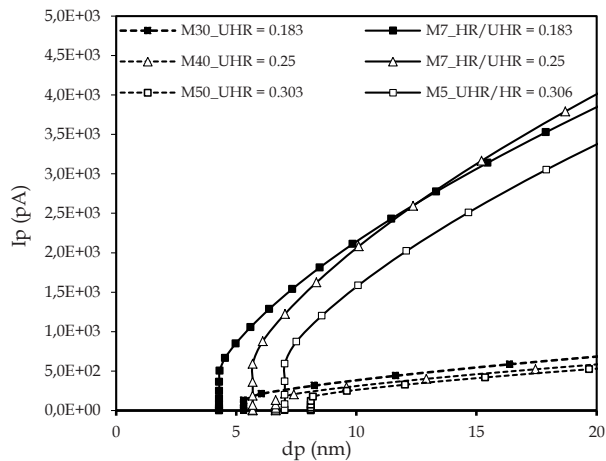


Figure 3.3.4 Relation between probe size and probe current for two objective lenses of UHR and HR/UHR for the same magnifications as calculated by changing the opening angle of the probe.

At any magnification, for the same probe size, a much higher probe current is obtained using HR/UHR as an objective lens. This is due to the lower spherical aberration coefficient of this lens compared with that of the UHR

lens alone for the same magnification. To understand why the combined HR/UHR lens gives a smaller spherical aberration coefficient for a larger working distance, let's look at the behaviour of two principle rays.

Figure 3.3.5 shows the position of the geometrical centre of the HR and UHR lenses (indicated as g-HR and g-UHR) and two principle rays, r_a and r_b , for two different objective lenses, the UHR lens and the HR/UHR lenses for the same object and the same magnification. The point of intersection of r_a with the optics axis shows the Gaussian image point of the lenses and the size of r_b at this point is the magnification of the lenses.

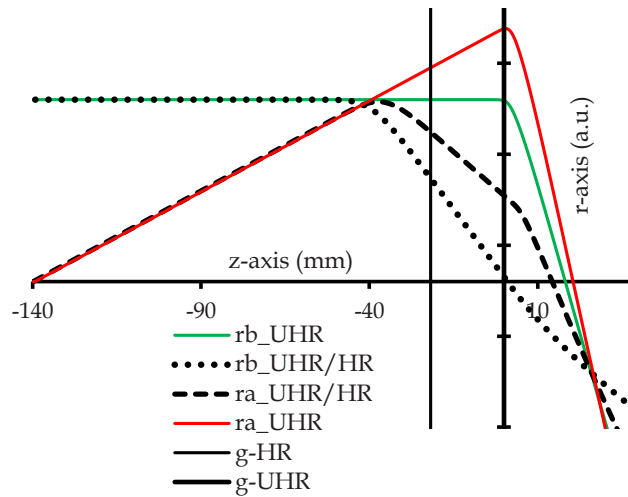


Figure 3.3.5 the behavior of two principle rays of r_a and r_b for different objective lenses of UHR and HR/UHR lenses.

In the HR/UHR lens, the UHR excitation is pre-fixed at 1500AT and HR lens excitation is used to get the right focus at the right working distance but also to minimize the distortion at the sample. From the relation for the spherical aberration coefficient one can see that there is a dependence on the fourth power of the r_a (r_a^4). In the lens field region, the value of $r_{a_UHR/HR}$ is considerably smaller than that of r_{a_UHR} and this is the main reason that the spherical aberration coefficient of the HR/UHR lens is smaller.

3.4 Coulomb interaction

As it is mentioned in the previous chapter, we have used Tiemeijer's program to calculate the Coulomb interactions in the MBSEM. The result of this calculation for the MBS is presented in the previous chapter. The result of this calculation for the rest of the column, from the MBS image plane to the VA plane, is presented here. The result of the calculation is as follows: for an acceleration energy of 10keV, trajectory displacement increases the virtual source size to about 3.5 times its real size making it about 100nm. A significant part of the Coulomb interaction contribution comes from two common crossovers where all the sub-beams meet.

The same calculation however, shows that for the C_2 lens off mode where there is only one common crossover of the sub-beams at the variable aperture plane, the effect of the trajectory displacement is remarkably reduced compared with the previous case, but it is not yet negligible. The effect of the Coulomb interactions can be neglected (below 15% of the virtual source size) only if we operate the system at C_2 lens off mode (only one common crossover of the beams) and for acceleration energies of 15keV or higher. After the variable aperture the effect of Coulomb interactions is completely negligible. For acceleration energies smaller than 15keV, it is therefore important to decelerate electrons at the last moment before they hit the sample, for instance by biasing the sample stage.

3.5 Summary

The chapter consists of the following three parts. Part I presents the general rules and good practices for the design of a multi-beam SEM; the electron-optical behaviour of the system is described, and the electron-optical design of a coupling lens, an accelerator lens, is introduced; also, a recipe for the calculation/simulation of the axial and off-axial performance of the complete system is provided. Main message of this part is that designing a system capable of delivering multiple beams onto the sample, with a typical beam

size and beam current (per beam) comparable to those of a state-of-the-art high resolution SEM, using the column of an standard SEM, is certainly possible. Part II discusses the possibilities, along with the limitations, of changing acceleration energy and magnification of the system, in order to render it suitable for high resolution applications. Conclusion is that the MBSEM can work straightforwardly whenever the acceleration energy is in the range (10, 30) keV; for acceleration energies lower than 5keV, however, beam deceleration at the sample is required. It is also found that the magnification of the system can be varied, in a limited range, by changing the strength of the accelerator lens. Another, more flexible way of varying the system magnification is by changing the working distance; this method, on the other hand, also suffers from limitations. It is shown that it is possible to change the system magnification up to a maximum pitch of $1\mu\text{m}$, by combining the two methods. In part III, the possibilities and the limitations for changing the MBSEM magnification over wider ranges, and for moderate resolutions, are discussed. It is found that, regardless of the type of objective lens used, there is an ultimate limit for the "safe magnification" of the objective lens of about 0.3. It follows that the largest obtainable pitch for the MBSEM is $5\mu\text{m}$. The reasons why the standard HR or UHR objective lenses require a large working distance in order to reach higher magnifications are also explained, together with the reasons why this will degrade the probe current, due to the larger spherical aberration coefficients.

An alternative solution is proposed, based on using the combination of HR and UHR lens as objective. It is shown that this combination allows for larger magnifications while keeping the spherical aberration coefficients reasonably small.

3.6 Bibliography

- [1] B. Roelofs, J. Barth, *Microelectron. Eng.* 2 (1984) 259.
- [2] M. McCord, et al., *J. Vac. Sci. Technol. B* 15(6) (1997) 2125.
- [3] T. Chang, M. Mankos, K. Lee, L. Muray, *Microelectron. Eng.* 57 (2001) 117.

- [4] E. Yin, A.D. Brodie, F.C. Tsai, G.X. Guo, and N.W. Parker, *J. Vac. Sci. Technol. B* 18 (2000) 3126.
- [5] S. Tanimoto, et al., *Jpn. J. Appl. Phys.* 42 (part 1) (2003) 6672.
- [6] S. T. Coyle, et al., *J. Vac. Sci. Technol. B* 22 (2004) 501.
- [7] H. Yasuda, et al., *J. Vac. Sci. Technol. B* 14 (1996) 3813.
- [8] G. Winogard, et al., *J. Vac. Sci. Technol. B* 18 (2000) 3052.
- [9] M. Muraki and S.Gotoh, *J. Vac. Sci. Technol. B* 18 (2000) 3061.
- [10] N. Nakasuji, S. Yoshikawa, T. Satake, and N. Noji, *Jpn. J. Appl. Phys.* 44 (part 1) (2005) 5570.
- [11] O. Kamimura, et al., *J. Vac. Sci. Technol. B* 25 (1) (2007) 140.
- [12] A.J. van den Brom, et al., *J. Vac. Sci. Technol. B* 25 (6) (2007) 2245.
- [13] A. Mohammadi-Gheidari, C.W. Hagen, and P. Kruit, *J. Vac. Sci. Technol. B* 28 (6) (2010) C6G5.
- [14] B. Lencová, J. Zlamal, *Electron Optical Design program package EOD 3.069*.
- [15] J. Barth, P. Kruit, *Optik* 101 (3) (1996) 101.
- [16] B. Lencova, M. Lenc, *Optik* 97 (1994) 121.
- [17] B. Lencova, M. Lenc, *Optik* 105 (1997) 121.

Vacuum, mechanics and electronics of the multi beam source

"Everything should be made as simple as possible, but not simpler."

Albert Einstein

This chapter describes the issues related to vacuum, mechanics: the mechanical design, fabrication, testing, assembly and alignment of the individual electrodes and the electronics of the multi beam source.

4.1 Mechanical design

As explained in chapter 2, one of the major problems of the previous design of the multi beam source was the huge amount of out-gassing of the massive extension unit which was leading to an inadequate vacuum level far worse than a minimum required for the operation of the Schottky source. A very obvious and straightforward solution is to remove the extension part and design a very compact multi beam source which simply fits in the standard column. This design will have, however, consequences on both electron optics and electro-mechanics of the multi beam source proposed and designed by van Bruggen. The changes in the electron optics have already been discussed in chapter 2 and 3. In this chapter the new approach towards the electro-mechanical design of a compact multi beam source module will be discussed. From the electron optical design presented in chapter 2, it can be seen that the multi electron beam source module has six more electrodes compared to the standard single beam module.

Figure 4.1.1 shows a schematic overview of the source section of a standard Nova Nano 200-SEM equipped with: (I) a single beam Schottky electron source module, and (II) a newly designed multi beam source module. From this very schematic picture, some important pre-conditions can be drawn which are important for the design of a compact multi beam source module: As can be seen from the figures, in the multi beam source module, except the Schottky electron source unit with its sub-components (electron emitter, suppressor and extractor) which is a standard product as supplied by FEI Company, the rest of the components have to be newly designed and manufactured.

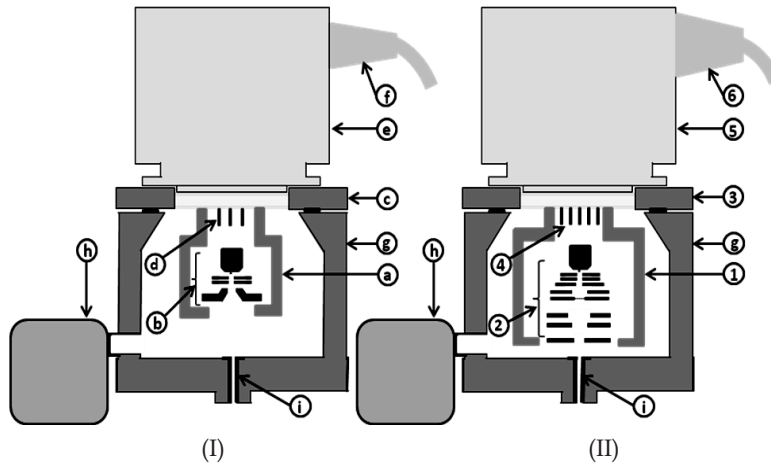


Figure 4.1.1 Schematic cross section of: I) the standard Nova nano 200 single beam source module (a) with its components (b) as from top to bottom: Schottky emitter + suppressor + extractor + C_1 lens all assembled on a CF100 flange (c) with totally 7 high voltage feed-throughs (d) will be connected to a "gun head" (e) which itself is connected to the Field emission Gun Supply Unit (FGSU) via a thick cable (g). The CF100 flange is mounted onto the source house (g) of the standard SEM column and a 25l/s getter ion pump (h) is used to create ultra high vacuum level necessary for the operation of the Schottky source; II) the newly designed multi beam source (1) with its components (2) as from top to bottom: Schottky emitter + suppressor + extractor + E-1+E-2+AA+Acc-1+Acc-2+Acc-3 all assembled on a CF100 flange (3) with totally 11 high voltage feed-throughs (4) will be connected to a "gun head"(5) which itself is connected to two FGSUs via two thick cables (6). The CF100 flange is mounted onto the source house (g) of the standard SEM column and a 25l/s getter ion pump (h) is used to create ultra high vacuum level necessary for the operation of the Schottky source.

A very immediate consequence of removing the extension part of the electro-mechanical design is twofold: the first is the lack of space to accommodate all the extra electrodes in the standard source house and the second is the lack of high voltage feed throughs in the standard CF100 flange as used for the Nova-nano 200 SEM. In fact, the main reason for using an extension part was the possibility of accommodating all extra electrodes in it with all the necessary high voltage feed throughs required to supply the potentials on the extra electrodes of the multi beam source module. Since the plan is to use the standard column of the Nova-nano 200 SEM with all its standard electro-mechanical, vacuum and software controls, to fit the multi beam source module in the standard column, some modifications in the electronics, mechanics, vacuum and software are inevitable. This means that not only more power supplies are needed but also that the standard CF100 flange with its limited number of connectors cannot be used. Therefore to make a compact multi beam source module with a design very similar to its standard single beam counterpart, three important precautions have to be taken into account: high voltage connection problems have to be solved; in a dense and a compact design the high voltage breakdown between the electrodes has to be seriously taken into account; vacuum problems have to be taken into account. The first problem can be simply solved by using a CF100 flange equipped with more high voltage feed-throughs. This will be explained in the section about electronics. The second problem can be solved by making an elaborate mechanical design e.g. by making longer paths on the insulators separating the electrodes. This part will be presented in forthcoming sections on mechanics. The problem associated with vacuum will be briefly treated in the next section.

4.1.1 Vacuum design

Although with the attempt of removing the extension part the out-gassing area is substantially reduced it is yet important to know whether the present IGP is capable of reaching and keeping an ultra high vacuum level of $<5 \times 10^{-9}$

Chapter4.

mbar as required for the operation of the Schottky source. To evaluate this let's make the following simple calculation. The total out-gassing area of the new source module is about 1100cm². With an averaged out-gassing rate of about 5×10^{-10} Torr .l.s⁻¹cm⁻² for the elements (Macor, Titanium and cleaned and polished stainless steel), the total pumping speed required to keep a vacuum level of about $<5 \times 10^{-9}$ mbar is about 100 l/s, which is four times more than the pumping speed of the present IGP. The problem however can be solved by decreasing the out-gassing rate of the components. This can be simply done with a long and high temperature bake-out (e.g. at temperature of about 250°C for one day or more) of the complete source module and preventing the use of higher out-gassing materials, especially Teflon wires and glues. In the worst case scenario, with a bake-out process the out-gassing rate will be reduced by about one order of magnitude and then it immediately follows that the standard IGP can simply reach the vacuum level of 10^{-9} mbar which is good enough for the operation of the Schottky source. Thanks to the bake-out and minimizing the use of high degassing rate material, the vacuum level of the multi beam SEM is always one order of magnitude better than what is actually needed. It should also be mentioned that due to the lack of space it was not possible to accommodate internal bake out elements such as bake out lamps inside source module. Therefore the bake-out has to be performed out of the column, in a separate set up.

4.1.2 Mechanical component design

All electrodes are made of Titanium with accurately drilled holes using Electric Discharge Machining (EDM) method. The degree of accuracy in drilling is determined by the required tolerances as calculated in chapter 2. The insulators are made of Macor. The aperture array is made of a Silicon wafer using MEMS fabrication techniques. Prior to assembling, the accuracy of both the metal and the micro-fabricated electrodes such as the roundness of the holes, quality of their edges and their thickness is examined using an SEM and it turned out to be within the range of the required tolerances.

The performance of the MBS against charging and contamination is studied using a setup shown in figure 4.1.2. In this setup a copy of the MBS module is installed in the tilted stage of the standard SEM chamber and the focused beam of the SEM is used as an electron source of the MBS. By apply voltages on the MBS electrodes an array of focused images is produced using a CCD camera accommodated below the MBS. Typical results of this experiment are shown in figure 4.1.3.

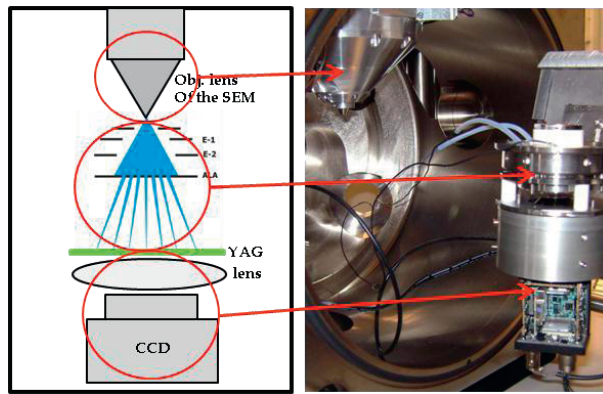


Figure 4.1.2 Experimental set-up for testing the performance of the electrodes in the SEM chamber. Note, the wire connection for the electrodes to the outside chamber is done via side flanges, and insulator pillars for electrical insulation of the MBS from the Chamber. Also note the tilted stage of the SEM.

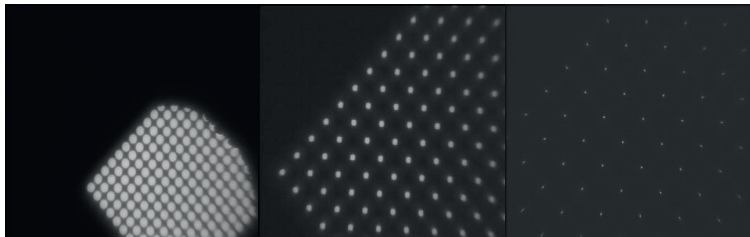


Figure 4.1.3 Typical result showing a focusing action of the MBS by adjusting the voltages on the electrodes. By zooming in on the focused beam it is possible to see whether there is any asymmetrical form of aberrations or disturbances as caused by charging due to the contamination or remaining oxide layer of the Bosch process.

Using these images and by analyzing the shape, roundness and pitch between the focused spots the possible charging issue of the aperture array (AA) and other electrodes are studied. This charging can be caused either by electron beam induced contamination on the electrodes or by a very thin oxide layer on the walls of the small apertures in the aperture array. The thin oxide layer is the leftover of the Fluoride components as used in the Bosch process to etch holes in the Si-wafer. It was found that indeed the left over oxide layer is causing a charging effect which leads to astigmatic spots. This problem however, is circumvented by careful deposition of Molybdenum on both sides of the aperture array.

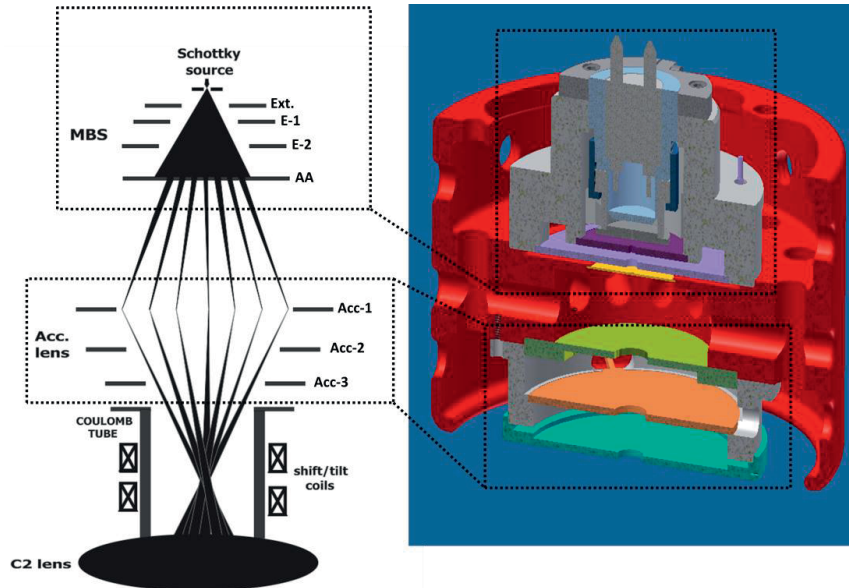


Figure 4.1.4 Schematic electron optical (left) and corresponding mechanical drawing (right) of the multi electron beam source module.

4.1.3 Components assembly and alignment

The multi electron beam source module is composed of two main units namely the multi beam source (MBS) and the accelerator lens (Acc. lens). Figure 4.1.4 shows a schematic electron optical and corresponding mechanical drawing of these two units. As can be seen from the drawing, the complete

module is designed such that every individual unit can be assembled and aligned separately and then the two units are aligned and assembled with respect to a common reference. The common reference of the MBS and Acc. lens is as follows: in terms of flatness of electrodes is the AA and Acc-1 plane mechanically made in the main Bell¹ that holds these two units against each other, and in terms of concentricity of the electrodes is the tip. In the forthcoming sections the alignment and fixation of the components will be explained in more detail. The assembly and alignment of the multi beam source module can be divided into three main steps as follows:

4.1.3a MBS unit

In assembling and aligning the MBS, two following important pre-conditions have to be kept in mind:

- The electrodes: Ext, E-1, E-2 and ALA, should be parallel and concentric with each other, within the range as defined by the tolerances.
- The tip has to be in the center of the hole in the electrodes (in line with the common optical axis of the electrodes within the range of the defined tolerances)

It should be mentioned that the electron source with the extractor, suppressor and emitter provided by FEI Company is used. The concentricity of the tip to the extractor aperture was found to be within the range of tolerances and therefore needed no further alignment. To position the electron source, E-1 and E-2 and to separate them electrically, a very accurately machined Macor insulator with tight tolerances, better than 5 μ m, is used. Figure 4.1.5a and 4.1.5b show drawings of the front and backside of the insulator.

The flatness of plane 1 as indicated in figure 4.1.5a is of prime importance.

¹ The container where the entire components of the multi beam source module is enclosed in. In figure 4.1.4 it shown in red color. Historically the name "Bell" is given to this part by FEI Company, Eindhoven and it is because of its similarity to bicycle bell which is called "Fietsbell" in Dutch. We shall call it as "Bell" throughout this thesis.

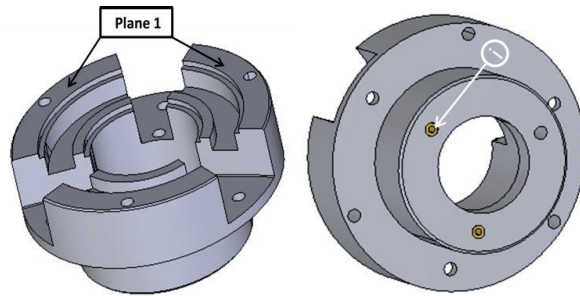


Figure 4.1.5a (left) mechanical drawing of the front and fig. 4.1.5b (right) mechanical drawing of the backside of the Macor insulator. Plane 1 in fig.4.1.5a is a reference plane for aligning Ext., E-1 and E-2.

This is because the flatness of the Ext., E-1 and E-2 will be examined and aligned with respect to this common plane. The degree of flatness of this plane is carefully examined using a 3D coordinate measurement and a height measurement tool present at the section “Demo” workshop of the Delft University of Technology. Figure 4.1.6a and 4.1.6b show pictures of these systems.



Figure 4.1.6a (left) 3D coordinate measurement tool and Figure 4.1.6b (right) height measurement tool.

After this measurement, the standard electron source is slightly fixed in its clamping ring as shown in Figure 4.1.7a (the connection to the suppressor shouldn't be forgotten in this step). This clamping ring has to be fixed to the bottom of the Macor using three insert small screws and three small cylinders (depicted in fig4.1.5b by “(i)”) having inner threads, that were glued to the

Macor piece. The flatness of the extractor electrode and its height is measured with reference to plane 1. With these measurements it is possible to adjust the correct distance between Ext. and E-2 and its parallelism with other electrodes.



Figure 4.1.7a (left) mechanical drawing of the electron source fixed in its clamping ring and Figure 4.1.7b (right) a picture of the electron source mounted to the Macor (the electrical connection to the extractor is also clear from picture).

It should be noted that in this step the electrical connection to the extractor has to be made (figure 4.1.7b). Now E-1 has to be placed in the Macor and its flatness should be measured with reference to plane 1. E-1 itself cannot be moved in its x-y plane but along the z-axis (the optical axis), its height and possible tilt can still be adjusted. The distance between E-1 and extractor electrode is very crucial and has to be accurately measured. With the help of 3D coordinate and height measurement tools this can be done within the tolerances calculated in chapter 2. After all these steps, E-1 is ready to be glued to the Macor. We used ultra high vacuum compatible glue to guarantee that the correct distance between Ext. and E-1 will remain unchanged, while gluing and curing, three small cylindrical spacers having only $5\mu\text{m}$ smaller in height than the required spacing are used between these electrodes. These small cylinders can be simply put in and taken out from the three side openings of the Macor. Needless to say that after each step of gluing a part, the glue has to be cured first and only then another step can be taken. The next step is to fix E-2 to the Macor. Exactly in the same way and following all those steps for E-1, plus the fact that E-2 has to be concentric with E-1, E-2 should be glued to the Macor. To examine the concentricity of the electrodes,

Chapter4.

a roundness measurement tool whose standard probe was replaced with a CCD camera and a lens system connected to a TV screen (figure 4.1.8) is used.



Figure 4.1.8 roundness measurement tool whose standard probe was replaced with a CCD camera and a lens system connected to a TV screen (not shown here) used to examine the concentricity between the optical elements.

Now, the tip has to be concentric with E-1 and E-2. If the tip is not at the centre of the electrodes, the source with its clamping ring can be moved with respect to electrodes. After this step, the source with its clamping ring is fixed and glued to the Macor. Figure 4.1.9 shows a picture of the complete unit of electron source, E-1 and E-2 aligned and glued to the Macor.



Figure 4.1.9 picture of the complete unit of electron source, E-1 and E-2 aligned and glued to the Macor.

4.1.3b accelerator lens unit

In assembling and aligning the Acc. lens, the following important pre-condition has to be kept in mind:

- The electrodes, Acc-2 and Acc-3 should be parallel and concentric with each other within the tolerances needed.

Very similar to the MBS, in order to position the electrodes of the accelerator lens and to separate them electrically, an accurately machined Macor insulator with tight tolerances of better than $5\mu\text{m}$ is used. Figure 4.1.10 shows a mechanical drawing of this Macor insulator.

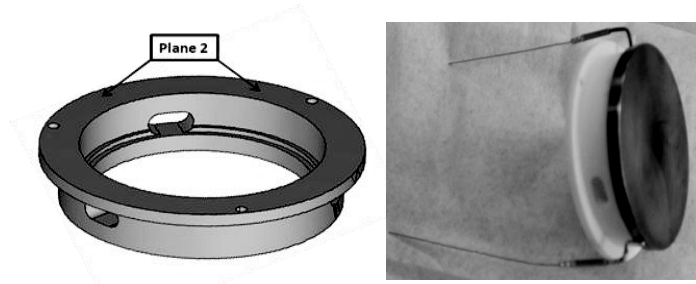


Figure 4.1.10a (left) mechanical drawing of the Macor insulator. Plane 2 is a reference plane for aligning Acc-2 and Acc-3. Figure 4.1.10b (right) picture of the complete unit of Acc-2 and Acc-3 aligned and glued to the Macor.

The flatness of the “plane 2” as indicated in figure 4.1.10a is of prime importance. This is because the Acc-2 and Acc-3 will be aligned with respect to this common plane. The degree of flatness of this plane is carefully examined used a 3D coordinate measurement and a height measurement tools and it turned out to be within the range of the required tolerances. The Acc-2 and Acc-3 are aligned and glued to the Macor following similar alignment steps as used for E-1 and E-2. Figure 4.1.10b shows a picture of the aligned and glued Acc-2 and Acc-3 to the Macor insulator with their electrical connections.

4.1.3c complete multi beam source module

So far the elements of two important units of the multi beam source module are aligned, glued and fixed separately. In this step the MBS and Acc. lens will be aligned and fixed with respect to each other to their common interface, the Bell. However, prior to this, all the necessary preparations such as electrical connections to the electrodes, the 11 pins CF100 flange with its connectors, etc. have to be prepared. Figure 4.1.11 summarizes all the steps needed to be taken before aligning and fixing the MBS and Acc. lens to the

Bell. Only after all these preparations, the MBS and the Acc. lens can be aligned and fixed with respect to their common references in the Bell.

There are two common reference planes, each for every unit, namely AA and Acc-1 which are mechanically fairly tightened and pre-aligned with respect to each other. In figure 4.1.11 indicators 3 and 4 are showing the places of these two crucial planes in the Bell. The Bell itself is made with a very tight accuracy of below $5\mu\text{m}$ to guarantee that these two planes are perfectly parallel. The Bell is made out of NiFe to act as a shield against stray electromagnetic fields and has the same potential as AA and Acc-1. First the complete unit shown as "(1)" in fig. 4.1.11 has to be fixed to the Bell using the screw indicated by letter "g" as shown in figure 4.1.12a. The next step is to examine the flatness of the AA plane with respect to E-2. These two planes have to be perfectly parallel to each other.

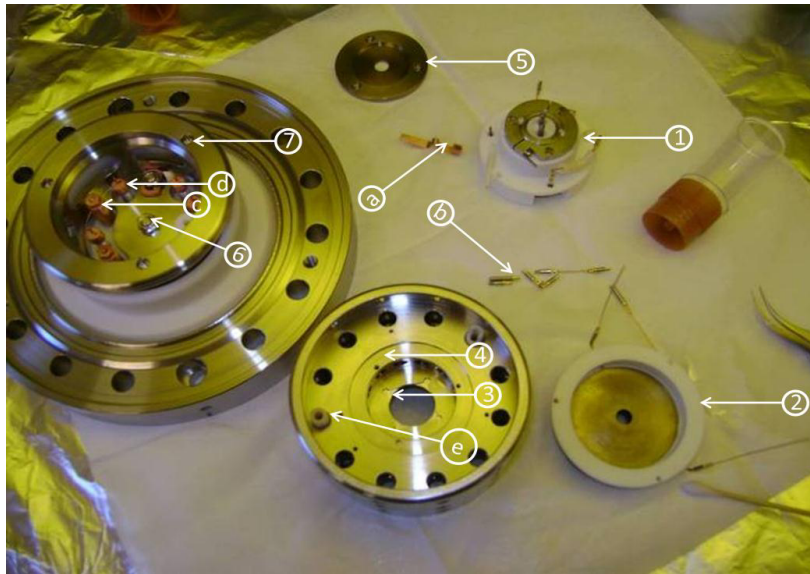


Figure 4.1.11 All the steps needed to be taken before aligning and fixing the MBS and Acc. lens to the Bell. The picture shows the complete MBS unit with its connectors (1), Acc. Lens unit with its connector (2), AA plane (3), Acc-1 plane (4), Acc-1 electrode (6), threaded holes to mount the Bell onto the flange (7), a thick copper connector (a) making connection between the filament in (1) and corresponding pins in flange (c), small pins with tiny clamping mechanism (b) to connect electrical connections between electrodes and flange pins (d), isolated connector passage for Acc-2 and Acc-3 (e).

As the very last step, the Si wafer of which AA is made can be placed and its coordinates and height can be measured and compared with E-2. In case of any tilt, the “plane 1” has to be adjusted to correct the tilt. Just to make sure that the wafer and Acc-1 are located accurately in place, the tilt between Acc-1 and AA electrode has to be examined. In the next step the concentricity of the MBS has to be examined with respect to Acc-1. For this the AA wafer has to be removed because it blocks the view. The concentricity of Acc-1 and the MBS elements can be examined using a turn-table and a CCD camera imaging the edges of electrode holes and the emitter tip. Any possible misalignment can be corrected by shifting the MBS with respect to Acc-1 while keeping them parallel. After this step, the Acc-1 has to be taken off again and the AA wafer has to be fixed in its position. Afterwards, the Acc-1 has to be fixed in position again.

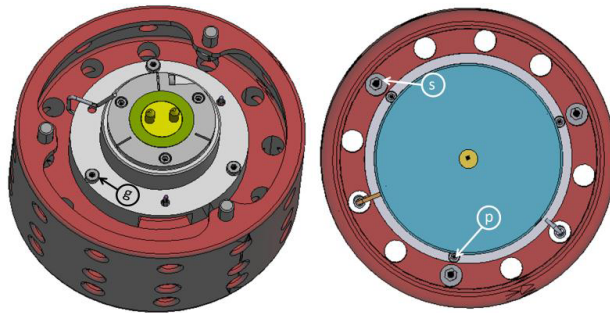


Figure 4.1.12a MBS is fixed to the Bell using the screws as indicated by “g”. Figure 4.1.12b Acc. lens is fixed to the Bell using the screws as indicated by “p”. In this step the electrical connections to the Acc-2 and Acc-3 have to be adjusted and three main screws (S) holding the Bell on top of the flange have to be inserted in place.

Now, the flatness and concentricity of the second unit “(2)” needs to be examined and aligned with respect to Acc-1. Afterwards it can be fixed to the Bell using three screws as indicated by “p” in figure 4.1.12b. The electrical connections to the accelerator lens electrodes have to be brought in place and three main screws holding the Bell on top of the 11 pins CF100 flange have to be inserted through the holes as indicated in figure 4.1.12b by “S”.

Chapter4.

These three screws will fix the Bell to the flange through the threaded holes as indicated by “7” in figure 4.1.11. Now the Bell has to be mounted on the 11 pins CF100 flange. However, before completely tightening the three screws (7), two important steps have to be taken.

- All electrical connections between the elements and their corresponding pins in the flange have to be made. This can be done using tweezers through the openings as indicated in figure 4.1.14. Afterwards, the electrical connections have to be checked using a multi-meter.
- The concentricity and flatness of the entire module with respect to the CF100 flange has to be examined. This can be done by testing the concentricity and flatness of Acc-3 with respect to plane 8 as shown in figure 4.1.13.

Only after these steps, the Bell can be tightened to the flange and it is ready to be baked out.

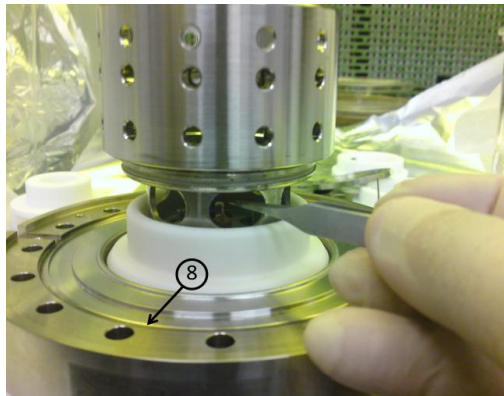


Figure 4.1.13 The electrical connections to the Acc-2 and Acc-3 have to be fixed using the tweezers as shown. Before completely tightening the screws “(s)” the concentricity of the Bell has to be checked w.r.t. rim “8”.

Figure 4.1.14 shows a picture of a “ready to install” multi beam source module mounted on a CF100 flange next to its standard counterpart, the standard source module of the Nova nano 200 single beam SEM. As can be seen it is slightly larger than its standard counterpart.

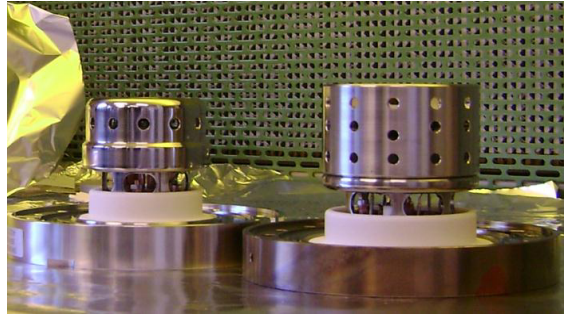


Figure 4.1.14 Multi beam source module versus the standard single beam source module of the Nova nano 200 SEM from FEI Company.

Now the complete module has to be installed in a separate baking set up for higher temperature baking (around 250°C) for a couple of days. To make sure that nothing goes wrong during the wiring and also during the bake out, it is important to first do a flashover or breakdown tests between the elements.

After the bake out process, the complete module has to be examined again for any possible drift or tilt as caused by heating. Now the multi beam source module has to be mounted on the microscope. The standard procedure of getting a good vacuum, as provided by FEI standard software has to be followed carefully except the “lamp bake out” step which has to be skipped. After cooling down the system it should be possible to get a vacuum in the range of 5×10^{-10} mbar. The next step is to mount the 11 pins gun head connector to the back side of the flange and activate the high tension interlock. Now the system is ready to be started.

4.2 Electronics

Figure 4.1.1a shows a schematic overview of the electron source of the standard Nova-nano 200 SEM. The electron source module comprising a Schottky type field emitter, a suppressor, an extractor and the first electrostatic condenser lens (C_1) is mounted on a CF100 flange. The flange equipped with high voltage connectors is in fact the electrical interface between the standard Field emission Gun Supply Unit (FGSU) and electron

optical elements inside the source module. These connectors supply the filament current and the suppressor, extractor and the C₁ lens potentials.

The source module housing in the column is kept at ultra high vacuum level of 10-9mbar by a 25 l/sec getter ion pump (IGP). While operating the system, the complete source module and all FGSU supply units will be on a negative high voltage with respect to a real ground as is chosen by the user. This means that the electrons emerging from the emitter are accelerated between this housing and the Coulomb tube. In a standard SEM, the potential on the Coulomb tube depends on the high voltage setting. For low voltages, its positive potential is higher and for higher voltages it is lower and at -30 kV it is grounded whereas in the MBSEM the Coulomb tube is always at real ground potential. Figure 4.2.1 shows a schematic overview of current and voltage supplies of the standard source module and their connection path to the corresponding component and to the gun head. The standard Field Emission Gun Supply Unit (FGSU1) of the SEM supplying the Schottky electron source is, lifted to a maximum voltage of -30 kV by the High Tension Supply Unit (HTSU).

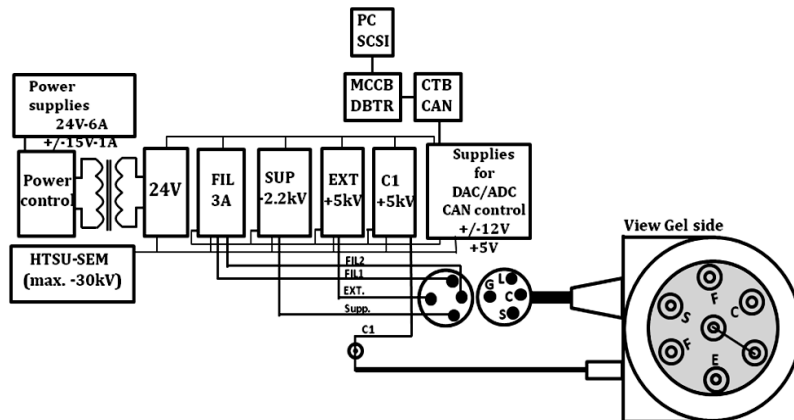


Figure 4.2.1 Schematic overview of current and voltage supplies of the standard source module and their connection path to the corresponding component and to the gun head. The standard Field Emission Gun Supply Unit (FGSU1) of the SEM supplying the Schottky electron source is, lifted to a maximum voltage of -30 kV by the High Tension Supply Unit (HTSU).

In order to supply voltages to all electrodes of the MBSEM, in addition to the standard FGSU of the SEM, another FGSU, FGSU2, is used. The second FGSU, however, is modified as follows: the supply board for the filaments is removed and the supply board of the suppressor is replaced with a new voltage supply unit of maximum 15kV, the supply unit for the extractor is kept unchanged but the supply unit for the C_1 lens is also replaced with another supply unit of maximum 15kV. There is still one electrode left, Acc-2, which needs a separate supply unit. This is unfortunately not possible because of lack of space in the FGSU container. To solve the problem the remaining electrode is connected to one of the other electrodes, either internally or externally. For the very first version of the multi electron beam source module it was connected to electrode-2 (E-2) externally through a high voltage safety box filled with Silicone gel (see figure 4.2.2). For the present multi beam source module this is connected internally to the extractor. In the near future another separate supply has to be integrated to supply the Acc-2 separately. This gives more freedom in the system performance, especially when working with different energies and different magnifications. Unlike the FGSU1, which is floating on a negative potential supplied by the High Tension Supply Unit (HTSU), the FGSU2 is lifted by the C_1 supply unit of FGSU1 (fig4.2.2).

Figure 4.2.2 shows a schematic overview of the power supplies of the multi-electron beam source. The Schottky electron source is supplied by the FGSU1 of the microscope via a standard cable as provided in the gun head. FGSU1 is lifted to a maximum voltage of -30 kV by the HTSU of the SEM. It is controlled by the microscope control PC and a standard program provided by FEI Company. The potentials on the other electrodes of the multi beam source are supplied by FGSU2, whose local ground is lifted to the potential of the Bell using the C_1 supply in FGSU1. At the same time the output of C_1 is connected to the Acc-1 and AA. The output of the FGSU2 supply units are connected to the gun head via a box filled with Si-gel.

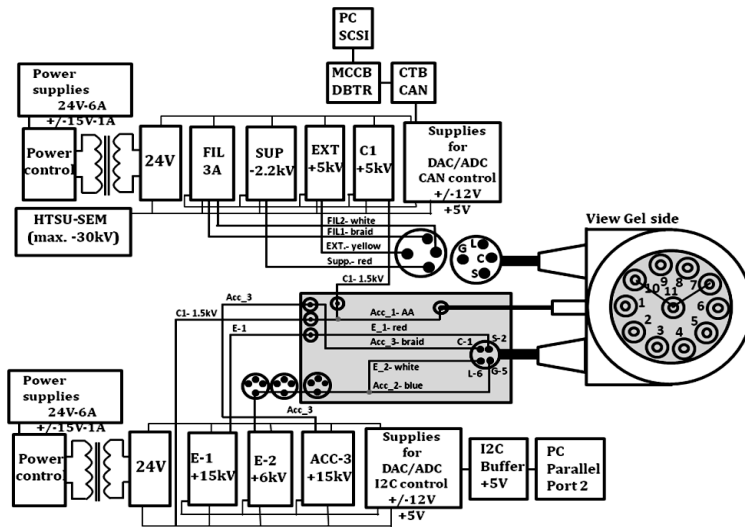


Figure 4.2.2 Schematic overview of current and voltage supplies of the MBS+ACC module and their connection path to the corresponding elements and to the gun head. The FGSU1 of the SEM is lifted to a maximum voltage of -30 kV by the HTSU. The FGSU2 supplies the potentials of the multi beam source module and its local ground is lifted through the C₁ output of the FGSU1. The FGSU1 is controlled using the FEI standard program and PC, whereas the FGSU2 is controlled externally by a home-made program and a separate PC.

The FGSU2 is controlled independently from FGSU1 via a homemade program and a separate PC. Figure 4.2.2 also shows a schematic drawing of the connection paths and their corresponding pins in the gun head with different numbers associated to different electrodes. Notice that this side of the gun head will be fixed to the CF100 flange pins.

4.3 Summary

The actual fabrication of the MBS components, their cleaning and pre-test, the method of assembly and alignment of the parts are described in detail. The ways to overcome the issues related to vacuum and electronics of the system were also discussed.

5 CHAPTER

Experimental results of the multi beam scanning electron microscope

"A theory is something nobody believes, except the person who made it. An experiment is something everybody believes, except the person who made it."
Albert Einstein

This chapter presents the performance of the MBSEM. It consists of two subsections: The first section is about the first experimental results obtained with our MBSEM. Throughout this section, at first we show, for the very first time ever, that it is possible to have 196 (an array of 14×14) focused beams of a multi electron beam source onto a specimen using standard SEM optics. To see the multiple focused beams on the sample directly, a YAG screen with a CCD camera was placed in the SEM sample stage producing direct images of 196 beams in the SEM chamber. Afterwards, the total current delivered by the MBS to the SEM column was measured in the Coulomb tube to be 150nA which is in a perfect agreement with its calculated value.

The next step is to characterize each beam in terms of beam current and beam size. To measure the probe current of every beam, first the total current of all the beams at the sample was measured by focussing them in a single spot into a Faraday cup placed in the sample stage. By making a scanning-transmission-like image of an aperture using multiple beams, it was found that this total current is uniformly distributed over 196 beams and from there the current of every beam is estimated which is also found to be in a perfect match with its calculated value. Due to the practical limitations however, the first try of simultaneous measurement of the beam size wasn't satisfactory and it was found to be much larger than expected. This is attributed to the

limited accuracy of the photocathode in collecting the transmitted signals. On the other hand, the individual beam size measurement, by using MBSEM in its single beam mode revealed that all the beams are the same in size with a sub-2nm resolution, very close to the theoretical calculated data. The single beam mode of the MBSEM can basically be done by cutting off all the beams but one in the pump aperture located at the C₂ lens and directing that beam to the column using “gun tilt and gun shift” coils around the Coulomb tube. In the second sub-section, the result of simultaneous multi-beam size measurement using a recently developed 11 zones STEM detector is presented. The results show that indeed not only the multiple focused beams are having the same size but also the resolution obtained by each beam is in the order of 1-2 nm as it is expected from the calculations.

5.1 Multi-beam scanning electron microscope: Experimental results¹

5.1.1 Abstract

The authors present the first results obtained with their multi-beam scanning electron microscope. For the first time, they were able to image 196 (an array of 14×14) focused beams of a multi electron beam source on a specimen using single beam scanning electron microscope (SEM) optics. The system consists of an FEI Nova-nano 200 SEM optics column equipped with a multi electron beam source module. The source module consists of the multi beam source and an accelerator lens. In the multi beam source, the wide angle beam of a high brightness Schottky source is divided into 196 beam-lets and focused by an aperture lens array. The accelerator lens is positioned in the image plane of the multi beam source to direct the beams toward the SEM column. The array of source images is further imaged by the SEM magnetic lenses and the beam opening angle is defined at the variable aperture of the SEM. The system is

¹ This section is from the paper “A. Mohammadi-Gheidari, C.W. Hagen and P. Kruit, J. Vac. Sci. Technol. B 28 (6) (2010) C6G5”.

designed to deliver 14×14 arrays of beam-lets with a minimum probe size of 1nm. In this article, the performance of the system is examined for a fixed magnification case.

5.1.2 Introduction

There is a growing demand to make sub-50 nm features in laboratories and the semiconductor industry. To fabricate and inspect such small structures, light based systems can no longer be used. Charged particle lithography and microscopy tools provide the highest resolution, but they are not a competitive alternative because of their low throughput. The latter is a direct consequence of the limited probe current, I , that can be achieved in a small probe, as given by:

$$I = B_r U \pi^2 \alpha^2 \frac{d_{geo}^2}{4} \quad (5.1)$$

Where B_r is the reduced brightness of the electron source, U is the beam acceleration energy, α is the half opening angle at the probe and $d_{geo} = M \cdot d_v$ is the geometrical source image.

Any increase in current will degrade the resolution due to the limited B_r of the electron source. Moreover, there is a limit to the probe current, for a given resolution, because of the statistical Coulomb interactions. Multi-beam systems can enhance the throughput by several orders of magnitude.

Many approaches have been tried to make multi electron beam systems over the last decades [1-11]. One of the major challenges in multi electron beam systems is the electron source. To create multiple beams, different methods are available. In the single column approach, multiple beams are created either by using multiple sources [4-6] or by using a single source which is split into multiple beam-lets using apertures [7-12]. Multiple sources are either photo-cathodes or cold field emitter arrays. Photo-cathodes have problems with poor current stability, short life time and low brightness [12-17]. Cold field emitters, on the other hand are promising candidates due to their high brightness, small virtual source size, and low energy spread. They

can be produced easily and cost effectively in a micro fabricated array. However, years of research and investment has not yet produced emitters that are sufficiently stable and reproducible to be useful in multi-beam systems [18-21]. As mentioned earlier, in the single source approach, the wide angle beam is split into many sub-beams. Two kinds of sources have been used so far: thermionic sources, such as LaB₆, and CRT- type sources as used by Mapper (e.g. Ref [22]). Both emitters provide a very high current, but for high resolution applications, the brightness is too low.

We have developed a multi electron beam scanning electron microscope (MBSEM) as a tool for fast and high resolution Electron Beam Induced Deposition (EBID). This system is able to deliver 196 beam-lets, each of which is focused down to a 1nm spot, similar to state of the art single beam SEMs. Our system uses a ZrO/W Schottky source, a source with a high brightness and good current stability [23, 24]. Recalling equation (5.1), this means we can achieve 32 pA current in a 1nm spot. Depending on the pattern to be written, this system enhances the writing speed up to 196 times. A simple example shows the importance of the MBSEM as a high resolution and fast EBID system: suppose we make a 10×10 μm² array of 1 nm³ dots at 10 nm pitch using a dose of 4 pC/nm³, and a beam current of 25 pA. With a single beam SEM, the total writing time is almost two days of continuous writing. With a MBSEM, it takes only 20 minutes. This system is mainly developed for high throughput fabrication of sub-10 nm structures by EBID, where resist based electron beam lithography fails [25]. It can also be used for high throughput electron beam lithography and inspection (the latter, of course, only after a special detector has been developed). The aim of this article is to present the performance of the MBSEM.

5.1.3 MBSEM system design

A very brief description of the electron optical working principle of the MBSEM is given here. The system consists of an FEI Nova-nano 200 SEM equipped with the multi electron beam source module.

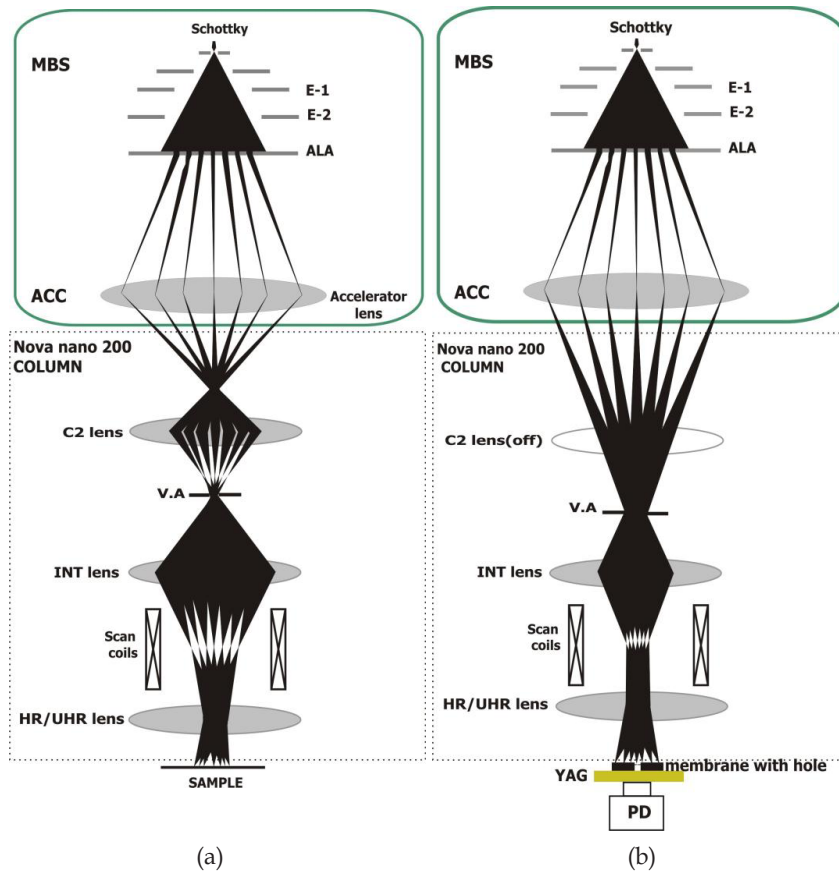


Figure 5.1.1a) Schematic overview of the electron optical system in the MBSEM, b) Schematic illustration of the MBSEM with a fixed magnification (C_2 lens off); the combined setup of “membrane with hole / YAG / PD” is used to measure the individual beam size.

Figure 5.1.1a shows a schematic overview of the electron optical design of the MBSEM. As a consequence of using a single optical column to image all beam-lets, a common crossover of all beams may degrade the system performance at high currents due to the statistical Coulomb interactions. Because of its high resolution application, the total current in the MBSEM is relatively low and the Coulomb interaction in the crossovers is less severe. In fact, these crossovers can even be of use to change the system magnification (first crossover) or to correct the astigmatism of all beams simultaneously

(second or third crossover) using a single stigmator. The multi beam source module is composed of two crucial components: the Multi Beam Source (MBS) and the Accelerator Lens (ACC). In the MBS, the emission cone of a high brightness Schottky emitter is split into an array of focused beams by an aperture lens array (ALA). The ALA is a combination of two mechanical electrodes and an array of apertures of $18\mu\text{m}$ diameters with $25\mu\text{m}$ pitch micro-fabricated in a thin Si membrane. The MBS is uniquely designed to correct the field curvature, to have low spherical aberration aperture lenses and to nullify the chromatic deflection error [26, 27]. The single aperture array used in the MBS avoids any precise alignment of two or more electrodes which is the case, for instance, in a micro-Einzel lens array [11, 28]. In the MBS, multiple images of the source are positioned on the object principle plane of the accelerator lens to avoid chromatic deflection aberration and to minimize the off-axial aberration of the lens. The accelerator lens directs the beams toward the column and creates the first common crossover of all the beams in the Coulomb tube. By changing the strength of the accelerator lens, and thereby moving the position of the crossover, the system magnification can be changed. This crossover is further imaged by the magnetic condenser lens C_2 onto the Variable Aperture (VA) which acts as a current limiting aperture. With the VA, it is possible to manipulate the opening angle and consequently the probe current. The intermediate magnetic lens, INT lens, is used to image the VA onto the coma free plane of the objective lens to suppress the off-axis aberrations of the high resolution (HR) / ultra high resolution (UHR) objective lens. Further demagnification of the probes will be done by the UHR or HR lens.

The MBS is designed to create an array of focused beams in the ACC plane, with a geometrical spot size of 95nm at a pitch of $70\mu\text{m}$. The pitch to geometrical probe size ratio is conserved throughout the system. For a landing energy of 1.5keV in the ACC plane, the total current delivered by the MBS is 157nA , or 0.8nA per beam-let (with a typical reduced brightness of $5 \times 10^7 \text{ A/ (m}^2 \cdot \text{Sr} \cdot \text{V)}$) and a FW50 energy spread of 0.5eV for the Schottky

Experimental results of the multi beam scanning electron microscope

source [23, 24]). This current can be simply measured in the Coulomb tube. Depending on the required resolution, the current is further cut off by the VA.

For applications with a fixed total magnification, the C_2 lens can be switched off. The imaging sequence of this particular feature of the MBSEM is illustrated in Figure 5.1.1b, which is the situation of interest in this paper. This configuration is designed to give a 1nm spot at the wafer in UHR mode. The detailed electron optical calculation was presented in chapter 3 and will also be published elsewhere [29]. Table 5.1.1 summarizes the calculated electron optical parameters of the system with a fixed magnification and 1nm resolution in UHR mode.

Table 5.1.1 Calculated electron optical parameters of the system with a fixed magnification and 1nm resolution in UHR mode. (Note: C_{st} and C_{ct} stand for total Spherical and Chromatic aberration coefficients of the system at the sample respectively)

Parameter	Value
Total magnification (M_{tot})	0.0162
Pitch at the wafer (nm)	360
Geometrical spot (nm)	0.49
C_{st} image side (mm)	5.43
C_{ct} image side (mm)	3.07
Working distance (mm)	5
Acceleration voltage (kV)	15

Figure 5.1.2 shows the calculation results of the total axial spot size and different aberration contributions in it as a function of VA size. As can be seen from the figure, the smallest axial probe size of $d_{tot} = 1.17\text{nm}$ is obtained for a VA of $20\ \mu\text{m}$. The corresponding optimum half opening angle of the beam is then $\alpha_i = 8.5\text{mrad}$.

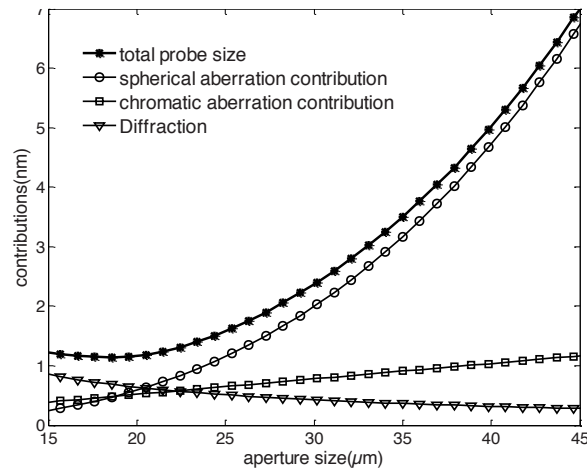


Figure 5.1.2 Calculation results of the total axial spot size and its different axial aberration contributions as a function of VA size.

5.1.4 MBSEM performance

The very first challenge is to image all beam-lets onto the specimen. To visualize the beams at the specimen level we mounted an yttrium aluminium garnet (YAG) screen and a charged coupled device (CCD) camera at the specimen position. Figure 5.1.3a shows an image of the de-focused array of beams in the chamber. This is the very first demonstration that we can image 196 (14×14) beam-lets using a single electron optical column.

Now we need to characterize the beam-lets in terms of current, size, pitch and eventually brightness (not a subject of this paper). Unlike a single beam system, measuring the individual beam-let size of the MBSEM is not straight forward, because there is no full control over each beam-let. In a single beam system one can scan the beam across a sharp edge (Knife edge method) and the beam size is then determined by measuring the width of the intensity profile between two fixed levels (normally 25%-75% or a different portion depending upon the definition). Alternatively the resolution of the system can be quantified using the edge sharpness of features in the secondary electron images, e.g. nanogold balls (image processing). In our MBSEM all beam-lets can only be scanned simultaneously.

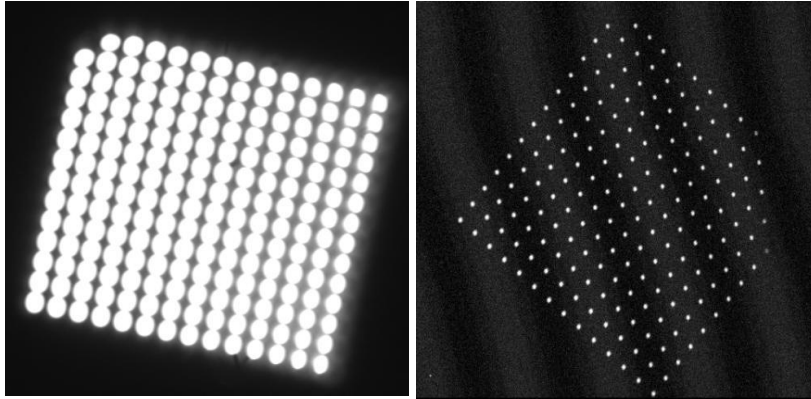


Figure 5.1.3a (left) direct image of 196 beams in the chamber onto a YAG screen and recorded with CCD camera (scale: 1mm×1mm) and Figure 5.1.3b (right) MBSEM image of single aperture (for scale: pitch $\approx 4\mu\text{m}$).

This means that the signal of one beam-let cannot be distinguished from the others. To overcome this problem, all beams are scanned simultaneously over an aperture. This aperture is a hole with a diameter of 220nm made by focused ion beam (FIB) drilling in a Silicon Nitride (Si_3N_4) membrane covered with titanium (Ti) on both sides. The diameter of the hole is smaller than the pitch between the beam-lets and the membrane is thick enough ($\approx 800\text{nm}$) to stop electrons of up to 20 keV. By integrating a YAG screen and a photodiode under the aperture and scanning the beam-lets over the aperture, each beam builds up a scanning-transmission-electron-microscope-like image of the aperture. A schematic of this experimental setup is illustrated in figure 5.1.1(b). Analyzing the intensity profile of the transmitted current for each beam-let gives a first measure of the size and pitch between the beams. Figure 5.1.3(b) shows the MBSEM image of the single aperture. Figure 5.1.4 shows a picture with an example of the image analysis, in which the measured pitch is about 400 nm and the beam size is 50 nm. The measured value for the pitch is close to its predicted value of 360 nm (see table 5.1.1) but the beam size is far from its predicted value of 1nm for a VA of 20 μm . This is not surprising as in the Knife Edge measurement method the quality of the aperture plays an important role. In fact, the accuracy of the beam size measurement mainly

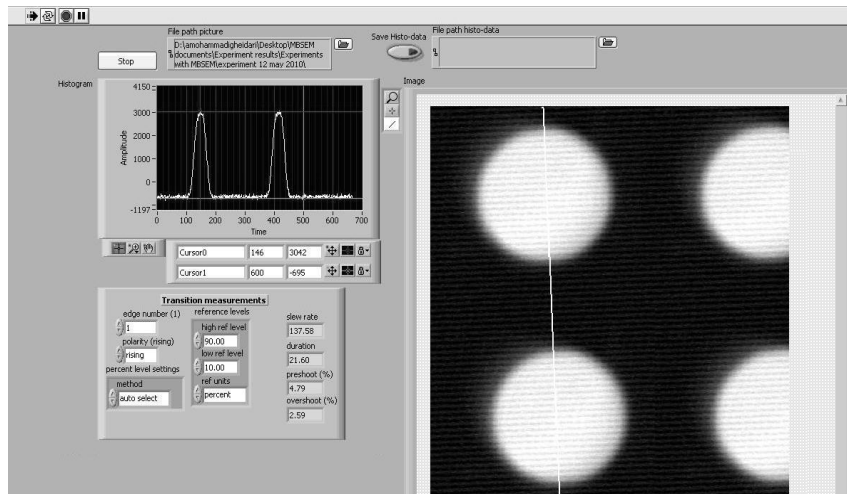


Figure 5.1.4 picture of the program used to analyze the beam size and pitch of the MBSEM.

depends on the quality of the edge over which the beam is scanned, and the high aspect ratio aperture used here is far from ideal. To improve the measurement, a rod of 20nm width is grown across the hole using EBID from a methyl-cyclopentadienyl-platinum-tri-methyl (MeCpPtMe_3) precursor. This already provides a much sharper edge.

Figures 5.1.5 (a) and 5.1.5 (b) show some typical results of this experiment where the 20nm rod is clearly imaged by all beams. The beam size is estimated by measuring the width of the intensity profile between two fixed levels (25%-75%) in the line profile. As before the measured pitch between the beams is 400 nm, but the measured beam sizes are around 14 nm. We have seen that after scanning the beams over this sample the EBID rod became thinner and shorter. It was disconnected from one side of the hole (see figure 5.1.6a). Figure 5.1.6b shows a result of the beam size analysis with a zoomed in image of a rod (inset) of width between 15 and 18nm. In this case the average measured beam size (25%-75% value) is 10nm. The measured beam size is clearly an upper limit, because of the somewhat poor image detection method with the photodiode.

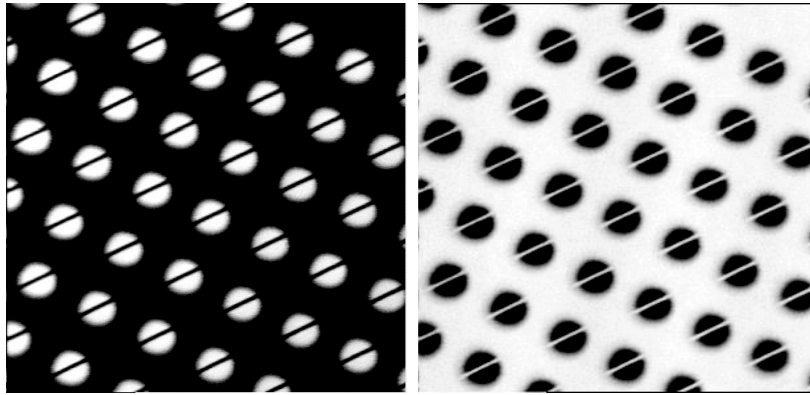


Figure 5.1.5a (left) Typical MBSEM transmission image of a single 220 nm diameter aperture with a 20 nm width EBID rod (UHR mode). Figure 5.1.5b (right) the same image with inverted contrast.

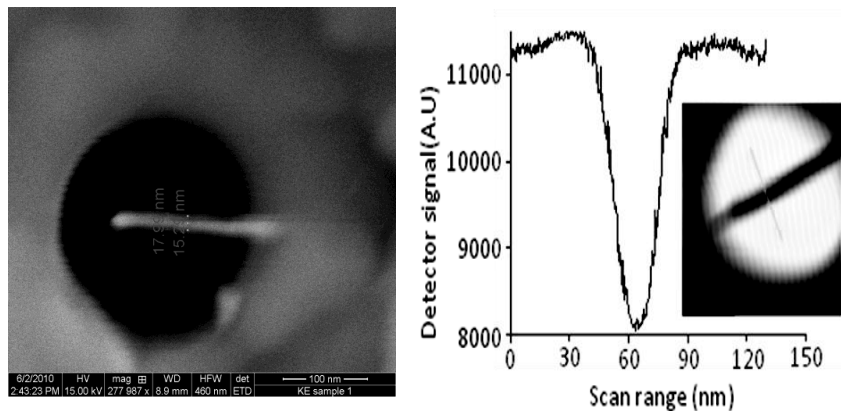


Figure 5.1.6a (left) SEM image of a FIB drilled aperture with a broken EBID rod attached. The width of the rod is 15 -18nm. Figure 5.1.6 b (right) Intensity profile across an EBID-rod and (inset) a zoomed in transmission MBSEM image of the rod.

The total current delivered by the MBS is measured at the Coulomb tube of the system. Prior to the measurement all beams were deflected using beam shift / tilt coils to the side of the Coulomb tube to make them all contribute to the measurement. To measure the total current delivered at the specimen level, all beams are focused into a Faraday cup and the total current of the system is measured for different VA of 20, 30, 40 and 50 μ m. Figure 5.1.7a shows the calculated total current as a function of VA and the measured values. It is observed that they are very close to the predicted values.

From Figure 5.1.7b it can be seen that the current distribution is almost uniform. The graph shows an integrated line profile of the indicated row (inset) in the array of beams. The area under each peak in this figure shows the total current confined in each probe. The maximum fluctuation between the areas was only 5% within a row. Similar results were obtained for different rows. This shows that the total current is uniformly distributed over 196 beams. For example for $V_A = 20 \mu\text{m}$, the measured total current is 6.1nA, i.e. the current per beam-let is 31.1pA, and the calculated current per beam-let is 31.5 pA. The total current delivered by the MBS to the system can be measured in the Coulomb tube and is found to be 150 nA which is also very close to the predicted value. The current stability is also a very important factor. The total current fluctuation was captured for more than 2 hours of operation, and it turned out to be negligible.

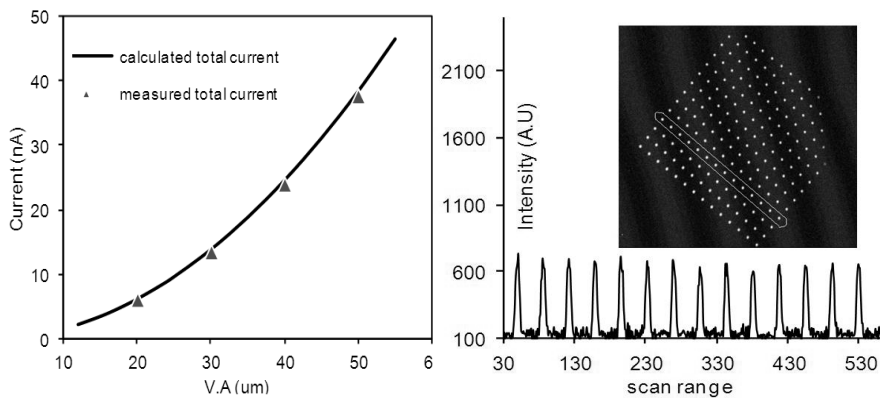


Figure 5.1.7a (left) the calculated total current of 196 beams and the measured values as a function of VA and figure 5.1.7b (right) the graph shows an integrated intensity profile of the row of beam-lets as indicated in the inset, which shows the array of beam-lets.

Also the long term stability of the multi beam source module is very good, as it is already reliably operating now for more than a year². To further improve the beam size measurements, we intend to install a scanning

² It actually worked reliably from 2009 till 2013, so for four years, much longer than expected life time of Schottky sources, and then the Schottky source was replaced.

transmission electron microscopy (STEM) detector and use angular dark field (ADF) imaging.

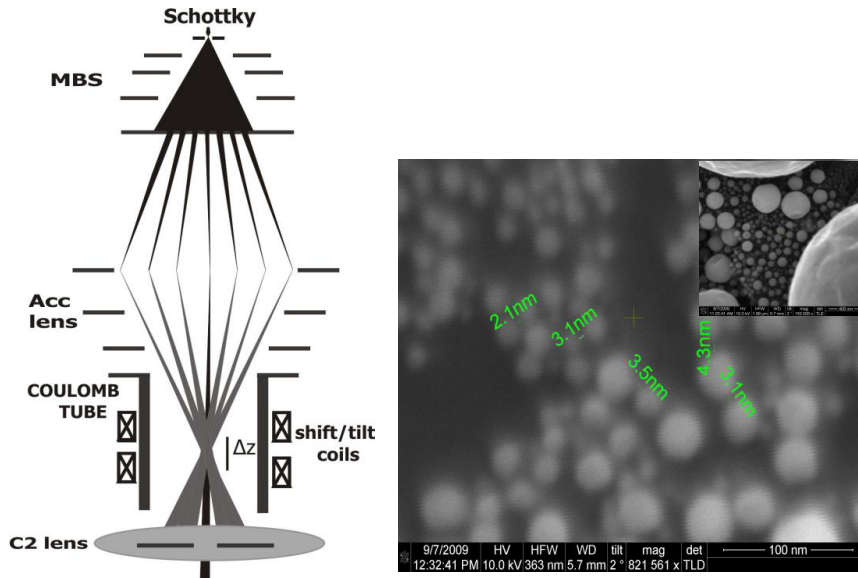


Figure 5.1.8a (left) Working principle of single beam operation of the MBSEM (only the indicated beam (black) is not blanked) and figure 5.1.8b (right) SEM image of tin balls made by a randomly chosen off-axis beam of the MBSEM. (Inset) a slightly zoomed out image (scale bar is 400nm).

5.1.5 Single beam performance of the MBSEM

As mentioned before it is possible to move the first common crossover of the beam-lets by changing the accelerator lens strength. As schematically illustrated in figure 5.1.8a, it is possible to position the crossover such that all beams, but one, are stopped in the pump aperture located in the C₂ lens. Using beam shift / tilt coils, this beam can be further aligned and directed toward the SEM column. Figure 5.1.8b shows a typical result of MBSEM performance as a standard single beam SEM. This image is made with a randomly chosen off-axis beam-let by beam shift / tilt coils. It should be noted that the same experiment has been carried out with some other beam-lets and they revealed the same imaging properties. The current measured for the beam was 43 pA and the resolution is measured to be less than 2nm using

a proprietary image processing program from FEI which essentially measures edge resolution of sharp features in the image. The resolution can also be estimated from the gap between tin balls in the image (green lines and numbers in fig.5.1.8b), in which a spacing less than 2 nm between balls is still distinguishable.

5.2 Beam size measurement using a STEM detector

As mentioned earlier, the previous simultaneous beam size measurement of the MBSEM was limited by the accuracy of the measurement method. This was mostly due to the use of an inadequate signal detection device, a photodiode. To further improve the detection method we have replaced the photodiode with a more sophisticated transmission signal detection device, a STEM detector, equipped with 11 active areas collecting transmitted signals for larger angles. The beam size measurement experiment that was described in the previous section was then repeated. Figure 5.2.1 shows a picture of the hole with a rod as taken with an outer beam of the MBSEM using the STEM detector.

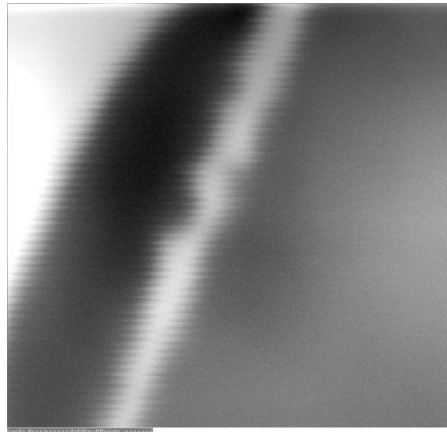


Figure 5.2.1 STEM image of the rod / hole by the outer beam of the MBSEM.

As can be clearly seen, very small features can be resolved in the rod showing that the real probe is indeed much smaller than what was measured

Experimental results of the multi beam scanning electron microscope

before. Even with this image it is still not straightforward to determine the probe size, especially because the image is strongly suffering from noise. This noise, especially 1000Hz, is most probably originating from the Turbo Molecular vacuum pump of the system located at the bottom of the SEM chamber. However, we can compare the resolution of the MBSEM with that of standard high resolution single beam SEMs. Two pictures shown in figures 5.2.2(a) and 5.2.2(b) are the images of the same sample taken by a Quanta-FEG SEM from FEI Company with the same magnification and using the same STEM detector. These images are also taken at 15KV and almost the same probe current. The horizontal field of view (HFW) for the first image is 240nm. As it is clearly seen from the pictures, apart from the fact that the picture taken by the MBSEM has more vibration induced noise, the resolution as determined from the pictures taken by the Quanta FEG and the MBSEM are comparable or even should we say the one from the MBSEM is better!

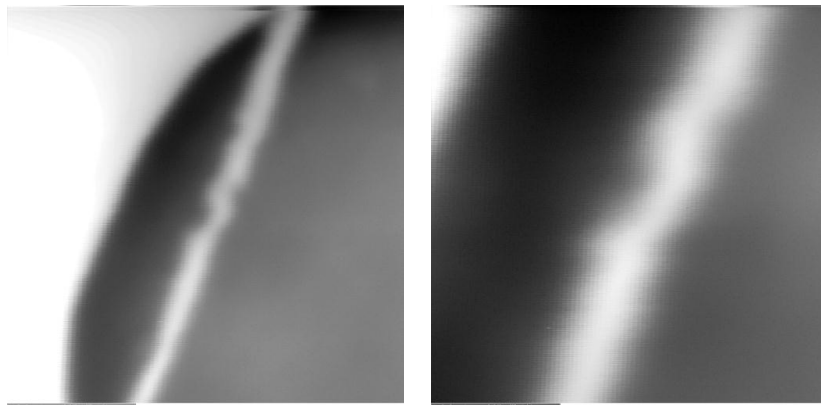


Figure 5.2.2a (left) STEM image of the rod /hole sample taken by a high resolution Quanta-FEG SEM from FEI Company and figure 5.2.2b (right) the same picture but highly zoomed in.

The resolution of the Quanta-FEG SEM is perhaps not quite 1nm but sure enough it is below 5nm. Therefore, we are confident that the probe size of the MBSEM is around its predicated value of 1nm.

5.3 Summary

We have developed a multi beam scanning electron microscope (MBSEM) dedicated for high resolution, high throughput lithography and microscopy. For the first time we were able to image 196 beams of a multi electron beam source on a specimen using single beam SEM optics. The source has a stable operation now for more than a year. The probe current and the probe size measurement results show a promising performance for the MBSEM. The measured pitch, current per beam and total current in the Coulomb tube are in good agreement with the predicted values. The current per beam is comparable with that of a single beam SEM. Although the first attempt of simultaneous beam size measurement weren't satisfactory due to the poor transmission signal collection efficiency by the photodiode, we are confident that the beam sizes are quite close to the calculated values based on the single beam performance of the system. However, to make sure, we repeated the beam size measurement using a recently developed 11 zones STEM detector and the result of these measurements indicate that indeed the beams are having the same size of 1-2nm. It was found that the measurement is limited by 1000Hz vibration most probably originating from the Turbo Molecular vacuum pump of the system.

5.4 Bibliography

- [1] B. Roelofs, and J. Barth, *Microelectron. Eng.* 2 (1984) 259.
- [2] M. McCord, *J. Vac. Sci. Technol. B* 15(6) (1997) 2125.
- [3] T. Chang, M. Mankos, K. Lee, L. Muray, *Microelectron. Eng.* 57 (2001) 117.
- [4] E. Yin, A.D. Brodie, F.C. Tsai, G.X. Guo, and N.W. Parker, *J. Vac. Sci. Technol. B* 18 (2000) 3126.
- [5] S. Tanimoto, et al., *Jpn. J. Appl. Phys.* 42 (part 1) (2003) 6672.
- [6] S.T. Coyle, et al., *J. Vac. Sci. Technol. B* 22 (2004) 501.
- [7] H. Yasuda, et al., *J. Vac. Sci. Technol. B* 14 (1996) 3813.
- [8] G. Winogard, et al., *J. Vac. Sci. Technol. B* 18 (2000) 3052.

- [9] M. Muraki and S. Gotoh, *J. Vac. Sci. Technol. B* 18 (2000) 3061.
- [10] N. Nakasuji, S. Yoshikawa, T. Satake, and N. Noji, *Jpn. J. Appl. Phys.* 44 (part 1) (2005) 5570.
- [11] O. Kamimura, et al., *J. Vac. Sci. Technol. B* 25 (1) (2007) 140.
- [12] G. Schwind, G. Magera, L. Swanson, *J. Vac. Sci. Technol. B* 24(6) (2006) 2897.
- [13] M. Mankos, et al., *J. Vac. Sci. Technol. B* 18(6) (2000) 3010.
- [14] X. Jiang, C. Berglund, A. Bell, W. Mackie, *J. Vac. Sci. Technol. B* 16(6) (1998) 3374.
- [15] M. Wieland, B. Kampherbeek, P. Addressi, P. Kruit, *Microelectron Eng.* 57-58 (2001) 155.
- [16] D. Schroder, R. Thomas, J. Vine, H. Nathanson, *IEEE Tran. Electron Devices* ED21 (12) (1974) 785.
- [17] T. Teepen, et al., *J. Vac. Sci. Technol. B* 23(2) (2005) 359.
- [18] W. Hofmann, L.-Y. Chen, N. MacDonald, *J. Vac. Sci. Technol. B* 13(6) (1995) 2701.
- [19] Y. Yamaoka, S. Kanemaru, J. Itoh, *Jpn. J. Appl. Phys.* 35 (1996) 6626.
- [20] J.Y. Park, et al., *J. Vac. Sci. Technol. B* 15(6) (1997) 2749.
- [21] G. Guo, et al., *J. Vac. Sci. Technol. B* 19(3) (2001) 862.
- [22] A. J. van den Brom et al, *J. Vac. Sci. Technol. B* 25(6) (2007) 2245.
- [23] M.S. Bronsgeest, PhD Thesis, Delft University of Technology (2009).
- [24] M.J. Fransen, M.H.F. Overwijk, and P. Kruit, *Appl. Surf. Sci.*, 146(1-4) (1999) 357.
- [25] A.E. Grigorescu, M.C van der Krogt, E.W.J.M van der Drift, C.W. Hagen, *J. Micro/Nanolith. MEMS MOEMS*, Vol. 7, 013005 (2008).
- [26] Yanxia Zhang and Pieter Kruit, *Phys. Procedia* 1 (2008) 553.
- [27] M.J van Bruggen, PhD Thesis, Delft University of Technology (2008).
- [28] M. J van Bruggen, B. Van Someren and P. Kruit, *J. Vac. Sci. Technol. B* 25(6) (2007) 2245.
- [29] A. Mohammadi-Gheidari, et al., in preparation.

Parallel EBID with the MBSEM

"There are plenty of rooms at the bottom."

Richard Feynman

This chapter addresses the very first result of high throughput patterning through electron beam induced deposition (EBID) using 196 beams. The MBSEM is used to deposit 196 dots simultaneously on the sample.

Parallel electron-beam-induced deposition using a multi-beam scanning electron microscope¹

Abstract

Lithography techniques based on electron-beam-induced processes are inherently slow compared to light lithography techniques. The authors demonstrate here that the throughput can be enhanced by a factor of 196 by using a scanning electron microscope equipped with a multi-beam electron source. Using electron-beam induced deposition with $\text{MeC}_p\text{PtMe}_3$ as a precursor gas, 14×14 arrays of Pt-containing dots were deposited on a $\text{W}/\text{Si}_3\text{N}_4/\text{W}$ membrane, with each array of 196 dots deposited in a single exposure. The authors demonstrate that by shifting the array of beams over distances of several times the pitch, one can deposit rows of closely spaced dots that, although originating from different beams within the array, are deposited within 5nm of a straight line.

¹ This chapter is from the paper "P.C. Post, A. Mohammadi-Gheidari, C.W. Hagen and P. Kruit, J. Vac. Sci. Technol. B 29 (6) (2011) F310".

6.1 Introduction

Using resist-based Electron Beam Lithography (EBL), one can routinely fabricate patterns down to 10 nm, and even down to about 5 nm [1] when using ultrathin resists and dedicated development processes. Using Electron-Beam-Induced Deposition (EBID), even smaller patterns of 1 nm in size can be written [2]. In EBID, a focused electron beam dissociates precursor molecules adsorbed on a substrate surface, leaving a solid deposit on the surface and gaseous fragments that can be pumped away. The reader interested in EBID is referred to some recently published review papers [3-6]. The advantage of EBID over EBL is that it is a direct deposition technique and provides a smaller minimum feature size. However, both EBL and EBID are inherently slow lithography techniques compared to light lithography techniques, because they are serial writing processes rather than parallel. However, in order to enhance the throughput, one could write with many electron beams in parallel. Several authors have proposed and/or built such multi-beam lithography systems [7-20], which can be divided roughly into four types:

(i) Multiple optical columns with multiple sources [10-12], (ii) single column with multiple sources [13-15], (iii) single column with single source [16-22], and (iv) multiple cold field emitters in close proximity to the wafer [23]. Although the latter system seems attractive, because it does not require any optics, it has been not demonstrated yet. The system we designed is a single column, single source system. We developed a multi-beam electron source based on a standard single Schottky electron emitter mounted on a regular Scanning Electron Microscope (SEM). This Multi Beam SEM (MBSEM) distinguishes itself from other systems in that it projects an array of 14×14 focused beams onto a sample with a probe size and current per beam comparable to that of a standard single-beam SEM [24,25], i.e., 196 beams, each with a 1nm probe size and 30pA of current.

The objective of this article is to report the parallel direct deposition of dots using multi-beam EBID. These experiments serve as a first test of the MBSEM as a multi-beam EBID system.

6.2 Experimental

• 6.2.1 The Multi-beam SEM

Although the design of the multi beam electron source and its integration in a standard SEM has been described in detail elsewhere [24-26], it is useful here to give a brief description of the MBSEM. In Figure 6.1 a schematic overview of the system is shown. It consists of an FEI Nova-nano 200 SEM equipped with the multi beam electron source module.

The module is composed of two crucial components: (i) the Multi-Beam Source (MBS) and (ii) the Accelerator Lens (Acc). In the MBS, the full emission cone of a single high brightness Schottky thermal field emission source is split up into an array of 14×14 focused beams by an aperture lens array (ALA). The combination of the ALA, which consists of a micro-fabricated Si membrane with apertures of $18 \mu\text{m}$ diameter at a $25 \mu\text{m}$ pitch, the two macro-electrodes, E-1 and E-2, and the extractor electrode, is uniquely designed to correct for field curvature, to have low spherical aberration aperture lenses. The accelerator lens accelerates the beams to the required final energy

and directs the beams to the SEM column. Although the system is designed for a variable magnification, for the present experiments we used a fixed magnification, with the first magnetic condenser lens (C_2) switched off.

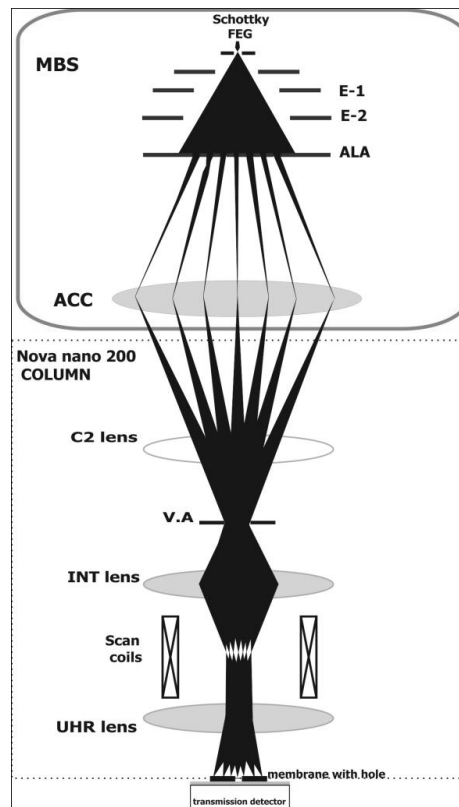


Figure 6.1 Schematic drawing of the multi-beam SEM mode when the C_2 lens is switched off. This is the mode in which the deposition experiments were performed.

The crossover at the current limiting variable aperture is imaged by the intermediate lens (INT) onto the coma-free plane of the ultra-high resolution objective lens (UHR). Further de-magnification of the probes is done by the UHR lens. The typical optical design parameters of this mode at 15keV acceleration energy are as follows: each beam has a 1 nm spot size at the sample, at a pitch of 360 nm at the sample, and a current of 31pA per beam, and the total footprint of the 14×14 array is (5×5) μm².

- 6.2.2 Multi-beam EBID

Focusing the array of 196 beams onto a sample is not straightforward. Using the regular Everhart-Thornley secondary electron detector, one collects the secondary electrons of all 196 beams simultaneously, such that one beam cannot be distinguished from the others. Therefore we used a transmission detector in combination with a membrane sample with an aperture. The membrane is a W/Si₃N₄/W sandwich, with layer thicknesses of 200nm/50nm/200nm respectively, sufficiently thick to stop 15 keV electrons. The aperture is just a hole in the membrane and is created by Focused Ion Beam (FIB) milling, using an FEI Quanta 3D FEG Dual Beam system. A Gallium ion beam was used at an energy of 30keV and a beam current of 30 pA. The milling process was observed using the electron beam and secondary electron detection, and the end point of the process was determined by measuring the transmission signal of the transmission detector below the membrane. Several holes were milled in the membrane at least 20μm apart, i.e. at a distance larger than the size of the array of beams. In order to keep multiple beams from passing through the aperture, the aperture diameter (typically about 250 nm) has to be smaller than the beam pitch of 360 nm.

Scanning the array of 196 beams over a single aperture and detecting the bright field transmission signal results in an image of 196 bright spots. The best focusing of the beams was obtained by optimizing the edge contrast of these spots.

For the deposition, we used the platinum precursor methyl-cyclopentadienyl-trimethyl-platinum (MeCpPtMe_3 , CAS: 94442-22-5) as a precursor gas. The specimen chamber was filled with precursor gas at a pressure of 2.5×10^{-5} mbar. After the beams were focused, the membrane was displaced (typically by 10 μm) in order to obtain a fresh deposition area away from the aperture. The defocus due to the displacement was checked by displacing the membrane to a different aperture, even as far as 100 μm away and no severe de-focus was observed. To expose the adsorbed precursor layer, we used Labview-based homebuilt patterning software that controls the position of the array of beams and the exposure time. As the microscope does not have a fast blanker, the beam was un-blanked just before the start of the writing sequence and then moved to the deposition area where the writing sequence was completed, after which the beam was moved away from the deposition area, where the beam was blanked. In this way, spurious deposition close to the deposition area during the relatively slow blanking time is avoided. After the deposition, the gas was pumped out and the dot arrays were imaged by taking single-beam SEM images in our FEI Quanta FEG Dual Beam system.

6.2 Results and discussions

Figure 6.2 shows a single beam image of an array of Pt-containing EBID dots, deposited with a single exposure in the MBSEM. The exposure time was 20 s. This is a relatively long exposure time, resulting in rather large deposits. This is done on purpose because it leads to better contrast images than when tiny sub-10 nm dots are deposited, and it makes it easier to judge the quality of the array of beams. The dots have a diameter of about 70 nm, and the average pitch is 436 nm. The total field of 14×14 dots measures $(5.7 \times 5.7) \mu\text{m}^2$. On the left-hand side of the image, the dots still have a slightly comet-like shape. This is because the crossover of the beams is not imaged exactly in the coma-free plane of the objective lens. Also, the fact that some of the beams are missing is due to a slight misalignment of the optical system.

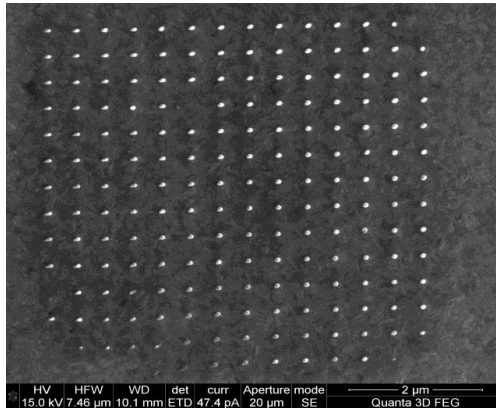


Figure 6.2 Single-beam SEM image of an array of EBID dots, grown on the W/Si₃N₄/W membrane sample, using a single 20 s exposure in the multi-beam SEM, at 15keV. The precursor gas used was MeCpPtMe₃, at a pressure of 2.5×10^{-5} mbar. A few dots are missing, and the dots on the left hand side reveal the presence of coma. This is due to misalignment, and the beams not being imaged exactly in the coma free plane of the objective lens.

To demonstrate the possibilities of multi-beam EBID, we did another experiment in which we shifted the array of beams five times over a relatively large distance of about $2 \mu\text{m}$ (4.6 times the beam pitch), each time exposing the sample for 15s. The single beam SEM image of the resulting assembly of dots is shown in figure 6.3. The markers in this figure serve as an aid to help the observer easily determine which dot originates from which exposure.

The square markers indicate dots deposited by the same beam at five successive positions of the array of beams, and the hexagonal-, star-, and circle-shaped markers indicate three neighbouring dots, deposited at the five different positions of the array of beams. It is easily seen from figure 6.3 that rows of dots can be created in which adjacent dots do not originate from adjacent beams in the array of beams (see the short line connecting three dots in a row). When choosing the proper direction in which the array of beams is to be shifted, dots exposed by beams far apart in the array can be grouped together to form regular rows of dots over large distances, or even continuous lines if the dots overlap. This uniformity of the resulting pattern depends on the accuracy of the array positioning and on the regularity of the array of

beams, i.e., on the pitch uniformity. When attempting to determine the orientation of the array such that the displacement of the array of beams can be chosen along the preferred direction, *in situ* imaging with the MBSEM is very helpful.

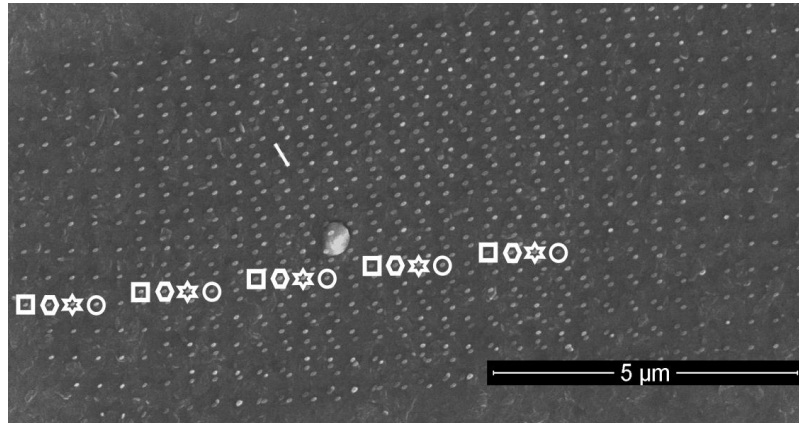


Figure 6.3 Single-beam SEM image of multi-beam EBID dots grown in 5 successive 15 s exposures in the multi-beam SEM, at 15 keV, each exposed position shifted by about 2 μm . The square markers indicate a particular dot written by the same beam in 5 successive exposures, and the hexagons, stars, and circles indicate, likewise, three neighboring dots. The potential formation of rows of dots is illustrated by the small line connecting three lined-up dots written by three different beams. The precursor gas used was MeCpPtMe₃, at a pressure of 2.5×10^{-5}

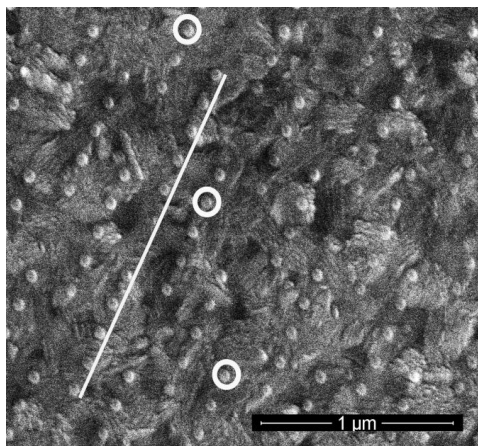
Of course, there is only one secondary electron detector, which collects the signals of all 196 beams simultaneously. The resulting image is a convolution of the deposited dot array and the 14×14 array of beams that are scanned over the dot array. Because both the deposition and the imaging are done with the same array of 196 beams, the resulting image still contains useful information, such as the orientation of the array of dots, provided the pitch variation within the array of beams is sufficiently small.

In figure 6.4 we demonstrate the deposition of a linear row of 150 nm spaced dots by shifting the array five times over a distance of 0.84 μm (twice the beam pitch) in the direction indicated by the circles in figure 6.4. The line drawn along the ten dots serves as a guide for the eye in order to demonstrate

that the ten dots, all originating from beams located far apart within the array of beams, can be deposited within a distance of about 5 nm from a straight line, as is easily judged from the width of the line, which is 20 nm.

We demonstrated the potential of multi-beam EBID as a direct lithography technique, with a 196-fold speed enhancement with respect to single beam EBID. The meaning of this becomes clear when considering large area deposition. As an example, suppose we were to upscale the size of the array of dots in figure 6.3 to an area of $(100 \times 100) \mu\text{m}^2$ (~140000 dots). In a single beam EBID process, this would take 24 days, whereas with multi-beam EBID this can be done in only 3 hours!

Figure 6.4 Single-beam SEM image of 5 successive 15 s exposures in the multi-beam SEM, at 15 keV, shifted with respect to each other by $0.84 \mu\text{m}$, in the direction of the imaginary line connecting the three circles. The precursor gas used was MeCpPtMe_3 , at a pressure of 2.5×10^{-5} mbar. The 20 nm thick line is a guide to the eye to judge how well the dots are positioned with respect to a mutually connecting straight line, which is better than 5 nm. As each dot within an array of 5 dots originates from a different beam, this demonstrates the patterning capability of the multi-beam SEM.



6.3 Summary and conclusions

We used a scanning electron microscope equipped with a multi-beam electron source for the electron-beam-induced deposition (EBID) of 196 dots simultaneously. We have learned how to operate the instrument in order to do parallel EBID, which introduces some new difficulties in terms of focusing and imaging. We have demonstrated that by shifting the array of beams over distances of several times the beam pitch, we can deposit rows of closely

spaced dots in which dots originating from different beams within the array are positioned within 5 nm of a straight line. This shows that the variation in pitch within the array of beams is smaller than 5 nm and that we have good control over the positioning of the array of beams. The dots we deposited were not the smallest possible ones, for reasons of visibility in the images. It was more important here to demonstrate the potential of multi-beam EBID, in terms of patterning capability and speed enhancement, than to obtain sub-10 nm resolution. In order to develop the multi-beam SEM into a full lithography tool, we plan to put a microfabricated deflector plate at the position of the first electrode of the accelerator lens to obtain beam blanking of each beam individually. Furthermore, the electronic controls of the new multi-beam source have to be integrated as a single unit in the control electronics of the standard SEM, in order to facilitate easy operation of the microscope and enable rapid switching between multi-beam mode and single-beam mode. The latter is really desirable for imaging purposes.

6.4 Acknowledgments

We gratefully acknowledge V.G. Kutchoukov for fabrication of the sandwich samples, F. Berwald for developing the patterning software, and the support provided by NanoNed and the EU Cost Action CM0601 "Electron Controlled Chemical Lithography" (ECCL).

6.5 Bibliography

- [1] J. K. W. Yang, et al., *J. Vac. Sci. Technol. B* 27 (2009) 2622.
- [2] W. F. van Dorp, et al., *Nano Lett.* 5 (2005) 1303.
- [3] N. Silvis-Cividjian and C. W. Hagen, *Advances in Imaging and Electron Physics* (Elsevier, Amsterdam, 2006), Vol. 43.
- [4] K. Furuya, *Sci. Technol. Adv. Mater.* 9 (2008) 014110.
- [5] I. Utke, et al., *J. Vac. Sci. Technol. B* 26 (2008) 1197.
- [6] W. F. van Dorp and C. W. Hagen, *J. Appl. Phys.* 104 (2008) 081301.

Chapter 6.

- [7] B. Roelofs and J. Barth, *Microelectron. Eng.* 2 (1984) 259.
- [8] M. McCord, *J. Vac. Sci. Technol. B* 15 (1997) 2125.
- [9] T. Chang, et al., *Microelectron. Eng.* 57–58 (2001) 117.
- [10] L. P. Muray, et al., *J. Vac. Sci. Technol. B* 18 (2000) 3099.
- [11] T. R. Groves and R. A. Kendall, *J. Vac. Sci. Technol. B* 16 (1998) 3168.
- [12] T. Haraguchi, et al., *J. Vac. Sci. Technol. B* 22 (2004) 985.
- [13] E. Yin, et al., *J. Vac. Sci. Technol. B* 18 (2000) 3126.
- [14] S. Tanimoto, *Jpn. J. Appl. Phys., Part 1* 42 (2003) 6672.
- [15] S. T. Coyle et al., *J. Vac. Sci. Technol. B* 22 (2004) 501.
- [16] H. Yasuda, et al., *J. Vac. Sci. Technol. B* 14 (1996) 3813.
- [17] G. Winograd, et al., *J. Vac. Sci. Technol. B* 18 (2000) 3052.
- [18] M. Muraki and S. Gotoh, *J. Vac. Sci. Technol. B* 18 (2000) 3061.
- [19] N. Nakasuji, et al., *Jpn. J. Appl. Phys., Part 1* 44 (2005) 5570.
- [20] O. Kamimura et al., *J. Vac. Sci. Technol. B* 25 (2007) 140.
- [21] J. Basu, et al., *Appl. Phys. Lett.* 93 (2008) 133104.
- [22] H. M. Kim, et al., *J. Vac. Sci. Technol. B* 27 (2009) 2553.
- [23] L. Dong, F. Arai, and T. Fukuda, *Appl. Phys. Lett.* 81 (2002) 1919.
- [24] A. Mohammadi-Gheidari, C. W. Hagen, and P. Kruit, *J. Vac. Sci. Technol. B* 28 (2010) C6G5.
- [25] A. Mohammadi-Gheidari and P. Kruit, *Nucl. Instrum. Methods Phys. Res. A* 645 (2011) 60.

7 CHAPTER

Summary and conclusions

“The real voyage of discovery consists of not in seeking new landscapes but in having new eyes.”

Marcel Proust

This chapter provides a general overview of the thesis and summarises the main conclusions.

- Summary

The first chapter is to be intended as an introduction for the whole thesis. Via a brief critical review of the history of the development of scanning electron microscopy, it is shown that most of the related research has always focused upon improving the resolution of the systems; sure enough, thanks to this trend, the resolving power of current SEMs is good enough for any kind of high resolution application. On the other hand, at least in the view of the author, this means that there is another parameter that needs renewed attention and a concentration of attempts for improvement: the system throughput. In particular, it is made clear that the throughput cannot be increased by simply pumping more electrons in the beam; more complex solutions must be envisaged.

Chapter 2 introduces the Multi-Beam Source (MBS) to be used in the MBSEM. The first part of the chapter provides a short survey of the various multi-beam sources found in the literature, plus the old MBS concept. The conclusion is that none of these multi-beam sources are appropriate and a new one has to be designed. The second part of the chapter deals with the

electron-optical design of the new MBS. The last two parts of the chapter are focused on the required tolerances of the MBS and on the effect of electron-electron interactions on its performance.

The third chapter consists of the following three parts. Part I presents the general rules and good practices for the design of a multi-beam SEM; the electron-optical behaviour of the system is described, and the electron-optical design of a coupling lens, an accelerator lens, is introduced; also, a recipe for the calculation/simulation of the axial and off-axial performance of the complete system is provided. The main message of this part is that designing a system capable of delivering multiple beams onto the sample, with a typical beam size and beam current (per beam) comparable to that of a state-of-the-art high resolution SEM, using the column of a standard SEM, is certainly possible. Part II discusses the possibilities, along with the limitations, of changing the acceleration energy and the magnification of the system, in order to render it suitable for high resolution applications. The conclusion is that the MBSEM can work straightforwardly whenever the acceleration energy is in the range 10-30 keV; however, for acceleration energies lower than 5keV, beam deceleration at the sample is required. It is also found that the magnification of the system can be varied, in a limited range, by changing the strength of the accelerator lens. Another, more flexible way of varying the system magnification is by changing the working distance; this method, on the other hand, suffers from a limitation that was analysed in more detail. It was shown that it is possible to change the pitch up to a maximum of $1\mu\text{m}$, by combining the two methods. In part III, the possibilities and the limitations for changing the MBSEM magnification over wider ranges, but for moderate resolutions, are discussed. It is found that, regardless of the type of objective lens used, there is an ultimate limit for the magnification of the objective lens of about $0.3\times$. It follows that the largest obtainable pitch for the MBSEM is $5\mu\text{m}$. The reasons why the standard HR or UHR objective lenses require a large working distance in order to reach higher magnifications are also explained, together with the reasons why this will degrade the probe current,

due to the larger spherical aberration coefficients. An alternative solution is proposed, based on using the combination of HR and UHR lens as objective. It is shown that this combination allows for larger magnifications while keeping the probe current reasonably high.

Chapter 4 describes the actual fabrication of the MBSEM; it includes the construction procedures of a compact multi beam source module, the method of assembly and alignment of the parts, the ways to overcome the issues related to vacuum and electronics of the system.

In Chapter 5, the results of the experiments carried out with the MBSEM are presented, in order to analyse its performance. It consists of two sub-sections. Section 5.1 addresses the first experimental results of the MBSEM, where for the very first time ever the possibility of having 196 (14×14 array) focused beams onto a specimen, using single-beam SEM optics, is demonstrated. The total current of the multi beam source module measured in the Coulomb tube is 150nA, in perfect agreement with its calculated value. The individual probe current of each beam is measured in several steps. First, the current distribution of every beam-let is examined and then, by focusing all the beam-lets as a single spot into a Faraday cup, the total current is measured. From this total current and from the knowledge of the current distribution inside the beam-lets, the probe current of every beam-let is estimated; again, it turned out to be in perfect match with the calculated theoretical values. Due to practical limitations, the first try of simultaneous measurement of the beam size wasn't satisfactory. This was essentially because, for the detection of the transmitted signal, a photocathode had been used, which returned a much larger probe size than expected. Afterwards, one-by-one beam size measurements of the beams were done by using the MBSEM in its single beam SEM mode. Also these results turned out to be in good agreement with calculated data. In section 5.2, the result of simultaneous beam-size measurement using a better signal detector, an 11-zones STEM detector recently developed at FEI Co., is presented. The results show that indeed the

size of the beam-lets is in the order of 1-2nm, in agreement with the calculation results.

Chapter 6 presents the outcome of the use of the MBSEM as a tool for high-throughput electron-beam-induced deposition. 196 dots have been deposited simultaneously onto the sample. This indicates the potential of multi beam Electron Beam Induced Deposition (MB-EBID) in terms of patterning capability and speed enhancement. Furthermore, it is demonstrated that, by shifting the array of beams over distances of several times the beam pitch, rows of closely spaced dots, in which dots originating from different beams within the array are positioned within 5nm from a straight line, can be deposited. This shows that the variation in pitch within the array of beams is smaller than 5nm, and that a good control over the positioning of the array of beams has been achieved.

- **Conclusions**

We have designed and built the world's first Multi Beam Scanning Electron Microscope (MBSEM) that is capable of delivering 196 focused beams, with resolution and current of every sub-beam comparable to that of the state-of-the-art high resolution SEMs. The main motivation behind the development of this system is to increase the throughput of EBID, a direct-write lithography technique for the fabrication of sub-10nm structures. EBID, however, has not yet seen any popularity increase along with the advancement of our MBSEM, as we had hoped for at the beginning of the project. It is not yet considered a versatile lithography technique and there are still problems associated with the involved chemistry, such as the purity of deposits, safety of the precursors, etc. Before these problems are tackled and solved, however, the MBSEM can also be used for high-throughput ordinary electron-beam lithography. Furthermore, it offers great promises for high-resolution and high-throughput electron microscopy, for which of course a special detector has to be developed.

The main conclusions of this work, which are worthwhile to be summarised once again:

1. 196 BEAMS? IT IS POSSIBLE! Yes, it is possible to have 196 beams out of a single Schottky source, each of which having identical probe size and probe current.
2. IN A STANDARD COLUMN? IT IS POSSIBLE! Yes, it is possible to design a multi-beam source module that can fit in the space of the original source module in the column of a standard SEM.
3. IDENTICAL BEAMS? IT IS POSSIBLE! Yes, it is possible to focus all the sub-beams onto the sample with identical beam current and size, comparable to those of a state-of-the-art high resolution single beam SEM, using standard SEM column optics.
4. HIGH VERSATILITY? IT IS POSSIBLE! Yes, it is possible to design a multi beam SEM with flexibility in changing acceleration energy and magnification and the possibility to switch between single beam and multi beam mode.
5. PARALLEL EBID? IT IS POSSIBLE! Yes, even parallel EBID is possible with our current MBSEM.

8 HOOFDSTUK

Samenvatting en Conclusies

Dit hoofdstuk geeft een algemeen overzicht van dit proefschrift en vat de belangrijkste conclusies samen.

- Samenvatting

Het eerste hoofdstuk is bedoeld als introductie voor het hele proefschrift. Via een kort kritisch overzicht van de geschiedenis van de ontwikkeling van de Scanning Elektronen Microscopie, van begintijd tot op heden, laten we zien dat het meeste onderzoek zich altijd concentreerde op het verbeteren van de resolutie van de systemen; en inderdaad is, dankzij deze trend, het oplossend vermogen van de huidige SEM goed genoeg voor elke hoge resolutie toepassing. Aan de andere kant betekent dit, althans volgens de auteur, dat er een andere parameter is die hernieuwde aandacht vraagt en concentratie op verbeterpogingen: de snelheid van een systeem. In het bijzonder is het duidelijk dat de snelheid niet simpelweg verhoogd kan worden door meer elektronen in de bundel te pompen; men moet zich meer complexe oplossingen voorstellen.

Hoofdstuk 2 introduceert een meervoudige-bundel bron (MBS = Multi-Beam Source), bedoeld voor gebruik in de huidige versie van de meervoudige-bundel opstelling. Het eerste deel van het hoofdstuk geeft een kort overzicht van de verschillende meervoudige-bundel bronnen zoals die in de literatuur gevonden worden, als ook het oude MBS concept. De conclusie is dat helaas geen van deze meervoudige-bundel bronnen geschikt zijn voor

het huidige ontwerp en dat een nieuwe bron ontworpen moet worden. Het tweede deel van het hoofdstuk behandelt het elektron-optisch ontwerp van de nieuwe MBS. De laatste twee delen van het hoofdstuk richten zich op de benodigde toleranties van de MBS en op het effect, wat prestaties betreft, van elektron-elektron interacties. Het derde hoofdstuk bestaat uit de volgende drie delen. Deel I gaat in op algemene regels en goede richtlijnen voor het ontwerp van een meervoudige-bundel SEM; het elektron-optisch gedrag van het systeem wordt beschreven, en het elektron-optisch ontwerp van een koppel-lens, een versnellende lens, wordt beschreven; ook wordt een recept gegeven voor berekening/simulatie van de prestaties van het complete systeem op en naast de optische as. De belangrijkste boodschap van dit deel is dat het ontwerp van een systeem, dat in staat is om vele bundels parallel op het preparaat te leveren, en met een typische bundelgrootte en bundelstroom (per bundel) die vergelijkbaar is met een state-of-the-art hoge resolutie SEM, en gebruikmakend van de kolom van een standaard SEM, zeker mogelijk is. Deel II bespreekt de mogelijkheden en ook de beperkingen van het veranderen van de versnelspanning en de vergroting van het systeem met als doel om het geschikt te maken voor hoge-resolutie toepassingen. De conclusie is dat de meervoudige-bundel SEM (MBSEM) zonder verdere complicaties werkt als de versnelenergie in het bereik 10-30 keV ligt; echter, voor een versnelenergie lager dan 5 keV is bundelafremming bij het preparaat vereist. Ook is gezien dat de vergroting van een systeem gevarieerd kan worden, over een beperkt bereik, door het veranderen van de sterkte van de versnellende lens. Een andere, meer flexibele manier van het veranderen van de vergroting van het systeem, is door verandering van de werkafstand; aan de andere kant is het zo dat deze methode lijdt onder beperkingen die in meer detail geanalyseerd zijn. Aangetoond is dat het mogelijk is om vergroting van het systeem te veranderen tot een maximum bundel tot bundel (pitch) van $1\mu\text{m}$ door het combineren van de twee methodes. In deel III worden de mogelijkheden en beperkingen besproken voor het veranderen van de MBSEM vergroting over een groter bereik en voor middelmatige resolutie. De

bevinding is dat er een ultieme limiet voor vergroting van 0.3 is, ongeacht het type objectief-lens dat gebruikt wordt. Hieruit volgt dat de grootst bereikbare bundel tot bundel afstand voor de MBSEM 5 μm is. De redenen waarom de standaard HR of UHR objectief-lenzen een grote werkafstand vereisen om grotere vergrotingen te bereiken wordt ook uitgelegd, alsook de reden waarom dit leidt tot een teruggang in de bundelstroom ten gevolge van de grotere sferische aberratiecoëfficiënten. Een alternatieve oplossing wordt voorgesteld, gebaseerd op de combinatie van HR en UHR lens als objectief. Er wordt aangetoond dat deze combinatie grotere vergrotingen toestaat terwijl de sferische aberratiecoëfficiënten redelijk klein blijven. Hoofdstuk 4 beschrijft de eigenlijke fabricage van de MBSEM; het bevat de bouwvoorschriften voor een compacte MBS module, de assemblage- en uitlijnmethode van de onderdelen, en manieren om problemen rondom vacuüm en elektronica op te lossen. In Hoofdstuk 5 worden de resultaten besproken van de experimenten die met de MBSEM uitgevoerd zijn, met als doel zijn prestaties te analyseren. Het bestaat uit twee sub-secties. Sectie 5.1 richt zich op voorlopige experimentele resultaten van de MBSEM, waar voor het eerst de mogelijkheid wordt gedemonstreerd van het hebben van 196 (14x14 array) gefocusseerde bundels op een preparaat gebruikmakend van enkelvoudige-bundel SEM optiek. De totale stroom van de MBS die in de kolom wordt gemeten is 150 nA, in perfecte overeenstemming met de berekende waarde. De afzonderlijke stroom van elke bundel wordt gemeten in verschillende stappen. Ten eerste wordt de stroomverdeling van elke bundeltje onderzocht en daarna wordt de totale stroom gemeten door alle bundeltjes als een enkele spot in een Faraday cup te focuseren. Uitgaande van deze totale stroom, en de bekendheid van de stroomverdeling binnenin de bundeltjes, wordt de stroom van elke bundeltje afgeschat; Opnieuw blijkt er een perfecte overeenstemming te zijn met de berekende theoretische waarden. Vanwege praktische beperkingen was de eerste poging om gelijktijdig de bundelgrootte te meten niet bevredigend. Dit kwam, in wezen, doordat voor de detectie van een transmissie signaal een fotokathode gebruikt werd, en die gaf een veel grotere

bundelgrootte dan verwacht. Later hebben we de bundel diameters één voor één gemeten, gebruikmakend van de MBSEM in enkelvoudige-bundel SEM modus. Ook deze resultaten blijken in goede overeenstemming met de berekende data te zijn. In sectie 5.2 worden de resultaten gepresenteerd van de simultane bundelgrootte meting met gebruik van een betere signaaldetector, een 11-sectoren STEM detector die recent ontwikkeld is door FEI Bedrijf. De resultaten laten zien dat de grootte van de bundeltjes inderdaad van de orde 1-2 nm is, in overeenstemming met berekende resultaten. Hoofdstuk 6 beschrijft de uitkomst van het gebruik van de MBSEM als een apparaat voor hogesnelheid elektronenbundel geïnduceerde depositie (EBID = Electron Beam Induced Deposition). Er werden gelijktijdig 196 spotjes gedeponerd op het preparaat. Dit geeft aan wat het potentieel is van meervoudige-bundel EBID, in termen van vermogen tot patroneren en snelheidsverbetering. Verder wordt aangetoond dat door het schuiven van een array van bundels over afstanden van enkele keren de bundel tussenafstand, er rijen van dicht aaneengesloten spotjes gedeponerd kunnen worden, waarbij spotjes die afkomstig zijn van verschillende bundels van het array niet meer dan 5 nm afwijken van een rechte lijn. Dit toont aan dat de variatie van de tussenafstand binnen de array van bundels kleiner is dan 5 nm, en dat er goede controle over de positionering van de bundel array bereikt kan worden.

- Conclusie

We hebben de eerste Meervoudige-Bundel Scanning Elektronen Microscoop (MBSEM) ter wereld ontworpen en gebouwd, die in staat is om 196 gefocusseerde bundels te leveren met een resolutie en stroom van elke afzonderlijke bundel die vergelijkbaar is met state-of-the-art hoge resolutie SEM. De belangrijkste motivatie achter de ontwikkeling van dit systeem is het verhogen van de snelheid van EBID, een direct-write lithografische techniek voor de fabricage van structuren kleiner dan 10 nm. EBID heeft echter geen

toename in populariteit gekend in de tijd dat wij vooruitgang boekten met onze MBSEM, iets wat we wel gehoopt hadden aan het begin van het project. EBID wordt nog niet beschouwd als een veelzijdige lithografische techniek en er zijn nog steeds problemen die te maken hebben met de gebruikte chemie, zoals de zuiverheid van de depositie, veiligheid van gassen, etc. Echter, tot de tijd dat al deze problemen aangepakt en opgelost zijn kan de MBSEM ook gebruikt worden voor hoge-snelheid conventionele elektronenbundel lithografie. Verder houdt het ook grote beloften in voor hoge-resolutie en hoge-snelheid elektronenbundel microscopie, waarvoor natuurlijk wel een speciale detector ontwikkeld moet worden.

Er zijn enkele punten van belang in het ontwerp die het waard zijn om nog eens op te sommen:

1. 196 BUNDELS? HET IS MOGELIJK! Ja, het is mogelijk om 196 bundels uit een enkele Schottky bron te verkrijgen, met identieke bundelstroom en bundelgrootte.
2. IN EEN STANDAARD KOLOM? HET IS MOGELIJK! Ja, het is mogelijk een meervoudige-bundel bronmodule te ontwerpen die past in de ruimte van de oorspronkelijke bronmodule in de kolom van een standaard SEM.
3. IDENTIEKE BUNDELS? HET IS MOGELIJK! Ja, het is mogelijk om alle afzonderlijke bundels te focuseren op het preparaat met identieke bundelstroom en bundelgrootte, vergelijkbaar met een state-of-the-art hoge-resolutie enkelvoudige-bundel SEM die gebruik maakt van standaard SEM optiek.
4. GROTE VEELZIJDIGHEID? HET IS MOGELIJK! Ja, het is mogelijk om een meervoudige-bundel SEM te ontwerpen met de flexibiliteit om de versnel-energie en de vergroting te veranderen, en met de mogelijkheid om te schakelen tussen een enkelvoudige bundel en een meervoudige bundel.
5. PARALLELE EBID? HET IS MOGELIJK! Ja, zelfs parallelle EBID is mogelijk met onze huidige MBSEM.

Acknowledgements

With a very good and collaborative team work, everything is possible. Yes I do strongly believe that “Together Everyone Achieves More”. A thesis work is a very good example of a team work, for which the PhD student (at least in the CPO group of Pieter Kruit) is the key person. For any successful team work every single member of the team should contribute positively and efficiently to the common mission, and to support the key person. Now when I look back, I see that indeed we as members of the team worked together very hard and well synchronised to achieve these great results. This team was comprised of three groups: The CPO group, my present work group and my family. I start with CPO group: The number one of this group is of course Prof.dr.ir. Pieter Kruit, my promoter. Without him this work would not have been possible. He introduced me to this project and to the beautiful world of “charged particle optics”. He is my number one “role model” in science and in technology, and also in humanity. Immediately after, I wish to thank Dr. Kees Hagen: tough not officially co-promoter, he was always there to answer to my questions and to sort out things for my experiment when I was in deep frustration, for something or somebody wasn’t there. I would like to thank him for always reading my articles very carefully as well as the draft of this thesis. And I feel like apologising to him for my english writing, by which surely he was drove mad on more than one occasion. Next I would like to thank the technicians of the group for their invaluable work, without which I couldn’t have moved one step forward: Alix, Cor and Ger from “Demo” did a great job in construction of the parts needed for multi-electron beam source module; Carel and Vladimir made micro-fabricated elements; Jacques, Frans and Jan helped me with electronics, control programs and vacuum. I wish I could express all my feeling of esteem and respect to all these people with whom not only I worked on my PhD, but also I shared a lot and enjoyed life. I want to thank the secretaries of the group: Elly, Margaret and Anjella, for helping me pleasantly with all the administration work, and also for always asking “how is everything at home?”. I wish to thank the other members of the group I really enjoyed being with and that were all the time there helping me with any sort of difficulties and questions. I will mention those of them with

whom I shared more. Martijn Van Bruggen, from whom I took over the work; tough he didn't have time, he tried his best in transferring the knowledge that I needed to start the project. Willem van Dorp, who was always helped and supported me with a smile. I would like to thank Anand, for being such a good friend (tough I must say that after he got married he disappeared all of a sudden!). I want to thank four of my best and somehow completely different friends I got from this group and with whom I also shared a lot. Vincenzo Castaldo, "a real man", with his definitions about a real man which I never fitted in! I always enjoy talking to him and discussing Quantum Mechanics and Physics in general. He was about to make me a "smoker" but NOT YET. Benjamin John Cook, or Ben, (or... nevermind!), who drives me mad all the time but for some reason I always forgive him in no time. I still remember the time when the three of us went to buy a car for me and Ben made the owner so angry that he told us: "Ok, I don't care if you are gonna buy my car or not. Just GO AWAY!". David Jun with whom I shared a lot at the very beginning of my PhD and then I thank Christiaan Zonneville for all those practical things that I learnt from him.

The second group are the people in my present work place, FEI electron Optics at Acht. I started my new job at FEI before defending my thesis and by default some people got involved in the finishing and writing this thesis. Guido Knippels, who was my first boss and kind enough to remind me all the time that I had to finish my thesis; and Gerard van Veen who later on took over from him and did exactly the same. Frank de Jong, tough not very explicitly, but quite often tried in reminding me about. I would like to thank them for their reminders. And then I want to thank all my colleagues who are very kind to me all the time. Some of them even got involved in the finishing the thesis: Sander Henstra, whom I know already from the begging of the project, and to whom I used to ask some of my electron optics questions, for his careful reading of chapters 1, 2 and 3; Peter Tiemeijer, from whom I learnt quite a lot of electron optics, for helping me with the Coulomb interaction calculations of the MBSEM and also for translating the propositions into Dutch. He is always there to help me for any problem that I encounter, be it scientific or not, related to work or completely something else. He is my second "role model" in science, technology and humanity. I would like

Acknowledgments

to thank Bart Buijsse for translating the summary and conclusions into Dutch and also Frank van Laarhoven for helping me with my questions about the vacuum and electronics of the Nova-nano SEM, during my work at CPO group and afterwards. I would like to thank Pleun Dona and his wife, Marieke Dona, for designing the cover of the thesis.

The last, but certainly not least, group I wish to thank is of course my family. I was fortunate enough to have my own family beside me all these years. First I would like to thank my wife, my Mahboob, for her continuous love, support, patience and motivation throughout all these years. She always understood me during all those strange working hours at TU-Delft, also when at 3 o'clock in the night I woke up to go and continue with my experiment. I still remember that her family wanted me to quit the study after my M.Sc. and find a "decent job" when I wanted to marry her and she simply told me "pretend that you are listening to them but do what you like, I think you should continue with your study". I also would like to apologise to my children, Sina and Hesam for not spending enough time with them.

Although we never felt out of home in the Netherlands, it is still very important to have families and friends from your own culture and country around you. We are fortunate enough to have a lot of friends around us and I am afraid that if I try to name all of them here, I might miss some. Among many, I would like to especially thank the family of Derakhshandeh, Nikbakht and Rakeei. A very especial thank to Mohammad Mehdi Rakeei for organising the Iranian restaurant in Delft and taking care that everything will go fine, and to his wife Neda Hesam for helping me in producing figure 3.1.10.

Ali Mohammadi-Gheidari

November 2013, Delft.

